Dipl. 2008 - 06
February

Unfluence of Mass Uncertainties of Exotic Nuclei on the rp- and vp- Process Model

Timo Fleckenstein

(Diplomarbeit der Justus-Liebig-Universität Gießen)

Gesellschaft für Schwerionenforschung mbH
Planckstraße 1 · D-64291 Darmstadt · Germany
Postfach 11 05 52 · D-64220 Darmstadt · Germany

Influence of Mass Uncertainties of Exotic Nuclei on the rp- and νp- Process Model

Diplomarbeit

von

Timo Fleckenstein aus Schupbach

Timo.Fleckenstein@physik.uni-giessen.de
Fleckens@nscl.msu.edu

Fachbereich 07 Mathematik und Informatik, Physik, Geographie
Justus-Liebig-Universität Gießen

Gießen, 2007

Contents

Chapter 1

Zusammenfassung

Diese Arbeit untersucht die Rolle der Kernmassen in den Berechnungen der stellaren Nukleosyntheseprozessen. Es wird die Abhängigkeit von stellaren Reaktionsraten von Kernmassen untersucht. Die Frage, die zu beantworten ist, lautet: "Besteht weiterhin die Notwendigkeit in aufwendigen Experimenten Kernmassen auf 10 keV, also mit einem relativen Fehler von 0,000001%, genau zu bestimmen?".

Zur Klärung dieser Frage werden Netzwerk-Simulationen für den *rp*- und νp- Prozess [XRB] [NUP] durchgeführt. Diese Programme berechnen stellare Größen durch die Simulation eines Röntgen-Ausbruchs (*rp*-Prozess) oder einer Supernova-Explosion (νp-Prozess). Stellare Größen sind z. B. die produzierte chemische Verteilung der Elemente oder die emittierte Röntgen-Lichtkurve in einem Röntgen-Ausbruch eines Binärsystems. Für die Beschreibung des $rp-$Prozesses wird die Simulation eines Typ II- Röntgen-Ausbruchs verwendet, der νp-Prozess wird simuliert durch eine Beispielrechnung der Nukleosynthese in protonenreichen Auswürfen von Supernova Explosionen, welche modifiziert wurde um besonders protonreiche Nuklide im Bereich von A=80-105 zu produzieren, damit der νp-Prozess leichter mit dem *rp*-Prozess vergleichbar ist. Dafür wurde ein Computernetzwerk zwischen dem Cluster der Michigan State University (MSU) und der Gesellschaft für Schwerionenforschung (GSI) etabliert. Dadurch ist es möglich die gebündelten Ressourcen mit Hilfe ein einzelnes Master-Programms zu nutzen. Dies geschieht im Sinne des Grid-Computing zur Bewältigung extrem aufwändiger Rechenoperationen.

Ein weiterer großer Teil dieser Arbeit ist die Erweiterung der Massensammlung "Atomic Mass Evaluation 2003" (AME 2003) durch neue Massenmessungen seit 2003. Diese neue Massenwerte ermöglichen eine neue Extrapolation zu unbekannten Massenwerten von protonenreichen Kernen bei A=80-120.

Zur Bestimmung der Abhängigkeit von Massenunsicherheiten auf stellare Syntheseprozesse werden Variationsrechnungen der AME 2003-Massen für den $rp-$ und νp-Prozess durchgeführt. Hierbei werden aus variierten Kernmassen das Verhältnis von Vorwärts- und Rückwärtsreaktionsraten neu berechnet und implementiert. Diese Technik ermöglicht das Aufspüren von Wartepunkten im $rp-$ und νp-Prozess. Die Variationsrechnungen identifizieren ^{93}Pd, ^{94}Ag und ^{91}Rh als Wartepunkte im *rp*-Prozess. Durch die Variationsrechnungen im νp-Prozess kann gezeigt werden, dass die Massenunsicherheiten von ^{100}Cd und ^{93}Pd großen Einfluss auf diesen Syntheseprozess haben. Des weiteren kann gezeigt werden, dass die Wartepunkte im νp-Prozess im Bereich A=80-105 nicht mehr durch die β-Halbwertszeit, sondern durch das Verhältnis von Protoneneinfang- und (n, p)-Reaktionsrate dominiert sind. Durch die neuen

Messungen und Extrapolationen von Massen kann ein direkter Vergleich mit den Massenwerten der AME von 2003 durchführt werden. Hier zeigt sich, dass die Messungen von ^{86}Mo, ^{80}Zr und ^{81}Nb besonders wichtig sind. Schließlich muss man zu dem Schluss kommen, dass Massenmessungen noch immer notwendig sind. Insbesondere zeigt sich, dass die Simulation durch Reaktionsnetzwerke ein wirksames Werkzeug zur Planung von neuen Massenmessungen sein kann. Ebenso muss man erkennen, dass Grid-Computing für Netzwerksimulationen unablässig ist und das zukünftige Bild von Simulationen prägen wird. Diese Arbeit behandelt verschiedene Hilfsmittel der astrophysikalischen Kernphysik, welche helfen den Ursprung der Elemente zu erforschen.

Chapter 2

Introduction

In 1813, the pioneer of spectroscopy, Joseph von Fraunhofer, discovered characteristic absorption lines in the solar spectrum and thus pioneered the investigation of the elemental abundances of the universe. Physicists have explained most of the abundance of the elements beyond the iron group with the slow-neutron-capture process (s-process), proton-capture process (p-process) and rapid-neutron-capture process (r-process)[Hoy56]. Yet, the origin of a few neutron-deficient nuclei in the A=92-126 region is still unexplained [Gor96]. The rp-process is able to produce the lacking nuclei[Wal81], however only a small fraction of the produced nuclei is able to escape from the gravitational field of the neutron star and contribute to the solar abundance of chemical elements [Bur57]. The newly explored νp-process in proton-rich outflows of supernovae explosions provides a mechanism to synthesize the lacking isotopes in the A=92-126 region [Fro06]. The neutrion-driven winds of a supernova provide high temperatures and densities, and thus a possible site for the production of ^{92,94}Mo and ^{96,98}Ru.

For a quantitative understanding of the creation of chemical elements in stellar sites, the nucleosynthesis processes are modeled via reaction network codes. These programs are limited by uncertainties of the physical inputs, e.g. the temperature on the surface of a neutron star, and nuclear physics data. In the course of this diploma thesis, we estimate the influence of mass uncertainties of exotic nuclei in the A=80-105 region on the nucleosynthesis models. On the experimental site, many facilities in various countries, e.g. ISOLTRAP [Kel02], JYFLTRAP [Rah07], LEBIT [Rin06], FRS-ESR [FGM07, Lit07] and SHIPTRAP [Rau06] are dedicated to accurate mass measurements of exotic nuclei. Presently, nucleosynthesis network codes have to rely on theoretical mass models and extrapolations[Aud00][Bor92]. In this work, we focus on mass uncertainties of proton-rich nuclei with A=80-105 and investigate their impact on astrophysical observables, e.g. x-ray burst light-curves, production path and final chemical abundance produced in nucleosynthesis (rp- and νp-) processes. We create a database of mass measurements since the last atomic-mass evaluation AME 2003[Aud03]. In addition, we improve the extrapolations to hitherto experimentally unknown masses close to the proton dripline (see Chapter 4). We have used the network-code for nucleosynthesis processes in a type II x-ray burst [Sch07] and the network-code for nucleosynthesis processes in neutrino-driven proton rich winds of a supernova explosion [Pin07]. A discussion of the results is given in Chapter 6. We also point out classical β-decay waiting points in the endpoint region of the rp-process and the new waiting points of the νp-process.

Chapter 3

Stellar Sites and Nucleosynthesis Processes

3.1 Evolution of Stars - From stable Burning to Core-Collapse Supernovae

Stars, e.g. our sun, are stabilized by an equilibrium of pressures. The outgoing radial pressure, caused by ions and photons is compensated by the gravitational pressure and thus stabilizes the size of the star [Ili07, Jan07]. The gravitational pressure is given by the mass and the radius of the star. The radiation and ion pressure are described by the ideal gas equation. The main source for the energy of the star is the fusion reaction of 4 protons into one ^4He. This is done via two mechanisms the p-p-chain and the CNO(carbon nitrogen oxygen)-cycle [Ili07, Bur57, Hoy56]. Typically, the fusion of hydrogen determines up to 90 % of the star's life [Woo02].

The p-p chain

This energy generating process has been suggested more than 60 years ago by Atkinson 1936 [Atk36]. It has been improved since then by Bethe and Critchfield in 1938 [Bet38],von Weizaecker in 1938 [Wei38] and Bethe in 1939 [Bet39].

The p-p chain synthesizes ^{4}He by fusion reactions combined with weak interactions. The first reaction produces deuterons via fusion combined with β^+-decay (see figure 3.1). This reaction is the bottleneck of the p-p chain, with a typical reaction rate of 1 reaction per 100000 years. The produced deuteron is able to capture an additional proton and forms exited ^{3}He ions, which deexcites via emission of a γ-ray. The detailed production path of the p-p chain is illustrated in figure 3.1. The total energy release of the p-p chain is 26.73 MeV. Up to one fifth of the energy is transmitted via solar neutrinos. A second reaction has been suggested to fuse two protons into a deuteron, the *pep*-reaction. In this reaction mechanism two protons merge under emittance of a positron and a neutrino ($p(pe^+, \nu)d$). Bahcall and May have shown in 1969 [Bah69] that this mechanism is able to compete with the p-p chain only at stellar densities in excess of $10^4 \frac{\mathrm{g}}{\mathrm{cm}^3}$. Therefore, the *pep*-reaction is important for the energy production in early stages of explosive hydrogen burning [Ili07].

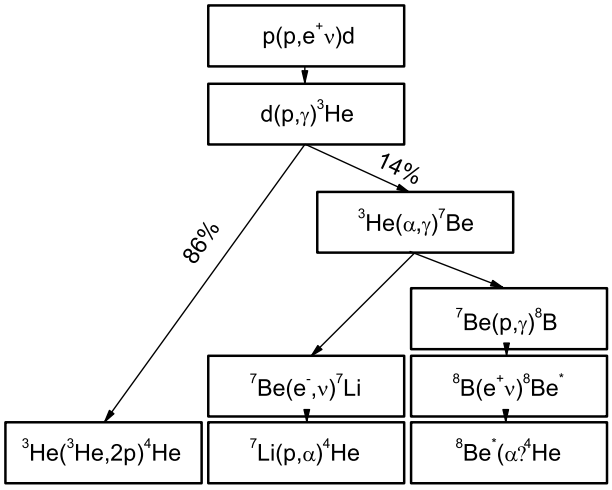

Figure 3.1: The p-p-chain describes the fusion of 4 protons into ^{4}He.

CNO-cycle

If only a little amount of ^{12}C is available, e.g. in 2nd and 3rd generation stars, or created via helium burning (the description of the helium burning is given in the next subsection) the carbon-nitrogen-oxygen-cycle (CNO-cycle) starts [Ili07]. This cycle burns protons faster than the p-p chain. This process governs the energy production in heavier stars, due to its dependence on the carbon abundance and on temperature. The net result of this cycle is to fuse 4 protons into one ^{4}He and 2 positrons and 2 neutrinos. The positrons annihilate with electrons and release energy in form of γ rays. The carbon, oxygen and nitrogen of the CNO-cycle serves only as catalysts. 4 different CNO-cycles exist.

CNO1	CNO2	CNO3	CNO4
$^{12}C(p,\gamma)^{13}N$	$^{14}N(p,\gamma)^{15}O$	$^{15}N(p,\gamma)^{16}O$	$^{16}O(p,\gamma)^{17}F$
$^{13}N(\beta^+\nu)^{13}C$	$^{15}O(\beta^+\nu)^{15}N$	$^{16}O(p,\gamma)^{17}F$	$^{17}F(\beta^+\nu)^{17}O$
$^{13}C(p,\gamma)^{14}N$	$^{15}N(p,\gamma)^{16}O$	$^{17}F(\beta^+\nu)^{17}O$	$^{17}O(p,\gamma)^{18}F$
$^{14}N(p,\gamma)^{15}O$	$^{16}O(p,\gamma)^{17}F$	$^{17}O(p,\gamma)^{18}F$	$^{18}F(\beta^+\nu)^{18}O$
$^{15}O(\beta^+\nu)^{15}N$	$^{17}F(\beta^+\nu)^{17}O$	$^{18}F(\beta^+\nu)^{18}O$	$^{18}O(p,\gamma)^{19}F$
$^{15}N(p,\alpha)^{12}C$	$^{17}O(p,\alpha)^{14}N$	$^{18}O(p,\alpha)^{15}N$	$^{19}F(p,\alpha)^{16}O$
$T_{1/2}:^{13}N(9.965min)$	$T_{1/2}:^{15}O(122.24s)$	$T_{1/2}:^{17}F(64.49s)$	$T_{1/2}:^{18}F(109.77min)$

Table 1: The table shows all four possible CNO-cycles. $T_{1/2}$ gives the longest half-life in the cycle, and therefore the delimiting factor for the timescale of this chain [Ili07].

Higher burning stages

The consumption of hydrogen reduces the radiation pressure of the star, due to the increasing abundance of ^{4}He. The star gains energy from the contraction. The star has to exceed a threshold temperature, in order to ignite the different burning mechanism. The temperature, which can be achieved by a contraction is given by the initial mass of the star. The second

burning, after the hydrogen burning is the helium burning, afterwards carbon, neon, oxygen and silicon burning. Stars, which ignite Carbon burning, create a massive iron core. The helium burning occurs for star with more than 0.5 solar masses. This process synthesizes carbon from helium. Two ^{4}He-nuclei fuse and produce the meta stable nucleus ^{8}Be if the transmitted energy of the helium corresponds to the resonance energy of the meta stable state of ^{8}Be. The meta stable beryllium is able to capture an additional helium and form the stable nucleus ^{12}C. The energy release for this reaction is 7.275 MeV. More massive stars (at least 8 solar masses) are able to ignite the carbon burning. Because of the initial mass of the star, it can exceed a temperature of $6 \cdot 10^8$K($T9 = 0.6$) and a density of $2 \cdot 10^5 \frac{\mathrm{g}}{\mathrm{cm}^3}$. In this phase, the star fuses ^{12}C nuclei and creates ^{20}Ne, ^{23}Na or ^{23}Mg. Even heavier stars ignite neon, oxygen and silicon burning, thus these massive stars are able to fuse nuclei up to iron. The fusion of nuclei, heavier than iron consumes energy, due to fact that iron has the highest binding energy per nucleon. During the different burning periodes after the p-p chain, the energy emission is increased, and thus the star expands. This core consists mainly of nickel and iron. The size of the iron-nickel core depends on the birth mass of the star, typical if the initial mass of the star has been bigger than 8 solar masses, the iron core can exceed the Chandrasekhar limit. After the star has finished the energy production via burning processes, the energy emittance becomes smaller than the containing gravitational pressure, therefore the outer layers of the star are accelerated in the gravitational field of the star. The particles in the outer and inner layers can exceed more than 20 percent of the speed of light. The accelerated matter crashes on the iron core. Because of the increasing pressure on the core of the star the electrons in the degenerated gas gain energy and reach relativistic velocities. Due to the fact that the pressure goes with 4/3 for relativistic electrons(equation (3.18)) the star starts to collapse. The collapse stops, because of the creation of a proto neutron star. The neutrons in the neutron star, cause a stabilization, because of the non-relativistic energies of the neutrons and therefore the 5/3 dependence of the pressure of the degenerated gas(equation (3.18)). The gravitational energy is transformed into a burst of νs and radiation. The radiated energy can be approximated with

$$\frac{3}{5}\frac{GM_{NS}^2}{R_{NS}} \approx 3 \cdot 10^{53}\mathrm{ergs}\frac{(M_{NS}/1.4M_\odot)^3}{R_{NS}/10\mathrm{km}} \tag{3.1}$$

G is the gravitational constant. M_{NS} and R_{NS} is the mass and the radius of the neutron star.

A $8M_\odot$-star would emit up to $\sim 10^{59}$ neutrinos [Bal05]. Furthermore the neutron star causes a bounce back of the accelerated matter, which forms a shock wave. This mechanism is called prompt explosion mechanism. However, this mechanism can not cause the distribution of the supernova remnant (figure 3.2), because of the great energy loses of the shock wave inside the dense layers of the neutron star. A second mechanism, the neutrino interaction or heating transfers energy on the outer layers of the supernova and therefore supports the distribution of the supernova remnant.

In the course of this work, the proton-rich wind are investigated of stars with more than 15 solar masses. The ejecta of such stars can be divided into two kinds, the hot bubble ejecta and neutrino-driven winds. The hot bubble ejecta comes from a region outside the neutron star, therefore it does not have to overpower the gravitational force on the neutron star surface. The characterizing conditions of the hot bubble outflows are a relatively small entropy ($s/k_B \sim 20 - 30$) and an electron fraction of $Y_e \lesssim 0.52$. The wind ejecta originates from the neutron star surface with higher entropies ($s/k_B \sim 50 - 80$), a high $Y_e \approx 0.57$ and a short initial expansion timescale. [Pru06, Fro05]

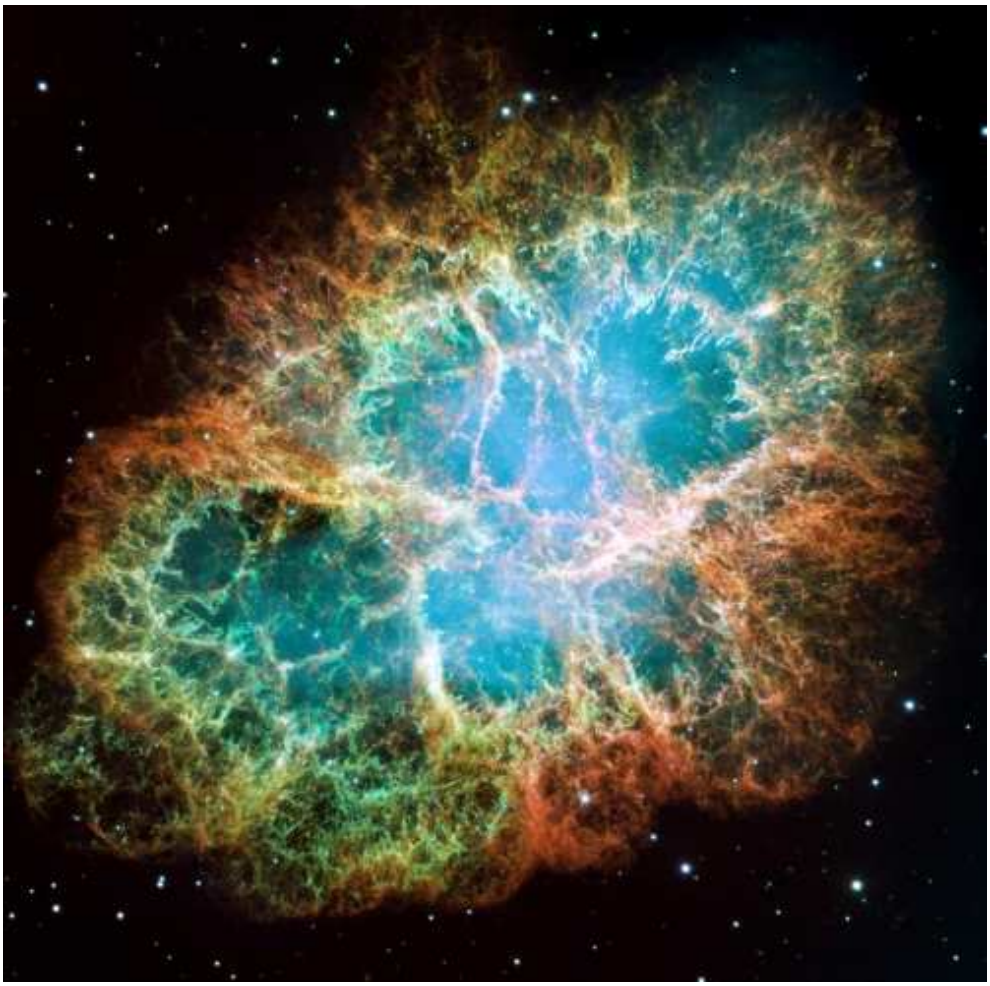

Figure 3.2: The supernova remnant 'Crab Nebula'. The remnant consits mainly of hydrogen and less helium [Nas07b]

.

In this work, the neutrino-driven wind is discussed and modeled in a selfconsistent network code [Fro06]. The young neutron star, originates from a core collapse supernova, emits photons and neutrinos. The whole gravitational binding energy (10^{53}erg) is radiated approximately equally in ν_e,$\bar{\nu}_e$,ν_μ,$\bar{\nu}_\mu$,ν_τ,$\bar{\nu}_\tau$ [Arc07, Rap06]. This process is called Kelvin-Helmholtz phase and lasts approximately 10s. The available neutrinos heat the layer of the supernova and interact weakly with the material. Therefore the matter expands away from the neutron star surface. This mass outflow is called: 'neutrino-driven winds'. The nucleosynthesis in the neutrino-driven winds is mainly sensitive to four physical parameters that characterize the wind: the mass loss rate $\dot{M}$ of the neutron star, the entropy per baryon S, the electron fraction Y_e and the dynamic time scale τ of the process [Qia96]. These parameters are time-independent, and thus one can use the steady-state assumption. The following equations have been discussed in reference [Qia96].

$$\dot{M} = 4\pi r^2 \rho v \tag{3.2}$$

$$v\frac{dv}{dr} = -\frac{1}{\rho}\frac{dP}{dr} - \frac{GM}{r^2} \tag{3.3}$$

$$\dot{q} = v(\frac{d\epsilon}{dr} - \frac{P}{\rho^2}\frac{d\rho}{dr}) \tag{3.4}$$

ρ is the rest mass density, v is the velocity of the mass outflow, T is the temperature, P is the total pressure and ϵ is the specific internal energy, $\dot{q}$ is the heating rate, due to neutrino interactions.

These equations are difficult to solve, therefore the network code for the nucleosynthesis in the neutrino-driven proton rich winds are modeled, via an approximation for the density evolution. The evolution of stellar density in the adiabatic expansion mode is given by [Mey02]:

$$\rho(t) = \rho_1 \cdot exp[-\frac{t}{\tau}] + \rho_2 \cdot (\frac{\delta}{\delta + t})^2 \tag{3.5}$$

The exponential function describes the inital density and the evolution short after the bounce back of the core-collapse supernova. The second summand governs the late time evolution, it is determined by the collision of the supersonic neutrino-heated matter with the shock front, originated from the core-collapse. The collision causes an increase of the densities, thus an increase of temperature for a short time. In this time, temperatures above 1 GK are provided, which are necessary for the proton capture reactions of the *rp*-process. The temperature changes are determined by a constant entropy. A recent discussion of the physical conditions of the neutrino-driven winds is given in [Qia96].

3.2 The νp-Process

The νp-process is a very dynamical nucleosynthesis process [Fro06, Wan06]. It takes place in core-collapse supernovae and is also possible in collapsar jets or disk winds formed at a black hole [Pin06, Pru05]. This process is a candidate for the production of neutron-deficient nuclei (p-nuclei) in the mass region from A=92 to 126. Especially ^{92,94}Mo and ^{96,98}Ru are dramatically underproduced. Without the understanding of the νp-process it has not been possible to produce heavier nuclei than ^{64}Ge on the neutron-deficient side, because of its long beta-decay half-life in comparison to the short time of the supernova explosion (10-20s) [Pru06]. Because of the production of additional neutrons due to antineutrino-capture-reactions, it is now possible to bridge long-lived waiting points, as ^{64}Ge for example. A waiting point is a nucleus with a long half-life, compared to the proton- or neutron-capture-rate. For a deeper understanding of the νp-process further observations are necessary. Physicists observe metallpoor and hyperpoor stars. These stars are extremely old but they have not yet completed their carbon burning phase thanks to their small size. Therefore, these stars are perfect witnesses for first generation supernovae. Their abundance pattern consists mainly of hydrogen and helium and to a smaller extent of carbon and oxygen. Stars of later generations have been formed by other supernovae remnants; thus their chemical abundance differs. To discover such faint hypermetall poor stars is a real big challenge [Fre06].

Because of these additional ν-captures this process is able to bypass well-known waiting points in the *rp*-process by (n,p)-reactions [Kis07]. Maybe the most important input in the νp-process is the electron abundance Y_e. This quantity determines the fraction of protonrich and -deficient nuclei.

$$X_n = 1 - Y_e(i) \tag{3.6}$$

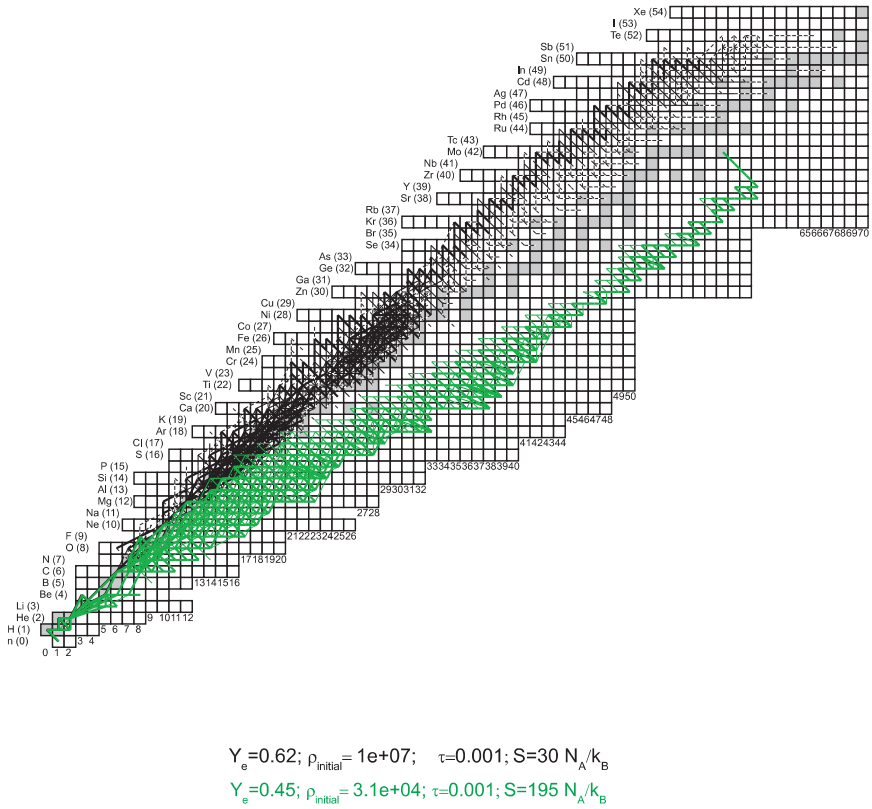

Figure 3.3: Two different settings for the νp-network calculations lead to the production of n-rich and n-deficient nuclei [NUP].

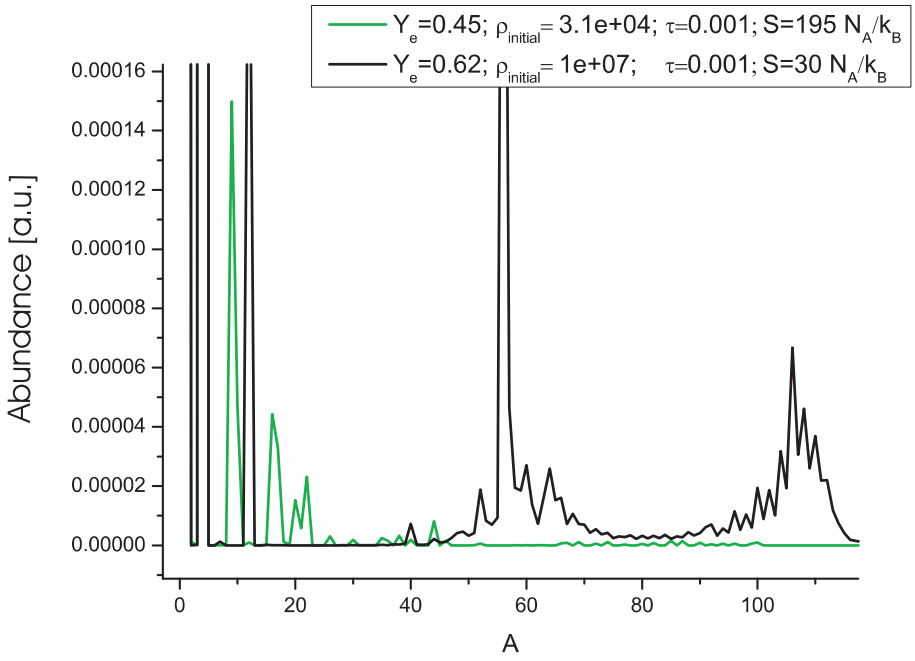

Figure 3.4: The produced abundances for different initial conditions in the νp-process. Illustrated in figure 3.3 [NUP].

$$X_p = Y_e(i) \tag{3.7}$$

$Y_e(i)$ is the initial electron abundance. $X_{n,p}$ is the mass fraction of neutrons and protons. The most dominant reactions to change the electron fraction are the weak interactions

$$\nu_e + n \leftrightharpoons p + e^- \tag{3.8}$$

$$\bar{\nu}_e + p \leftrightharpoons n + e^+ \tag{3.9}$$

Therefore, the electron fraction evolves during the nucleosynthesis in the neutrino driven wind. For different $Y_e(i)$ in the model the path is totally different. The different production paths and final abundances are illustrated in figure 3.3 and 3.4. (For more information, please view the parametric studies made by [Wan06].) With the variation of the electron fraction, it is possible to cover both the production of neutron- rich and deficient nuclei.

3.3 X-Ray Binaries - Site of the *rp*-Process

X-ray binaries have been discovered early in the 20th century because of their high luminosity. Physicists (R. Giacconi et al. Nobel prize 2002) used 'sounding rocket flights' to detect these extraterrestrial signals in the radio frequency band, but it has not been possible to locate their origins, because of the short measurement time. With the launch of the 'Uhuru' satellite, it has become possible to trace back these signals to x-ray binary systems. To the present day, x-ray binaries form a very interesting physical phenomenon with many unsolved problems and interesting open physical questions. BeppoSAX, Chandra X-ray and XMM-Newton explore such galactic events. However, it is still difficult to get clear and detailed data of such events. For many years physicists have been doing spectral analysis of stars in order to detect the galactical chemical abundances [Gal03]. To measure the chemical abundance of an accreting neutron star has not been possible, so far. On the other hand, physicists measure nuclear properties, e.g. reaction rates, deformations, lifetimes and masses, which are directly connected to astrophysics [Maz07]. X-ray binaries are a possible site for the *rp*-process [Sch99, Sch06b, Woo04].

An x-ray binary system consists of a supernova remnant, a so called neutron-star and a companion star, e.g. a red giant. A neutron star is a compact stellar object, typical with ≥ 1.4 solar masses, of which the radius amounts to only 10 km. The neutron star is able to accrete matter from its companion star. The neutron star accretes matter from the envelope of the companion star and the matter forms an accretion disc because of its angular momentum. This is illustrated in figure 3.5. However two different classes of x-ray burst binary systems, low-mass binary and high-mass binary, have to be taken into consideration. In a low-mass binary system, a neutron star orbits a giant star of about 1.4 solar masses, which is the minimum mass of neutron star, derived by Chandrasekhar. This system only emits x-ray radiation. In a high-mass binary system, a neutron star surrounds a very young massive star, with more than 10 solar masses. Because of the high mass of the companion star, the star also emits a lot of particles, the so-called solar wind, which are accumulated by the neutron star. In general, matter is transferred because of a mechanism called 'Roche lobe overflow'. For further information, please look at [Sav79]. The typical lifetime of high-mass systems is much shorter than an of low-mass systems, but high-mass systems have higher luminosities, which cover a larger band of frequencies. The brightest x-ray binary, right now, is 'Sco X-1'.

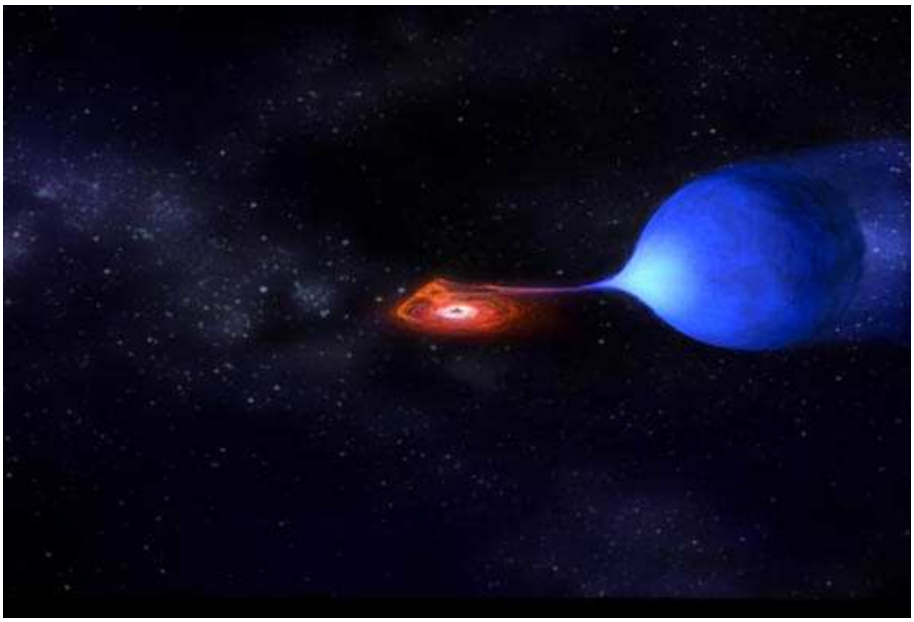

Figure 3.5: Accretion disk of X-ray binary. A neutron star orbits a companion star, e.g. a red giant and accretes matter in typical solar abundance [Nas07].

The material impinges on the crust of the neutron star, and, due to the strong gravitational field, the material is compressed. The material reaches densities up to $10^6 \frac{g}{cm^3}$ [Ili07]. Therefore, the temperature of the matter, accreted on the neutron star surface, increases extremely, this leads to continuous radiation at x-ray energies, which is detectable on earth. An x-ray binary does not only emits continious x-ray radiation, but also x-ray bursts. A burst is a dramatic change in the luminosity of such a system. The typical spectra can be approximated with black body radiation, with a shift to lower frequencies for later times after the burst. This kind of x-ray burst has been defined as Type I burst, by Hoffman, Marshall and Lewin in 1978 [Hof78]. A second type of x-ray bursts has been defined for 'fast burster'. The spectra of these x-ray bursts are similar to the black body radiation without a frequency shift after the burst, like in type I. The luminosity of the type II x-ray burst is nearly proportional to the time after the burst and before the next burst. It is assumed that type II x-ray bursts happen in low-mass binary systems. A low-mass binary system is typically older than a high-mass system, which results in a weaker magnetic field of the neutron star. Therefore, the binary system does not pulse with its radiofrequency [Sch98a].

The event of the accretion of a neutron star is characterized by the initial conditions for pressure P, temperature T and the composition of the accreted layer X_i [Sch98]. The network code, which is used in the course of this diploma thesis, models the nucleosynthesis in a type II x-ray burst with an one-dimensional, single burst and self-consisting code. Furthermore, it is approximated that the accreted layer is in hydrostatic equilibrium. This is reasonable, because the typical timescale for achieving the hydrodynamical equilibrium is small ($\tau_{hydro} \approx 10^{-5} s$) in comparison to the dynamic timescale of the x-ray burst. Additionally, one neglects changes of weight in the accreted layer, due to matter losses or additional accretion. Therefore, one assumes a constant pressure in the burning zone. Therefore, the pressure is related to temperature and density by the equation of state. The following equations are given in [Sch98a, Pac83].

$$P = f(T, \rho, n_{El}, n_{Ion}) \tag{3.10}$$

The particle densities n_{El} and n_{Ion} are defined as:

$$n_{Ion} = \rho \cdot N_A \cdot \sum_i \frac{X_i}{A_i} \tag{3.11}$$

$$n_{El} = \rho \cdot N_A \cdot \sum_i \frac{Z_i \cdot X_i}{A_i} \tag{3.12}$$

The pressure P consists of three parts, the pressure resulting from the electron gas, the ion gas and the radiation.

$$P = P_{El}(T, n_{El}) + P_{Ion}(T, n_{Ion}) + P_{Radiation}(T) \tag{3.13}$$

The pressure of the ion gas can be described with the ideal gas equation:

$$P_{Ion} = n_{Ion} k_B T \tag{3.14}$$

k_B is the Boltzmann constant

The radiation pressure is given by:

$$P_{Radiation} = a \cdot \frac{T^4}{3} \tag{3.15}$$

a is the radiation constant

The description of the electron gas is more complicated, due to the degenerated gas effect for low temperatures . The equation of state (EOS) for the pressure is defined as:

$$P_{el} = \sqrt{P_{end}^2 + P_{ed}^2} \tag{3.16}$$

with the ideal gas part P_{end}

$$P_{end} = n_{El} k_B T \tag{3.17}$$

and the degenerated part P_{ed}

$$P_{ed} = [(9.91 \cdot 10^2 12(\frac{n_{El}}{N_A})^{5/3})^{-2} + (1.23 \cdot 10^{15}(\frac{n_{El}}{N_A})^{4/3})^{-2}]^{-1/2} \tag{3.18}$$

Every component contributes to the pressure in the accreted layer. The pressure of the electron gas governs the low temperature region (below 0.4 GK). The radiation pressure dominates for higher temperatures (above T9=2 ($T9$ is defined as temperature in GK)). Because of the T^4 dependence of the radiation pressure, it causes that the explosion extinguishes. The whole process is controlled by the temperature T. The temperature change ΔT is caused by the energy production rate ϵ_{nuc} and by the emitted energy rate ϵ_{cool}.

$$\Delta T = \frac{1}{c_P} \cdot (\epsilon_{nuc} - \epsilon_{cool}) \tag{3.19}$$

c_P is the specific heat constant for constant pressure

ϵ_{nuc} describes the energy production rate, due to nuclear reactions in the accreted layer. ϵ_{cool} is determined by the energy loss of the burning zone, because of energy losses, due to the emission of photons and neutrinos that are created in weak interactions.

$$\epsilon_{cool} = \frac{a \cdot c \cdot T^4}{3\kappa y^2} + \epsilon_\nu \tag{3.20}$$

y is the column density ($y = P/g$). That describes the position of a particle in the layer. ϵ_ν is the energy loss, due to neutrino emission. g has to be calculated, including general relativistic effects. κ is the opacity for photons of a layer.

Whenever the temperature exceeds the critical point ($T = 1 \cdot 10^7 K$) [Sch06b], nuclear burning starts via the triple α process, which fuses three ^{4}He into one ^{12}C. A detailed description is given in 3.1. The hot CNO-cycle fuses 4 protons into one ^{4}He via several reactions including carbon, nitrogen and oxygen as catalysts [Rem97]. These fusion reactions heat the different layers of the neutron star atmosphere. Finally, these layers explosively expand and the explosive hydrogen burning takes place. However, there are two different accretion modes of binary systems. The slow accretion mode ($dm/dt < 1 \cdot 10^{-9} \frac{M_\odot}{a}$) creates pure layers or hydrogen and helium [Sch99b]. The whole amount of hydrogen is transformed into helium. Additionally, all nuclear burning processes take place in thin shells ('Thin shell burning') [Fis07], which causes a thermal instability, due to the fact that the layers cannot expand during the heating-up phase. These thin layers cannot expand. As the electron gas is degenerated the pressure is temperature independent. On the other hand the nuclear reactions are strongly dependent on the temperature. During the fast accretion mode of a binary system ($dm/dt > (2-5) \cdot 10^3 (\frac{Z_{CNO}}{0.01})^{13/18}$). Z_{CNO} is the mass fraction of CNO in the accumulated matter, the helium ignites while hydrogen is still available in the layer, thus the helium burning becomes unstable. The helium ignition triggers mixed H/He burning. Because of the strong temperature dependence of the helium-burning rate, one observes strong 'thin-shell-instabilities'($T9 = 0.5K$), which leads to an x-ray burst that is studied in this diploma thesis.

3.4 The *rp*-Process

The *rp*-process occurrs during x-ray bursts [Amt06, Sch05, Sch06a]. This process is a chain of proton capture reactions (p, γ) and beta-decays. Photo disintegration reactions (γ, p) compete with proton capture reactions and thus equilibrium states on or close the proton dripline are established. The reaction rates depend on the temperature and density in the stellar environment. Typically, capture-reactions are much slower than beta-decays for low temperatures (below 1 GK). Because of the high temperatures (1.5 GK) and high densities, which are achievable in the x-ray burst scenario the nucleosynthesis is a fast reaction network of proton-capture reactions. The cross sections for capture-reactions increase for higher temperatures and densities, thus the capture reactions become faster than the beta-decay reactions. As a logical consequence, nuclei are produced, which are close to the proton dripline. On the other

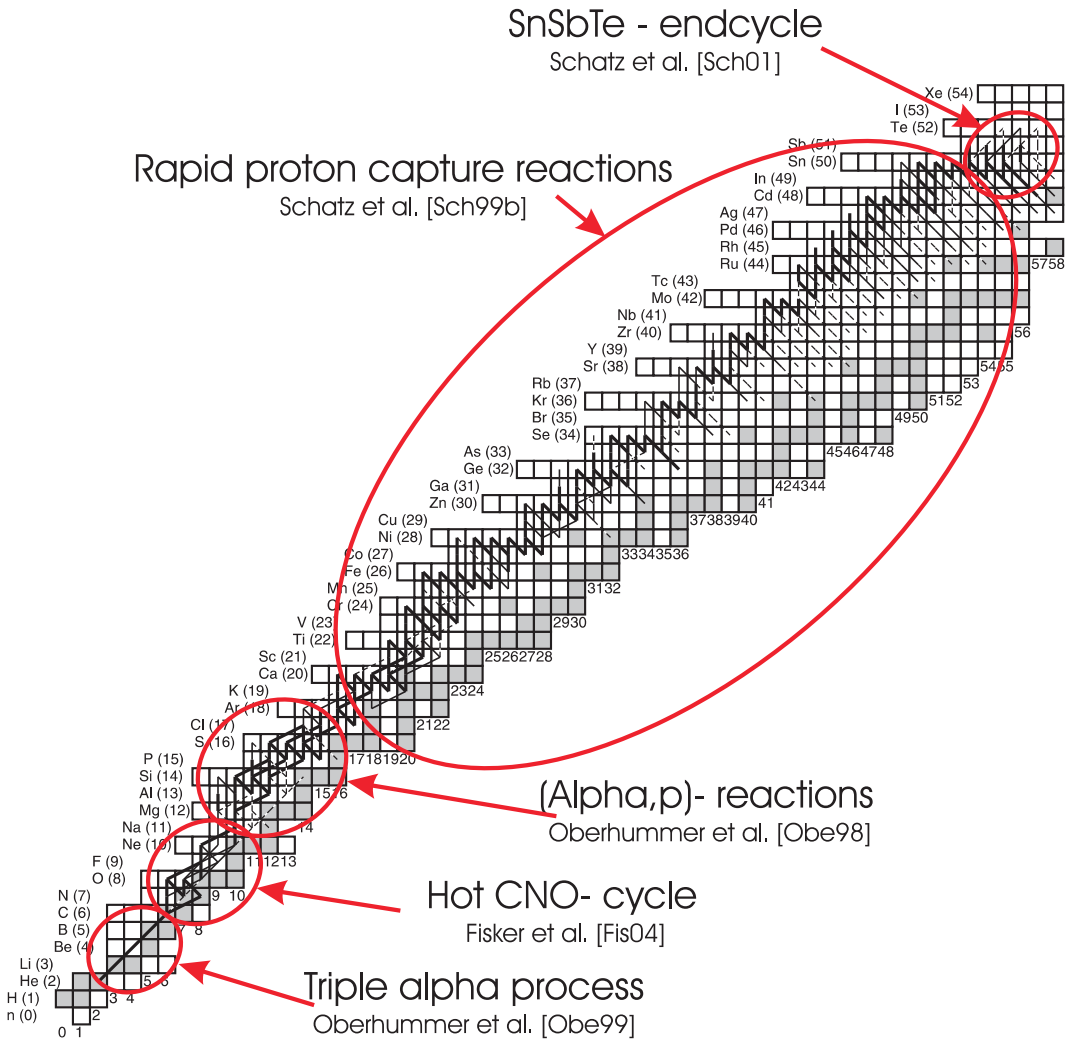

Figure 3.6: The production path of the *rp*-process in x-ray binary systems [Sch01, Jon05, XRB]

hand, the low separation energies for protons and neutrons in the vicinity of the driplines enforce backward reactions (A forward reaction is defined as capture reaction, whereas the backward reaction is caused by photo-dissociation). Consequently, equilibrium states are established in between and the reaction flow stops. At these extreme conditions, the production path is governed by partial quasi nuclear statistical equilibrium (QSE). The proton-capture equilibrium can be described with reference to their abundances. This can be approximated with the Saha equation [Sch06a]:

$$\frac{Y_{n+1}}{Y_n} = \rho_n \frac{G_{n+1}}{2G_n} \left(\frac{A_{n+1}}{A_n} \frac{2\pi\hbar^2}{m_u kT}\right)^{3/2} \cdot exp\left(\frac{S_{n+1}}{kT}\right) \tag{3.21}$$

Y_n and Y_{n+1} are abundances of neighbor nuclei n and n+1. T is the temperature of the environment, ρ_n is the neutron density and G is the partition function. A is the mass number of the nuclei with the atomic mass unit m_u . k is the Boltzmann constant and S is the separation energy between the nuclei n and n+1.

$$S_p = M(A,Z) - M(A-1,Z-1) - m_p \tag{3.22}$$

Therefore the mass differences contributes exponentially to the abundance ratio. The separation energies are extremely important for nuclei close to beta-decay waiting points. Furthermore, the calculation of forward reaction rates, as proton captures, is important for nucleosynthesis networks. Typically, proton capture rates, which are far away from stability, are given by a few narrow resonances [Her95, Sch05]. The reaction rate consists of a resonant and a non-resonant part. The resonant part of the rate can be described with [Sch06a]:

$$N_A < \sigma v >= 1.540 \times 10^{11} (\mu T9)^{-3/2} \Sigma_j \omega\gamma_i exp\left(\frac{-E_j}{kT}\right) \frac{cm^3}{s \cdot mole} \tag{3.23}$$

E_j is the resonance energy in the center of mass system. The temperature is given by T9 in GK. μ stands for the reduced mass of the entrance channel.

The resonance strengths $\omega\gamma_j$ for proton captures are given by [Sch06a]:

$$\omega\gamma_j = \frac{2J_j + 1}{2(2J_T + 1)} \frac{\Gamma_{pj}\Gamma_{\gamma j}}{\Gamma_{totalj}} \tag{3.24}$$

J_T is the spin of the target nucleus. $J_j, \Gamma_{pj}, \Gamma_{\gamma j}$ and Γ_{totalj} are spin, proton decay width, γ-decay width and total width of compound nucleus state j.

The second contribution (non-resonant) to the reaction rate can be expressed by the astrophysical S-factor [Ili07, Her95]. The direct proton capture rate is given by [Sch06a]:

$$N_A < \sigma v >_{direct} = 7.83 \times 10^9 \left(\frac{Z}{\mu T9^2}\right)^{1/3} S_i(E_0) exp\left(-4.29 \cdot \left(\frac{Z^2\mu}{T9}\right)^{1/3}\right) \frac{cm^3}{s \cdot mole} \tag{3.25}$$

The astrophysical S-factor $S(E_0)$ is given in MeV barn. E_0 is the Gamov window energy.

Chapter 4

Mass measurement of Exotic Nuclei

4.1 Production and Separation of rare Isotopes

Basic properties of a nuclide like lifetime, mass and matter distribution are essential for the understanding of astrophysical nucleosynthesis processes. Accurate mass measurements [Lun03, Gei95] are a crucial test for nuclear theory and enable reliable extrapolations. The direct mass measurements use ions in different charge states. The conversion of the measured result to atomic masses m_{atom} can be accurately be done because of the well-known mass of the electron and their atomic binding energies [Ili07]:

$$m_{atom}(A,Z) = m_{nuc}(A,Z) + Zm_e - B_e(Z) \tag{4.1}$$

m_{nuc} is the mass of all nucleons, m_e is the mass of an electron and B_e is the binding energy of the **??** electrons.

In order to, describe nuclear decays, one frequently uses the atomic mass excess M:

$$M = (m_{atom} - Am_u)c^2 \tag{4.2}$$

m_u is the unified atomic mass unit, which is defined as one-twelfth of the mass of a neutral ^{12}C.

The separation energies are defined as[Ili07]:

$$S_{2p} = M(A-2,Z-2) - M(A,Z) + 2 \cdot m_p \tag{4.3}$$

$$S_{2n} = M(A-2,Z) - M(A,Z) + 2 \cdot m_n \tag{4.4}$$

$M(A,Z)$ is the mass excess of a nucleus with massnumber A and Z protons

In order to improve nuclear theory and the understanding of stellar nucleosynthesis processes new experiments are needed to measure the properties of exotic nuclides close the the proton- and neutron- driplines. Thus the challenge for future experiments is to measure exotic nuclei with short half-lives and very small production cross sections. Mainly two production and separation mechanisms, the In-Flight and the ISOL-techniques, are used to produce and investigate exotic nuclei.

4.1.1 In-Flight Separation

In-Flight separators take advantage of the specific reaction kinematics to separate selected nuclear reaction products from contaminants and the primary beam [FGM07]. A high energy heavy ion projectile beam creates exotic nuclei in a thin target. The reaction products emerging from the target penetrate the separator with high velocities, thus it it possible to access very short lived nuclei. The flight time through the ion-optical system is the lower limitation for experiments with exotic nuclei at in-flight separators. The time-of-flight (ToF) is of the order of microseconds in devices used near the Coulomb barrier (SHIP [Mue79]) and decreases to a few hundred nanoseconds within separators for relativistic nuclei (FRS [Gei92]). At low energies, near the Coulomb barrier (a few MeV/u) the fusion reactions are well suited to provide exotic nuclei near the proton dripline and in the super-heavy atom region ($Z > 100$). At energies, much higher than the Coulomb barrier, the cross section for fusion reactions drastically decreases. Projectile fragmentation and projectile fission are superior reactions to provide exotic nuclei at higher beam energies up to the relativistic region. In the fragmentation reactions the heavy projectile interact with the target nuclei, via nucleon-nucleon collisions. This reaction type can be described by two steps, abrasion and ablation processes [FGM07]. Projectile fission reactions have been successfully applied with uranium projectiles at roughly 1GeV/u [Ber94] to produce medium mass neutron-rich nuclei. The fission process can be initiated by electro-magnetic excitation of or precedent nucleon removals from the incident uranium projectiles [FGM07]. The projectile fission fragments occupy a much larger phase space than the fragmentation products.

The in-flight separators SHIP and FRS at GSI are placed at the UNILAC and the SIS18, respectively. The linear accelerator UNILAC provides projectiles at the Coulomb barrier for fusion products, the synchrotron SIS18 is ideally suited for projectile fragmentation and fission up to a maximum magnetic rigidity of 18 Tm according to maximum beam energy of $E = 1922$ MeV/u for $m/q = 2$. The SHIP consists of two spatially separated Wien filters. These filters separate fusion products from projectiles according to their large velocity difference: In complete fusion reactions the kinematics is governed by the momentum conservation.

$$v_1 \cdot m_1 + 0 = (m_1 + m_2) \cdot v_2 \tag{4.5}$$

$$v_2 = \frac{m_1}{m_1+m_2} \cdot v_1 \tag{4.6}$$

$v_{1,2}$ and $m_{1,2}$ are the velocities and the masses of the projectile and the compound nucleus, respectively.

The advantage of a velocity filter is that the separation does not depend on the mass-over-charge ratio. The absolut value of the electrical and the Lorentz force are equal:

$$q \cdot E = q \cdot v \cdot B \tag{4.7}$$

$$v = \frac{E}{B} \tag{4.8}$$

v is the velocity of the particle E is the electrical field, B is the magnetic field.

This is important, because the UNILAC generates multiple charge states for each ion emerging from the target. After the compound nuclei are separated by SHIP, they can be stopped in a gas cell for further investigations (SHIPTRAP [Blo05]).

The in-flight separation at the FRS is performed by a twofold magnetic rigidity analysis in combination with atomic energy loss in a shaped degrader ($B\rho - \Delta E - B\rho$ - method [Gei92]).

In this way monoisotopic fragment beams can be provided for all elements up to uranium. High-resolution experiments can be performed with the unique combination of the FRS with the experimental storage and cooler ring ESR [Fra87].

4.1.2 ISOL

In the ISOL technique [Rav94] a very thick high-Z target is bombarded by a high-intensity light ion beam, e.g. protons. With a thick one obtains higher production rates of exotic nuclei [Lun03, Gue07, Lun01]. The primary production reactions can be divided into two groups, the proton-induced target fragmentation (spallation) and the proton-induced fission reactions. In the proton-induced fragmentation the nucleon-nucleon interaction creates exotic nuclei, as described above for the projectile fragmentation. Neutron-rich medium mass isotopes are preferentially produced via proton-induced fission reaction. Uranium compounds are used as target materials for the fission reactions. The produced reaction products are completely slowed down inside the thick target material. The produced exotic nuclei are released from the target by heating. The total timescale of diffusion and effusion processes can be of the order of 1 s, dependent on the chemical nature of the released reaction product. The emerging reaction products are mainly neutral, therefore they have to be ionized in an ion-source, before they can be extracted to the the electromagnetic separation units. For an element sensitive separation one uses laser-ionization.

4.2 Principle of Mass Measurements

4.2.1 ToF - Bρ Technique

The ToF - Bρ technique for mass measurements is based on measurement of the magnetic rigidity and the corresponding velocity of the ion [Lun03, Mat07]:

$$B\rho = \frac{\gamma m v}{q}$$

$B\rho$ is called magnetic rigidity and γ is the Lorentz factor

As an example, at GANIL [Bia89], the typical fight time (ToF) is approximately one microsecond for a flight path of about 82 meters. $B\rho$ is determined by position measurements at the magnetic spectrometer SPEG. The typical resolution is $\frac{\delta p}{p} \approx 10^{-4}$ [Bia89]. In order to identify the measured nuclei by A and Z the ToF $B\rho$ correlation has to be plotted versus the energy loss ΔE. The calibration of this method is done by reference masses. The low resolution power of about $2 - 4 \cdot 10^{-4}$ is rewarded by the accessability of very short-lived nuclei with very small production cross sections. This provides a rough mapping of the mass surface in an exotic region [Lun03].

4.2.2 ToF Measurements in Cyclotrons

The accuracy in ToF-measurements is limited by the length of the flight-path [Aug94]. The spiral motion in a cyclotron, in the range of kilometers, is an ideal solution for this limitation. Furthermore, the ion motion inside the cyclotron is isochronous. The applied cyclotron frequency ω_c yield the determination of mass over charge ratio.

$$\frac{\gamma m}{q} = \frac{B}{\omega/n} \tag{4.9}$$

This is described by:

$$\frac{\delta(m/q)}{m/q} = \frac{\delta t}{t} = \frac{\delta\phi}{\phi} \tag{4.10}$$

t is the mean-time of flight and ϕ is the accelerating frequency phase

In order to obtain accurate mass values, reference nuclei with well-known masses are used.

4.2.3 Mass Measurements in Storage Rings

The combination of the in-flight separator FRS and the experimental storage ring ESR [Fra87] is a perfect tool to explore nuclear properties of exotic nuclei [FGM07]. From the FRS the produced and separated fragments are injected and stored in the ESR. The stored ions travel on well-defined orbits and with cooling they can circulate for a long time (10^6 orbits per second) a basis for accurate time-of-flight and revolution frequency measurements. The average revolution time t of an ion is given by:

$$t = \frac{v}{C} \tag{4.11}$$

v is the velocity and C is the circumference of its orbit

In order to measure the masses of the stored ions, one has to determine the revolution frequencies f, which is related to the mass-over-charge ratio:

$$\frac{\delta f}{f} = -\frac{1}{\gamma_T^2}\frac{\Delta(m/q)}{m/q} + (1 - \frac{\gamma^2}{\gamma_T^2}) \cdot \frac{\Delta v}{v} \tag{4.12}$$

$$\gamma_T^2 = \frac{[\delta(p/q)/(p/q)]}{\Delta C/C} = \frac{1}{\alpha_p} \tag{4.13}$$

γ is the Lorentz factor and γ_T^2 is called transition point, this can be described by a change in path length, due to a corresponding change in the magnetic rigidity (p/q). C is the orbit circumference. α_p is called momentum compaction factor.

In order to obtain an accurate mass-over-charge determination from the frequency measurement one has to eliminate the 2nd summand in equation (4.12). Two different ion-optical modes of the ESR are possible to achieve the elimination of the 2nd summand: The 'Schottky mass spectrometry' (SMS) mode and the 'Isochronous mass spectrometry' (IMS) mode [Lit07].

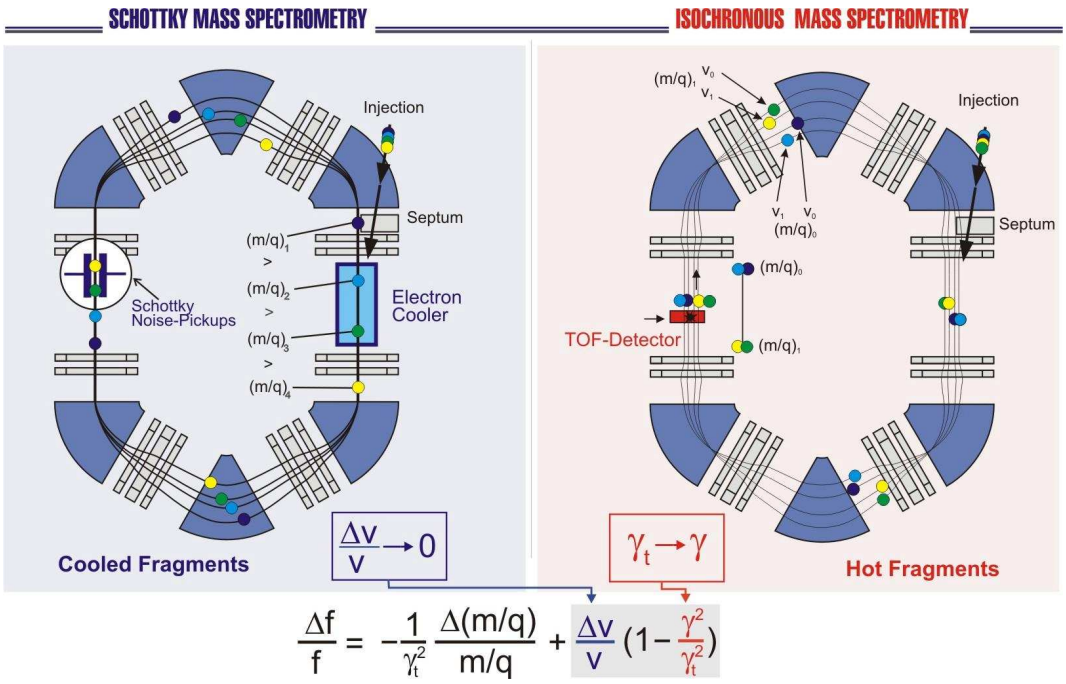

Figure 4.1: ESR - SMS (left) and IMS (right) Mode. Scheme of the two methods for mass measurements in the ESR.

Schottky Mass Spectrometry at the ESR

By cooling the beam inside the ESR by stochastic pre- and electron cooling (developed by Van der Meer (1985) [Van85]) or laser excitation (Madsen et al., 1999 [Mad99]) the velocity dispersion can be reduced. Thus, the second summand of equation (4.12) is continuously reduced [FGM87][Lit07]. The electron cooler merges a cool electron beam (small phase-space) with the hot ions (large phase-space) in the storage ring. The electron beam forces the ions to the identical mean velocity and temperature. This results in a reduced phase space of about $\frac{\delta v}{v} \approx 10^{-6}$. This cooling process takes several seconds if not minutes, therefore it is impossible to measure very short-lived isotopes ($\approx \mu$s to ms). To reduce the cooling time, stochastic precooling can be applied for half-life measurements. This is not applied for mass measurements, because the stochastic precooling would drastically reduce the number of reference masses. The non-destructive detection of the ions is performed via pickup electrodes, which are mounted a few centimeters away from the ions' orbit. A passing ion induces a signal on the plates, this signal is embedded in the 'Schottky noise'. The average revolution frequency is derived from the Fourier transformation of the whole signal. Together with reference masses inside the spectra, one can obtain the absolute mass value of the exotic nuclide. The mass resolution depends on reduction of the velocity spread (see equation (4.12)). The achieved mass resolution is typically about $7.5 \cdot 10^5$ (Geissel et al., 2001 [Gei01]).

Isochronous Mass Spectrometry at the ESR

In this isochronous ion-optical mode of the experimental storage ring ESR, the velocity of the ions match to the transiton point $\gamma_T = \gamma$ [Wol87]. Therefore, no cooling is required. Therefore, this method is applicable for very short lived fragments down to the m and μs-

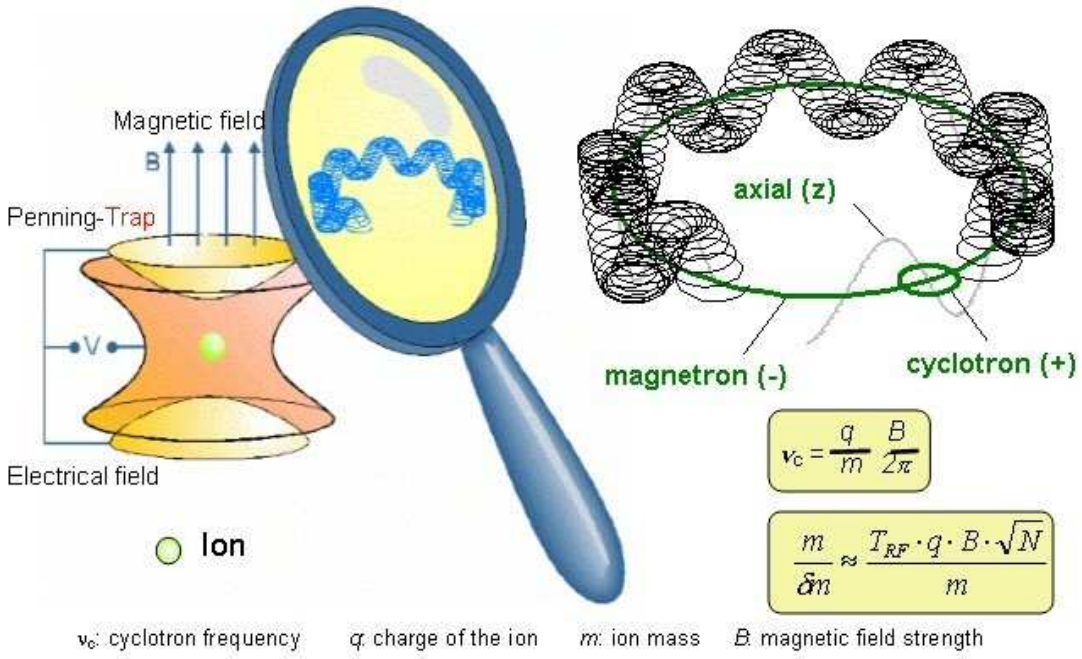

Figure 4.2: Schematic setup of the electrodes in a Penning trap (left) shows the vertical magnetic field and the hyperbolial electrodes. The trajectory (right) consists of the superposition of three eigen-modes, the axial, the magnetron and the cyclotron movement [Tri07, Bol92]

range. A time-of-flight detector records the revolution frequency of the stored ions. The Tof- detector consists of a very thin foil (e.g.17μg/cm^2). In this foil secondary electrons are released at each turn and thus provide the timing signal for Micro-Channel-Plates (MCP). After several hundred passages through the foil the ions get lost. The typical mass resolution is about 10^5.

4.2.4 Penning Traps

Penning traps are devices to store charged particles. The principle of these traps has been invented by Hans Georg Dehmelt (NP 1989).

A combination of an azimuthal quadrupolar electric potential and an axial magnetic field is created in a Penning trap to store ions [Kel02, Vor06, Bol92]. The ions' movement is a superposition of three harmonic eigenmotions (see figure 4.2). One mode is axial, the two other modes are radial movements. The magnetron motion has a specific frequency ν_-, and the modified cyclotron motion with frequency ν_+. The sum of both frequencies is equal to the cyclotron frequency of the ion.

$$\nu_c = \nu_- + \nu_-$$

A buffer-gas-filled Penning trap cools all three types of motion by collisions of the ions with gas atoms. These collisions reduce the amplitudes of the axial- and cyclotron motion, but increases the radius of the magnetron orbit. The radial modes of the stored ions can be exited by an external azimuthal dipolar or quadrupolar radiofrequency field. If the external RF field has the cyclotron frequency ν_c, the magnetron and the cyclotron motions are coupled. This leads to a constant conversion of energy between the modes, allowing to cool all three modes

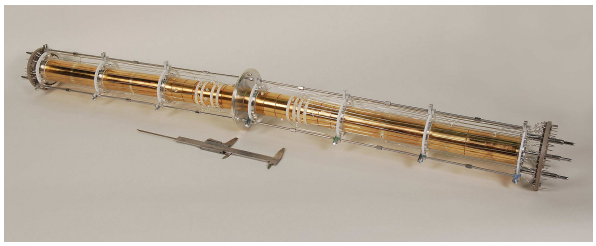

Figure 4.3: Penning trap of SHIPTRAP [GSI07]

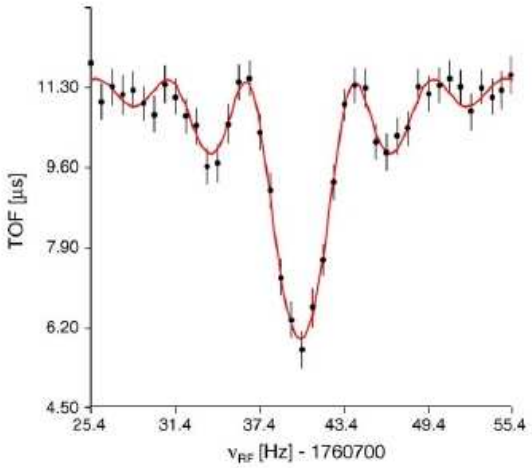

Figure 4.4: ToF-spectrum of a typical mass measurement with a Penning trap

simultaneously. This technique is applied in purification-Penning traps for isobaric isolation. The typical gas pressure in the purification-trap is 10^{-5}mbar. Although the ideal geometry of the electrodes in a penning trap are hyperbolic, often cylindrical Penning traps are used because of their larger inner volumina. Several ring electrodes are needed to correct the non-linear artifacts in the electric field. The ion sample can be stored in the purification trap for several hundred milliseconds. A precision Penning trap is installed behind the purification trap. The gas pressure in the precision-trap is much lower than in the purification-trap. A typical pressure is 10^{-8}mbar. Also, the geometry of the precision trap is often hyperbolic, to create almost perfect linear fields in the trap. Typical superconducting magnetic fields are 7 to 9 Tesla. For measurement of the ions frequency an azimuthal dipolar RF-field is applied to increase the magnetron motion. A second RF-field, an azimuthal quadrupolar field, is used to convert magnetron motion into modified cyclotron motion. Since the reduced cyclotron frequency is larger than the magnetron frequency, the ions start to gain kinetic energy. During the ejection of the ions towards the Multi-Channel-Plate (MCP) the ions pass an inhomogeneous part of the magnetic field. In this part of the field a force acts on the ions, which is proportional to their magnetic moment. This force converts radial energy into longitudinal energy. Ions, which have been resonantly-excited in the Penning trap, have a larger magnetic moment, thus these ions transform more radial energy into longitudinal energy. Therefore, these ions reach the MCP-detector in a shorter time-of-flight (ToF). This is shown in a typical resonance spectrum in figure 4.4. Penning traps are used as high-precision

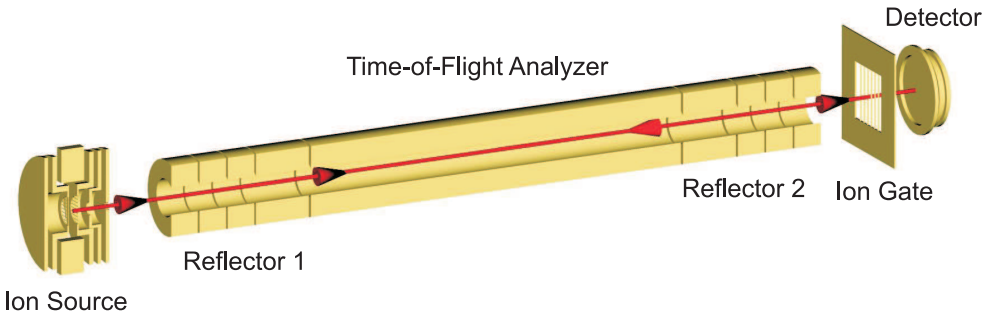

Figure 4.5: Multiple-reflection time-of-flight mass spectrometer[Pla07]. The segmented electrodes at each end of the device create a repulsive electrostatic potential, in order to reflect the ion bunch.

mass spectrometer with mass resolving power ($\frac{\Delta m}{m}$) of about 10^6. Mass measurements with penning traps are applied in various facilities, e.g. ISOLTRAP, LEBIT and SHIPTRAP.

4.2.5 Multi-Reflection Time-of-Flight Mass Spectrometer

A suitable way to access short-lived nuclei is a time-of-flight mass spectrometer (TOF-MS)[Wol03, Dic06]. The resolving power depends on the path-length of the ions inside the device. The idea of the MR-TOF-MS is to enlarge the path-length of the ions by multiple reflection on each end of the flight-path of the ions (figure 4.5). The measurement time is about a millisecond. This gives access to nuclides with short lifetimes, which cannot be measured with Penning Traps. In a pilot experiment, a resolving power of 100.000 has been achieved [Pla07].

Chapter 5

Mass Extrapolation

5.1 Theoretical Mass Models and empirical Mass Formulas

The comparison of accurately measured nuclear masses with theoretical models is a great challenge in nuclear physics[Bor93]. Several facilities around the world measure exotic nuclei and many theorists enjoy to improve mass-models. Different approaches are used to achieve this goal[Bor95, Jae88, Hau88] The really first theories have been developed by Weizäcker in 1935 and Bethe and Bacher in 1936. They derived a formula to describe the binding energy per nucleon for all isotopes with the liquid drop model[Roh94]. This global description is a very successful macroscopic approach.

$$E(MeV) = a_v A + a_s A^{2/3} - a_c(\frac{Z(Z-1)}{A^{1/3}}) - a_a \frac{(A-2Z)^2}{A} \pm \delta$$

The parameters are derived from experimental values (Table 1)

	Wapstra[Wap58](1958)[MeV/c^2]	Rohlf[Roh94](1994)[MeV/c^2]	Description
a_V	14.1	15.75	Volume
a_s	13	17.8	Surface
a_c	0.595	0.711	Coulomb
a_a	19	23.7	Asymetry
$\delta(even-even)$	-33.5	+11.18	Pairing
$\delta(odd-odd)$	+33.5	-11.18	Pairing
$\delta(even-odd)$	0	0	Pairing

Table 1: This table shows the evolution of the semi-empirical mass formula. Since 1958, the number of nuclei, which are included into the fitting routine of the mass formula increased dramatically, therefore the average error of the mass excess value prediction decreased down to 2-3 MeV.

Since then, more approaches have been developed to include more nuclear properties in mass models[Lun03]. The experimental observation of the nuclear shell structure, required new microscopic correction term. These correction term are the origin of the hybrid (microscopic - macroscopic (mic-mac)) and pure microscopic models. In 1966, Myers and Swiatecki modified the classical liquid-drop model with microscopic corrections[FGM07]. Shell effects have been taken into consideration. Additionally, a calculated pairing energy term has been

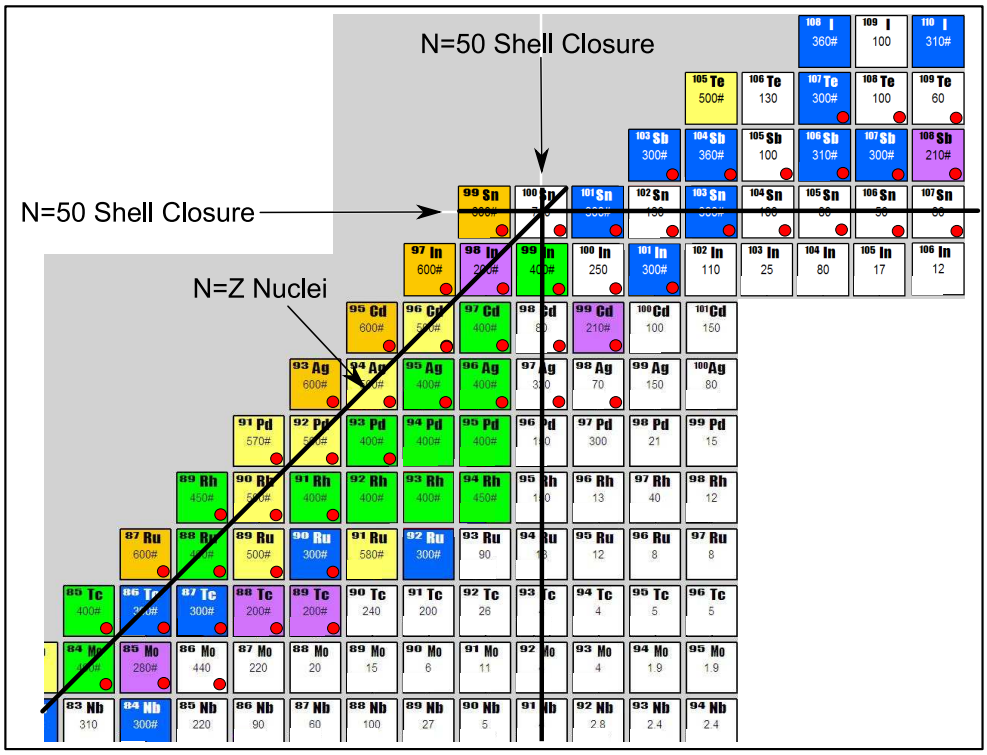

Figure 5.1: Mass extrapolations done by Audi and Wapstra et al. (2003)[Nuc03]. White squares are measured mass excess values in AME 2003. The colored squares are extrapolated values. The different colors represent the size of the error [keV] of the extrapolation(black: < 200; purple: 200-300; blue: 300-400; green: 400-500; yellow: 500-600; orange: 600-700; mandarin: 700-800; red: > 800;). The red dots mark nuclides, which are essential for the *rp*-process.

added for odd-odd nuclei and subtracted for even-even nuclei. A Wigner term has been included for nuclei that have the same number of neutrons and protons. This effect will be explained in the end of this section, because it is very important for the *rp*-process. Strutinsky has upgraded the liquid drop formula with shell corrections, calculated from a microscopic model[Str67]. The currently used Finite-Range-Droplet Model (FRDM) takes into account the finite range of the strong nuclear interactions and the diffuseness of the charge distribution[FGM07]. The Duflo-Zucker mass formula (1995) is a different mic-mac model approach. This method is based on pseudo potentials that describe effective particle interactions. The pseudo potential behave smoothly, i.e. the binding energies change slowly for A or Z.

The nonrelativistic Hartree-Fock model, is one of the earliest microscopic approaches. This model is based on the Schrödinger equation, where the potential results form the nucleon-nucleon interaction forces. The nucleons are described by wave functions. Knowing the particle interactions, e.g. nucleon- nucleon scattering it should be possible to calculate the binding energy of the nucleus and other properties, e.g. nuclear radii.

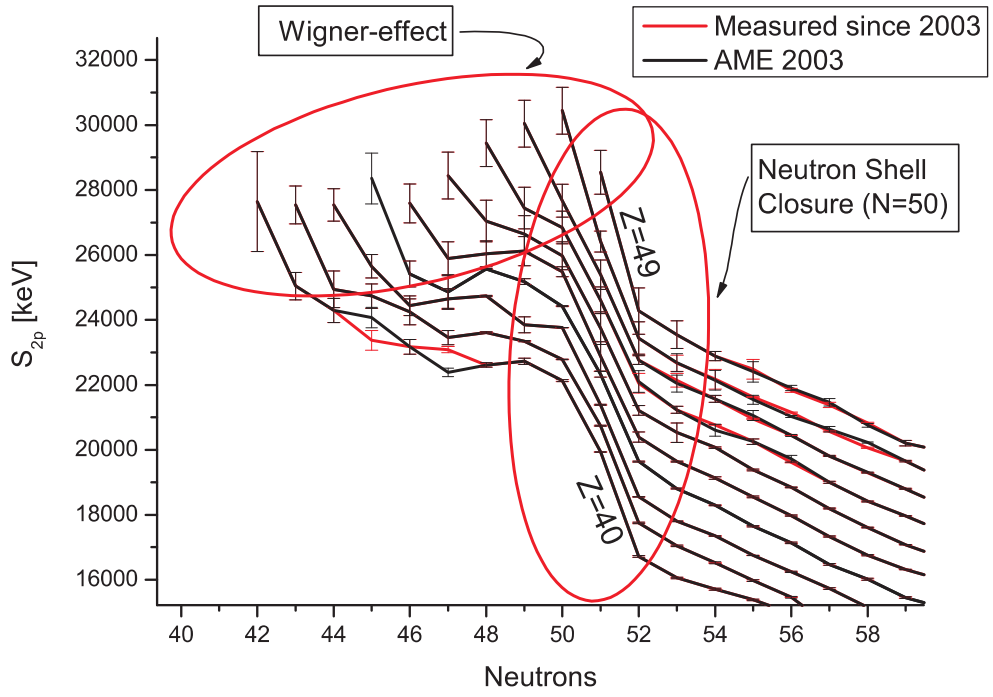

Figure 5.2: The figure shows the 2 neutron separation energy taken from AME 2003 (black) and measured separation energies of mass excess values since 2003 (red). The red bubbles mark the neutron-shell closure at N=50 and the Wigner-effect that causes a shift in the separation energies for N=Z nuclei.

5.2 Known and unknown masses in the region of the *rp*-process

Very exotic nuclei are important for the *rp*-process.[Aud03] figure 5.1 shows the measured and extrapolated masses, which are summed up in the AME 2003 list by G.Audi et al.. Due to new mass measurements in this region, it is possible to reextrapolate mass excess values. To observe the systematics in this region, several nuclear properties are plotted in this mass region. One looks for neutron- and proton-separation energy, also for 2 neutron- and proton-separation energy. These functions create a plane in a 3 dimensional space, thus it is often called 'mass surface'. Because of nuclear effects, like pairing energy, one obtain special behaviour, so one have to split these functions into, at least 4 parts: even-even and odd-odd nuclear configurations, also even-odd and odd-even compilations. These four sheets form four independent mass surfaces, which are nearly parallel in all points. These planes are charactericed by their specific pairing energies, e.g. the vertical distance between the even-even and odd-even layer defines the proton-proton pairing energy. Experiments, e.g. mass measurements show that these sheets are nearly parallel, which means that the pairing energies vary smoothly and slowly in dependence of N and Z.

This smoothness is only interrupted by important changes in nuclear structure, like shell and sub-shell closure, nuclear deformations and shape transitions and the 'Wigner' effect along the N=Z line (figure 5.2).

Thus, local mass extrapolations are possible. Previous extrapolations, which have been derived by Audi and Wapstra et al have been studied before. (2003).

Because of mass measurements of exotic nuclei, former systematic trends in separation energies and other nuclear properties can shift or show quite different behaviour. Therefore,

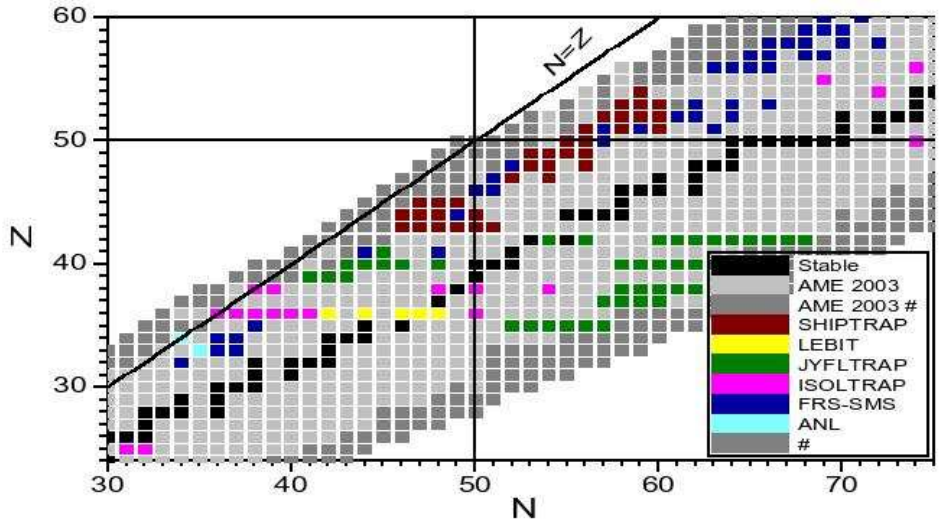

Figure 5.3: This chart of nuclides show newly measured masses since 2003. The color presents the facility that measured the mass excess with the smallest error bar.

it is essential to reextrapolate, in order to re-smooth the mass surface. Having a closer look on the A=80-105 region, one sees a linear behaviour of the separationen energies, until N=Z nuclei. The drop-down of the separation energy is caused by the previously mentioned 'Wigner' effect E_W [Lun03].

$$E_W = V_W \cdot exp[-\lambda(\frac{N-Z}{A})^2] + V'_W|N-Z|exp[-(\frac{A}{A_0})^2]$$

All parametrization variables can be varied, so that the fit delivers the best mass predictions. The second summand has been derived by Goriely et al in 2002, in order to improve the predictions for lighter nuclei.

In this work mass measurements have been summed up and illustrated in Figure 5.3, which have been taken since 2003 by SHIP-Trap, LeBit, JYFL-Trap, ISOL-Trap, ANL and FRS-SMS-group.

In general, the comparison of the new mass values to the current AME03 list, shows that in this mass region the average value for mass excess becomes significantly smaller (up to 700 keV). The average value is reduced by nearly 300 keV. This is a strong motivation for using the new mass values and new extrapolations as input for astrophysical network calculations. In the next section new extrapolations have been performed.

5.3 The Extrapolation

Considering the complexity of theoretical mass models, the extrapolations in this work take advantage of the 'smoothness' of physical observables, e.g. 2 proton and 2 neutron- separation energy. In total one includes S_{2p} for element- and isotone-chains and S_{2n} for isotones. By plotting these quantities, e.g. S_{2p} for isotone-chains (figure 5.7), one observes that these

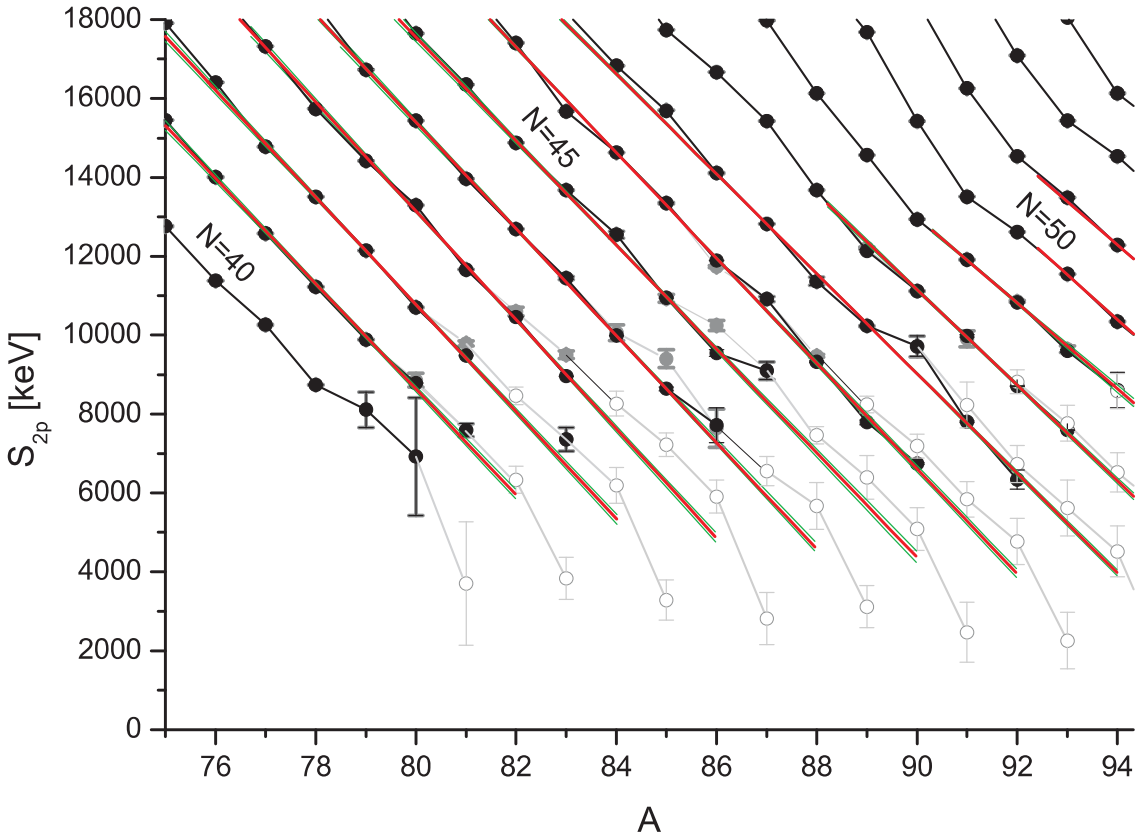

Figure 5.4: This plot shows measured separation energies (full grey circles) and extrapolated separation energies (open grey circles) of AME 2003. The black dots represent measured masses until today. The linear extrapolation (red lines) of the measured masses until today are surrounded by the confidence band (green) of the linear fit function. The fit function does not include the separation energies of N=Z nuclei, which are shifted, due to the Wigner-effect.

functions show a linear behavior. Thus, one can easily extrapolate these functions to unknown nuclei.

The error bar of the extrapolated separation energy is shown by a confidence band. Due to the 'smoothness' of the mass surface linear extrapolations are possible (figure 5.7 and figure 5.8). The slope of the linear functions is nearly the same for neighboring chains, this is not included explicitly. One considers nuclei with $N - Z \leq 8$ for the extrapolations, only. Therefore, local extrapolations have been performed. A general trend is observed, the former extrapolations are higher than the new extrapolations. This is in good agreement with the shift of the mass surface by the new measurements. A similar extrapolation technique is explained in reference [Bor95]. The two-proton separation energy of the 'N-Z=-1' nuclei have to be shifted by the 'Wigner effect'. The chains are extrapolated for all functions, afterwards the mass excess is determined by a weighted average (figure 5.5 and figure 5.6). In order to show the new positions of the extrapolated separation energies, the separation energies are recalculated and plotted in isotone and isotope chains (figure 5.8 and 5.7). Note, each last data point in the isotone- and isotope-chaines is shifted, due to the Wigner effect, therefore these points are not included in the linear extrapolations.

A full list of the extrapolated masses and the derivation from the former AME 2003 list

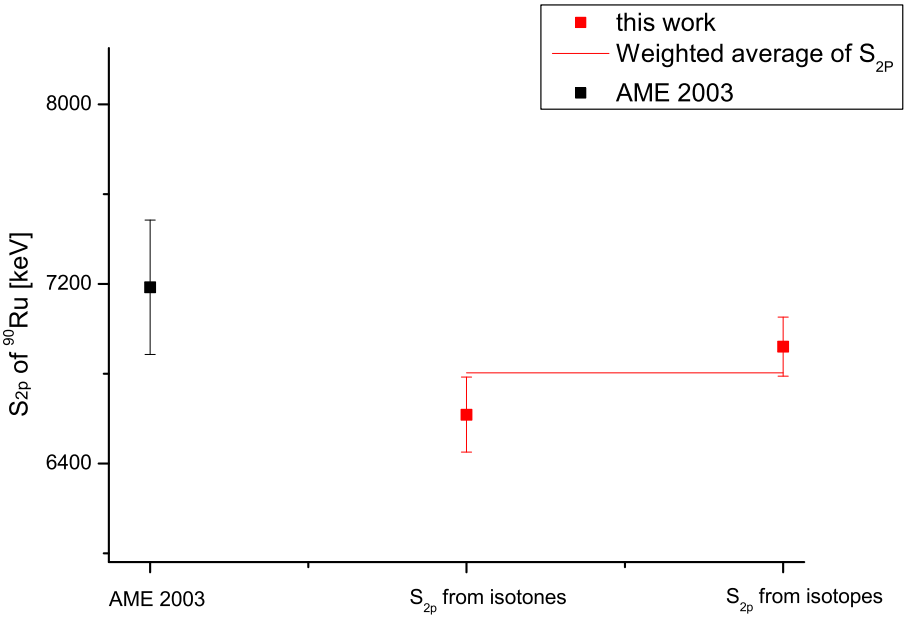

Figure 5.5: Weighted average of S_{2p} of ^{86}Tc(red line)((6804 ± 103)keV). The AME 2003 value for the separation energy (black point)((7190 ± 300)keV) is compared to the results of the extrapolations of this work (red points). ^{86}Tc has been selected due to its importance for the *rp*-process

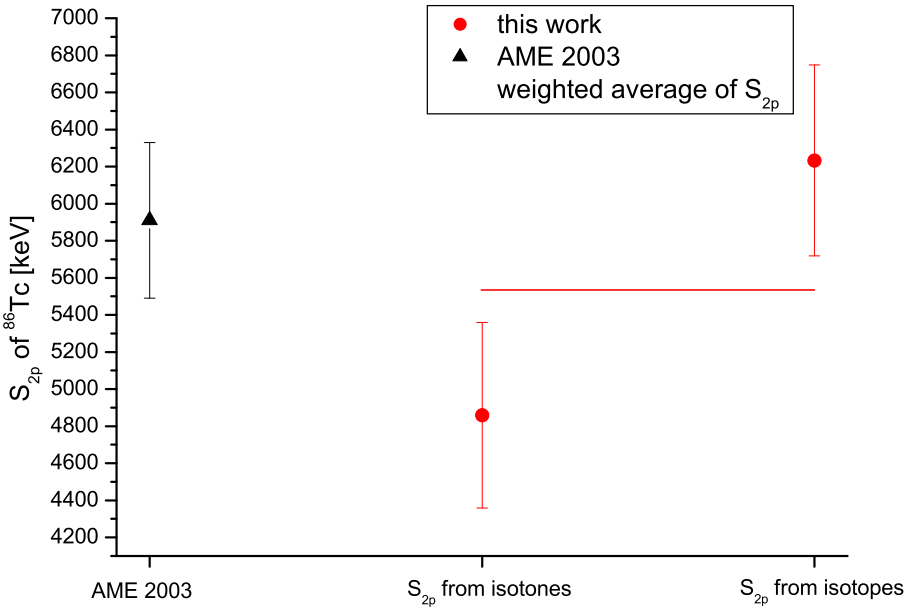

Figure 5.6: Weighted average of S_{2p} of ^{90}Ru(red line)((5528 ± 360)keV). The AME 2003 value for the separation energy (black point)((5910 ± 420)keV) is compared to the results of the extrapolations of this work (red points). ^{90}Ru has been selected due to its importance for the νp-process

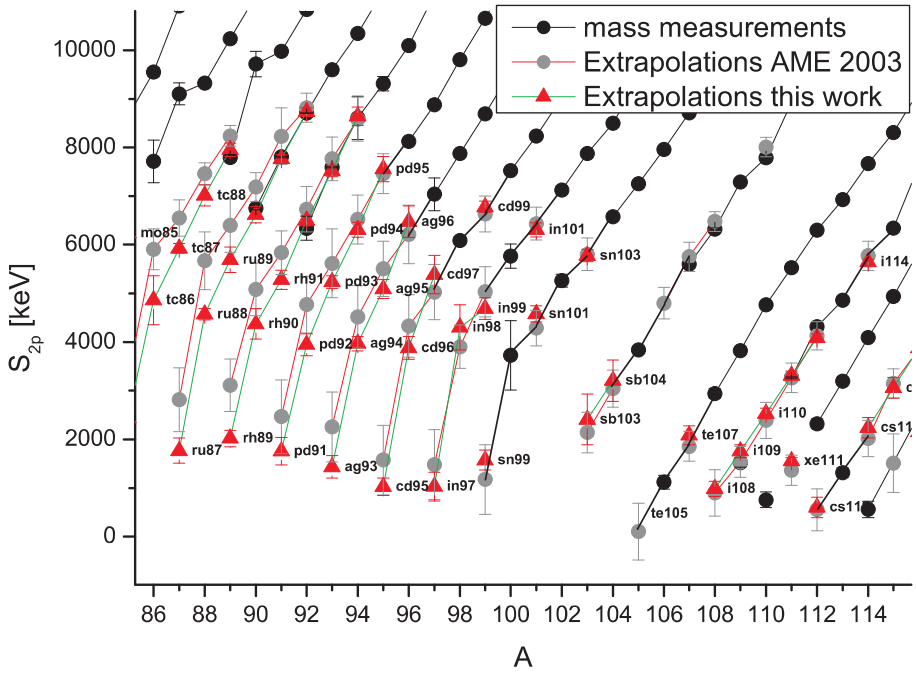

Figure 5.7: S_{2P} for isotope chains. The black dots are measured separation energies or separation energies calculated from two measured mass excess values. The grey data points are the former extrapolations, which have been performed by G.Audi and A.H. Wapstra et al. in AME 2003. The red points are the new extrapolations, which have been done in the course of this diploma thesis.

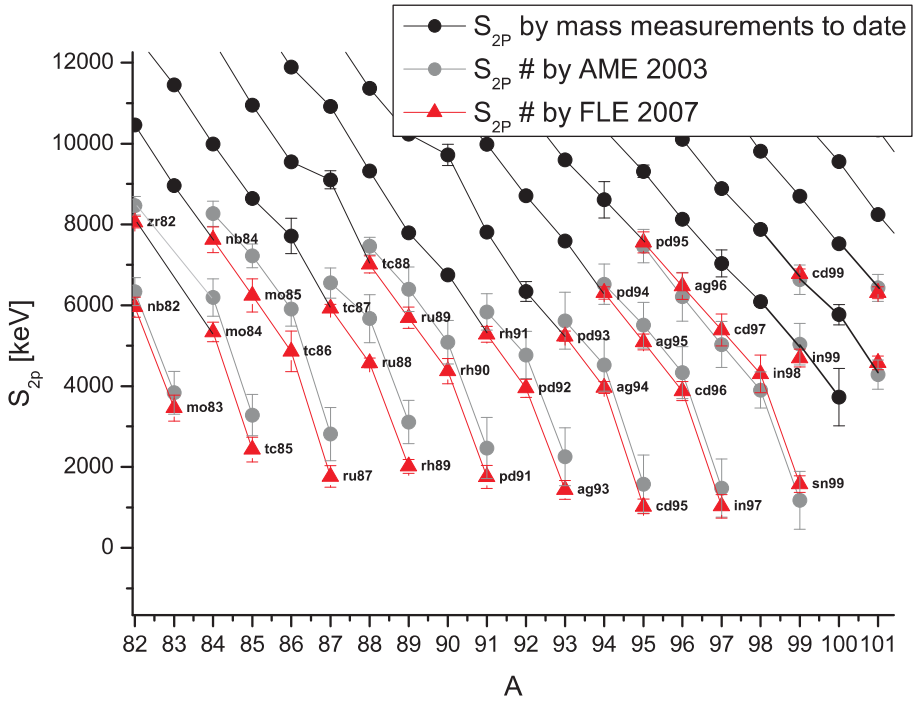

Figure 5.8: S_{2P} for isotone chains. The black dots are measured separation energies or separation energies calculated from two measured mass excess values. The grey data points are the former extrapolations, which have been performed by G.Audi and A.H. Wapstra et al. in AME 2003. The red points are the new extrapolations, which have been done in the course of this diploma thesis.

can be found in the Appendix of this work.

The Systematic Error of the Extrapolation

Each calculated and measured physical quantity has a statistical and a systematical error. The statical error is given by the number of data points and their error bars (figure 5.5). A systematical error, takes into account that data points are generally too low or too high, than predicted. It also deals with unknown physical circumstances, like a new physical effect that causes non-linearity in the extrapolations. In the extrapolations, one has estimate a systematic error. In order to estimate the systematical error of our extrapolation method, we apply it to the AME 2003 mass values. The extrapolated mass values have been compared with the newly measured masses since.

For example ^{84}Zr is extrapolated with AME 2003 values and is compared to the new measurement in 2007.

Such checks have been done for more previously extrapolated mass values. The predictive power of our present extrapolation method is demonstrated in table 2.

	Mass excess [keV] **Extrapolation**	**Error** [keV]	**Mass excess** [keV] **measured since 2003**	**Error** [keV]	**♯-measured** [keV]
^{92}Rh	-62914.1	295.07	-62971.33	34	57.23
^{93}Rh	-68666.9	257.75	-68999.51	11	332.61
^{94}Rh	-72587.13	146.33	-72945	447	257.87
^{90}Ru	-65019.39	409.52	-64868.93	10	-150.46
^{91}Ru	-68114.76	349.27	-68232.11	10	117.35
^{92}Ru	-74145.46	301.03	-74295.22	5	149.76
^{89}Tc	-67747.12	348.49	-67392.8	15	-354.32
^{84}Zr	-71477.61	101.07	-71418	6	-59.61

Table 2: This table sums up the mass extrapolations of mass excess values with AME 2003 data. The extrapolation is compared to the measurement values, which have been taken since 2003.

These results show that the extrapolation technique is valid and predicts well mass values and error bars. Although, in this comparison with recently measured masses, we have not observed systematical shifts, a typical systematic error of 100 keV is applied.

Result of the Mass Extrapolation

The result of our mass extrapolations in comparison to former AME03 extrapolations is shown in figure 5.10 for all extrapolated values in the region A=82-131.

The comparison shows a good agreement for nuclides with A100. The nuclides with A=82-100 show a systematic trend to higher mass excess values than predicted by AME 2003. This trend reflects the systematic derivation of the newly measured masses from AME 2003. The general trend in this region is a shift in mass excess of a few hundred keVs. The errors of the extrapolations have been improved by 50 to 100 keV. Figure 5.9 shows all nuclides, which have been measured and extrapolated since 2003.

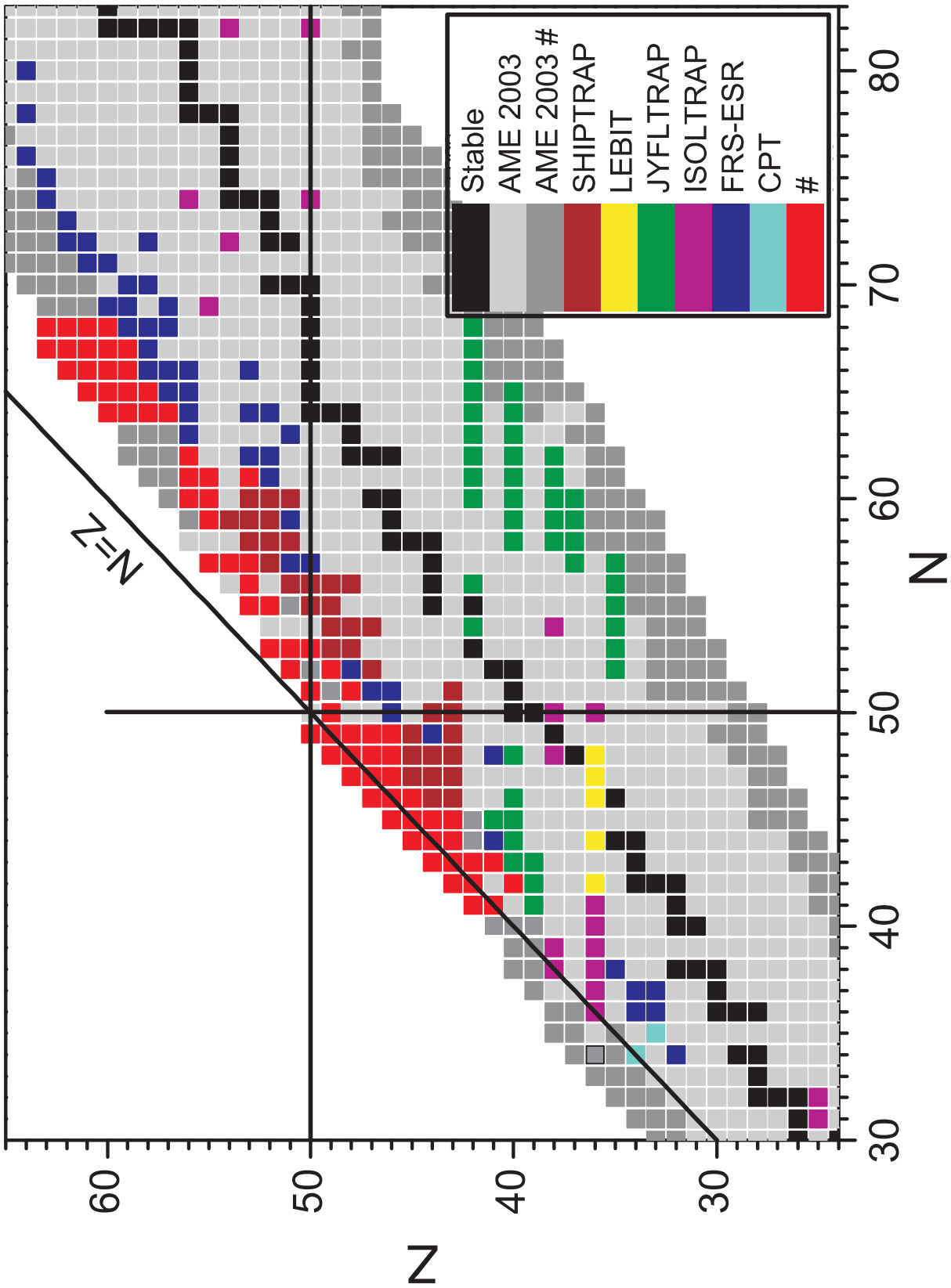

Figure 5.9: Chart of extrapolations 2007. In this chart (Neutrons vs. Protons), it is shown the current status of mass measurments. The color is explained in the legend box. Black squares mark stable isotopes. Squares in dark grey show the former extrapolations of AME 2003. Red squares mark the new extrapolations of this work.

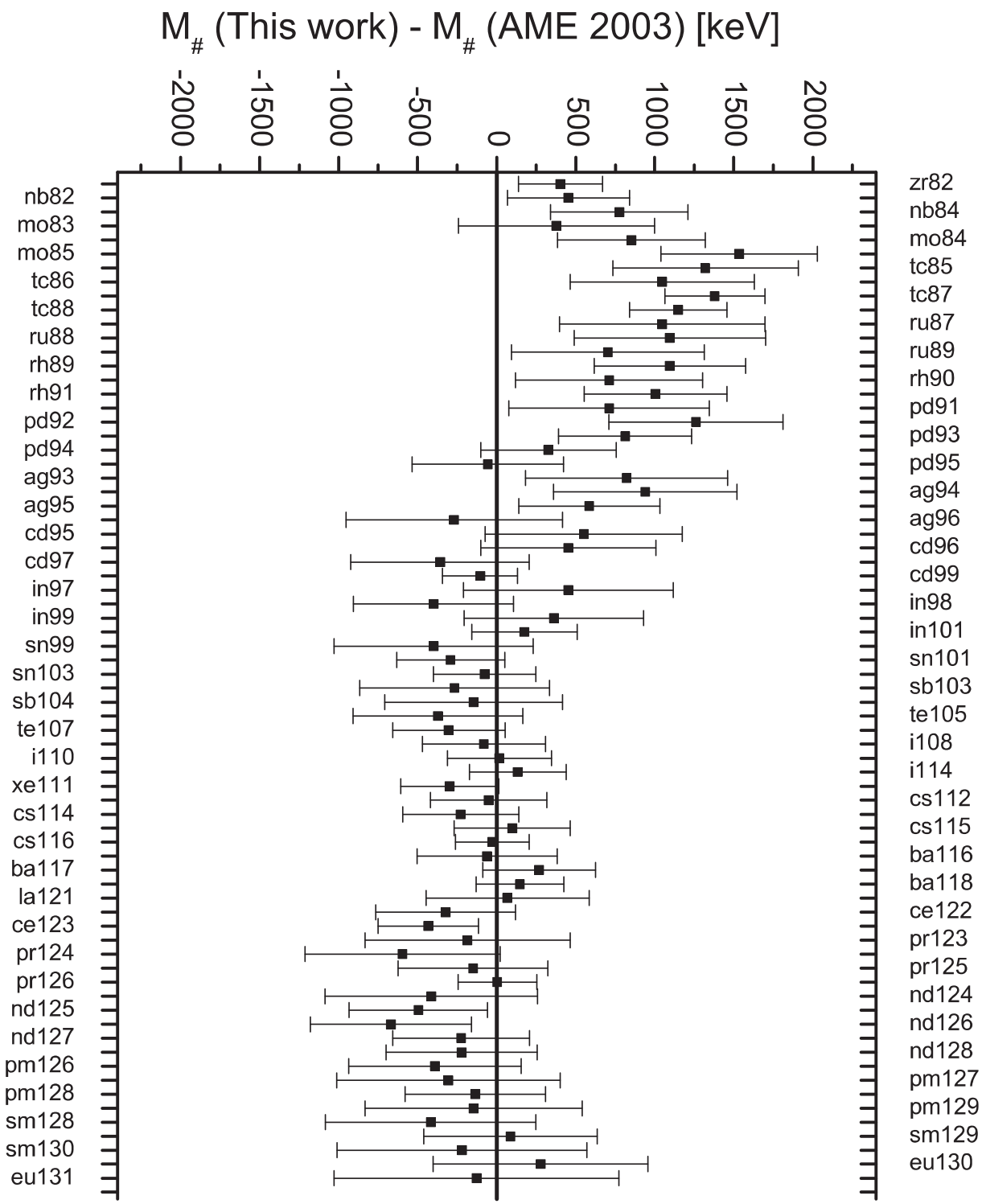

Figure 5.10: Final extrapolations 2007. The error bars of the differences are calculated by the root of the sum of the squares of the error bars from AME 2003 and the extrapolations of this work.

Chapter 6

Simulation Models

6.1 The Network Code

The nucleosynthesis processes in x-ray binary systems can be described by a simulation network code, which simulates the *rp*-process nucleosysthesis on an accreting neutron star. The code is selfconsistent and includes general relativity[Sch98, Sch04, Sch05, Fis07]. The accretion is described by one layer of matter. The actual temperature, opacity, entropy, chemical abundance and light emittance is calculated for every timestep. The accuracy, the size of the timestep is determined from the amplitude of the last change in the abundances. In order to assign the current chemical abundance, this simulation network reads the temperature depending reaction rate out of the data file 'reaclib'. The change of the abundance of a nucleus i is calculated via a nonlinear differential equation[Sch98a]

$$\frac{dY_i}{dt} = \sum_j N_j^i \lambda_j Y_j + \sum_{j,k} N_{j,k}^i \rho N_A < \sigma v >_{(j+k)} Y_j Y_k + \sum_{(j,k,l)} N_{(j,k,l)} \rho^2 N_A^2 < \sigma v >_{(j+k+l)} Y_j Y_k Y_l \tag{6.1}$$

λ_j is the decay and photodisintegration rate, $N_A < \sigma v >_{(j+k)}$ is the stellar two particles reaction rates, $N_A^2 < \sigma v >_{(j+k+l)}$ is the stellar three particles reaction rates. The stellar reaction rates are temperature depending.

The astrophysical forward reaction rates have been calculated by SMOKER [Rau01]. Furthermore, the reaction rate information is given by a Q-value and 7 parameters $(a_0 - a_6)$. They describe the temperature depending reaction rate $N_A < \sigma v >$[Rau00].

$$N_A < \sigma v > = \sum_i exp(a_{o_i} + a_{1_i} T_9^{-1} + a_{2_i} T_9^{-1/3} + a_{3_i} T_9^{1/3} + a_{4_i} T_9 + a_{5_i} T^{5/3} + a_{6_i} ln T_9)$$

By describing the chemical abundances of the network with the Saha equation (3.21) it is even possible to calculate the parameters $(a_0 - a_6)$ for the backward reaction rate[Rau00]. Applying the concept of chemical equilibrium for the reaction $a + b \rightarrow c$

$$\frac{dN_{ab}}{dt} = \frac{dN_c}{dt} = 0 \tag{6.2}$$

dN_{ab} is the number of particles of a and b, N_c is the number of product particles.

To achive our boundary condition, one has to claim:

$$N_a N_b < \sigma v >= N\lambda_c \tag{6.3}$$

$< \sigma v >$ is the stellar reaction rate, λ is the decay probability of decay per nucleus per time.

Using the equilibrium condition for chemical potentials ($\mu_a + \mu_b = \mu_c$), one obtains:

$$\frac{N_a N_b}{N_c} = \frac{g_a g_b}{g_c}(\frac{m_a m_b}{m_c})^{3/2}(\frac{kT}{2\pi\hbar^2})^{3/2} exp[\frac{-Q}{kT}] \tag{6.4}$$

$g_{a,b,c}$ are partition functions. They provide informations about the available phase space of the transition.

Therefore, it is possible to parameterize the backward reaction rate, similar to the forward reaction rate:

$$\begin{aligned} a_1^{backward} &= a_1^{forward} + 11.6048 \cdot \text{Q-value} \\ a_2^{backward} &= a_2^{forward} \\ a_3^{backward} &= a_3^{forward} \\ a_4^{backward} &= a_4^{forward} \\ a_5^{backward} &= a_5^{forward} \\ a_6^{backward} &= a_6^{forward} + 1.5(\text{for}(p,\gamma) - \text{reactions only}) \end{aligned}$$

The goal of this diploma thesis is the determination of the influence of mass uncertainties on nucleosynthesis processes, therefore the mass excess of 62 nuclei in the mass region A=80 - 105 has been varied in reference to its error bars. The mass excess of a nucleus has been increased or decreased by 2σ. The mass variation is included into the network simulations by editing the 'reaclib'-file, which contains all reactions of the network. The forward reaction rate is not altered, since the simulation with SMOKER for each reaction takes too long. By varying the backward rate, the branching ratio of waiting point nuclei are modified. The branching ratio in equilibrium states is described by Saha equation (3.21) and does depend strongly on the reaction Q-value. The Q-value is defined as the mass difference of the mother and the daughter nucleus.

$$Q_p = M(A-1,Z) - M(A,Z) + m_p \tag{6.5}$$

$M(A,Z)$ is the mass excess value (equation 4.2)of the nucleus with Z protons and A-Z neutrons. m_p is the mass excess of a proton.

By altering the equilibrium state, the branching of (p,γ)- and β^+-reactions is changed. The second simulation network code that has been used in this thesis describes the nucleosynthesis in neutrino-driven winds of supernova explosions. This simulation network is based on the reaction library file 'reaclib',too. However, the νp-process-network also includes (n,p) and (n,γ) reactions, which make the branching more complex. Typically, a produced neutron is instantly captured by proton-deficient nuclei. The calculation time of the rp- and νp- network code is typically (Opteron 185) 5 minutes. In order to produce a suitable amount of comparable runs (Definition follows), a master program varies not only one mass per simulation, but up to 3 masses. This is necessary, because the mass excess variation depends on other mass excess variation. The dependence can be subdivided into three groups, the impact of a specific

isotope, e.g.^{96}Ag changes, if a second isotope further down in the production path is altered, due to the increased or decreased particle flux through this isotope. The variation of the mass excess of a nucleus also decreases or increases the flux through it. A second possibility is the variation of e.g. ^{96}Ag and a second isotope, which is not part of the main production path. Thus, one does not expect an impact of the second modified isotope. The last case is the modification of e.g. ^{96}Ag and a isotope nearby, e.g. ^{95}Ag. The whole calculation time can be approximated:

$$(62 \text{ nuclei})^3 \cdot 5 \text{ minutes} \approx 200,000 \text{ runs} \cdot 5 \text{ minutes} \approx 800 \text{ days}$$

Because this is too long, the cluster of the NSCL (Jina) and the batch-farm of GSI have been connected via a master program. This thread manages all slave-CPUs from the clusters, by transmitting new input-files for the simulation-networks and picking up the calculated output-files of the simulation-networks. The slave-CPUs are connected to the master by Ethernet, but also by DSL-Internet connection. The cluster-network is able to accept every computer, which runs under an UNIX-based OS and which is connected stably to the Internet. The final part of the cluster-network is the full automatic-analyzer-network. After, the master thread delivered the first completed run (approximately 7 minutes on typical AMD Opteron 185 CPUs) of one slave CPU, the analyzer starts working. This program runs on two CPUs and watches the Log-script-file, which is produced by the master thread. This file lists, what has been done in every single run. So, the analyzer is able to find comparable runs, which only differ in one nucleus' mass change. Definition of comparable runs:

$$\text{Case 1: } M(^{98}Ag) \text{ - } 400keV \wedge M(^{82}Zr) + 400keV$$

$$\text{Case 2: } M(^{98}Ag) + 400keV \wedge M(^{82}Zr) + 400keV$$

Case 1 and Case 2 are comparable runs for ^{98}Ag. The analyzer compares all output-files of the comparable runs, to determine the impact of the mass-variation on light-curve, final abundance and production flow. Examples are given in the next chapter. The detailed comparisons are broken down to single integers, in order to simplify and quantify the compilation of all comparable runs. Thus, the changes in light-curves are judged by the absolute maximal amplitude and the absolute integral of the difference of both light-curves.

$$\frac{1}{N} \sum_{comp.runs} (|\int_0^{t_{end}} L_i dt| - |\int_0^{t_{end}} L_j dt|) \tag{6.6}$$

$$\frac{1}{N} \sum_{comp.runs} [max(abs(L_i(t) - L_j(t)))] \tag{6.7}$$

'Com.runs' means comparable runs 'i' and 'j'. N is the total number of comparable runs in order to normalize. 'L_i' and 'L_j' are the Luminosity in the run 'i' and 'j' $max(L_i)$ means the maximal value of L in the run i.

This is illustrated in figure 6.1. The impact on the production path is calculated with:

$$\frac{1}{N} \sum_{com.runs} (F_i^{Z,A,Z',A'} - F_j^{Z,A,Z',A'}) \tag{6.8}$$

$F_i^{Z,A,Z',A'}$ is the reaction flow from nucleus (A,Z) to nucleus (A',Z') of run i.

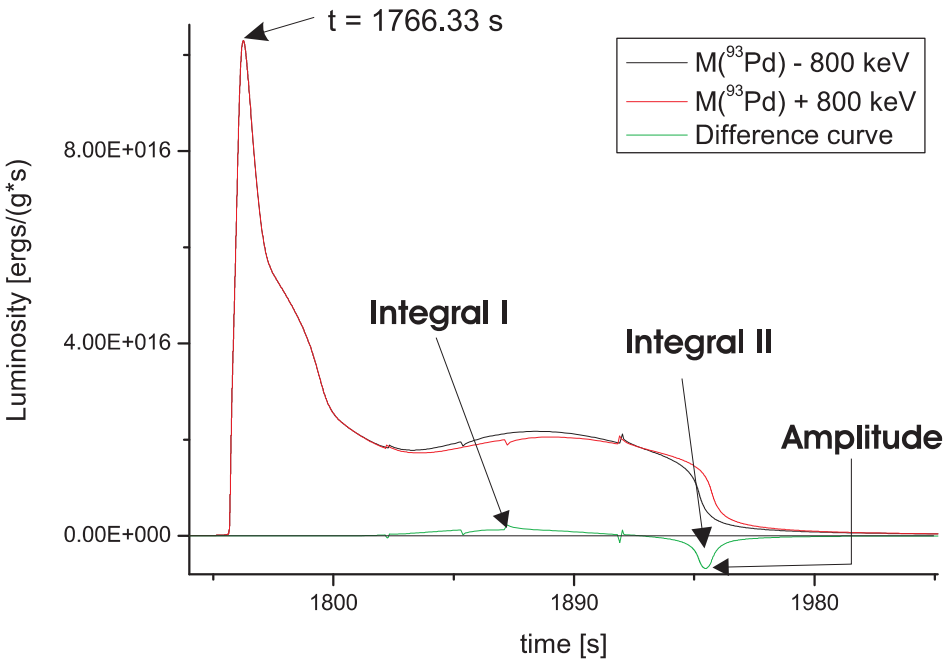

Figure 6.1: Comparison of two light-curves. The figure shows three curves. The black and the red line are results of the XRB-network calculation. The green one is the difference of both light-curves. Integral I is the area of the difference curve above 0. Integral II is the area below 0. For comparision of different runs, one calculates the absolut sum of both integrals. The second criterion is the maximal amplitude of the difference curve, which is caused by a decreased or increased burntime.[XRB]

The final abundances are sorted by their atomic mass number A, e.g. in figure 7.14. Like in the light-curve, the information is summed up. The first way is given by this formula:

$$\frac{1}{N} \sum_{com.runs} (\sum_{A} \frac{Y_i - Y_j}{Y_i + Y_j}) \tag{6.9}$$

This formula describes the standard derivation of every single difference in abundances.

In this figure 6.1, one observes a typical impact on the light-curve in a x-ray burst.[Fis04] In order to quantify the change, the light-curve (mass increased) is subtracted from the light-curve of the other case (mass decreased). The resulting function is shown in the figure (green curve). This curve is characterized by the absolute integral, which is divided into two parts. The second characteristic is the absolute amplitude of the resulting peek of the green curve.

Chapter 7

Simulation Results

7.1 The Impact of the New Mass Measurements and Extrapolations on the *rp*-Process

Several mass measurements have been performed in the A=80 to 105 region of the *rp*-process since the latest mass evaluation AME 2003 [Aud03]. These new measurements allow for new extrapolations of exotic nuclei. The proton separation energy is very important for the *rp*-process, which is governed by (p,γ) and (γ,p) reactions. In this section, simulation results for the process, calculated with the old mass values that are taken from the AME 2003 list, are compared with simulation results, which take into account the new mass measurements and extrapolations. The mass measurements since 2003 show a systematic trend in the mass region A=80 to 100 to larger mass excess values. The most significant change can be observed for ^{85}Mo, the mass excess of which has been increased by 1.5 MeV (chapter 4).

Typically, the final chemical composition is the most sensitive physical quantity as result of *rp*-process nucleosynthesis simulations, therefore the discussion focusses on the chemical abundance for both cases (AME 2003 mass values and the newly extrapolated values (figure 5.10)).

For a detailed investigation of the impact of the new mass measurements and mass extrapolations, the reaction library is modified to include changed backward reaction rates, according to the change in the separation energies (Section 5.1). Afterwards, the network code is executed with the unmodified reaction library, based on AME 2003 masses, and with the modified reaction library, which is based on the new mass measurements and extrapolations. In figure 7.1 one observes new peaks (red curve) at A=86 and A=90. The masses of the A=86 and A=90 isobars have been changed by up to 1 MeV (^{86}Tc), but the shift follows a systematic trend, therefore the Q-value changes are smaller. The diagram of the abundance versus mass number shows an overview on the abundances, which are independent of any β-decay occurring at the end of the *rp*-process, because the mass number stays constant for weak interactions. Especially the new peak at A=86 is significant and indicates a large impact of the new mass values on the nucleosynthesis process model. Therefore, this peak is investigated in more detail below. The enhancement of the mass channels A=86 to 90 goes together with decreased abundances in the mass channels A=76 - 85 and 93 - 104.

In figure 7.2, the abundance versus every single isotope is shown. The nuclides ^{86}Zr, ^{93}Tc and ^{90}Mo show the largest difference to the AME 2003 calculations. These nuclei are close to stability, therefore the error bars of the mass excess values are rather small (between 4 and 30

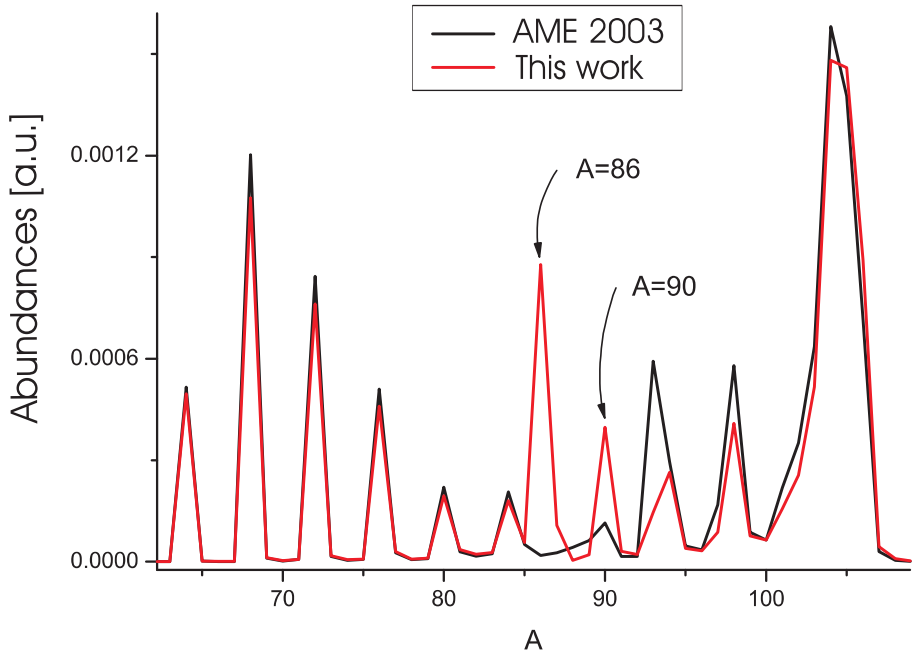

Figure 7.1: Comparison of final abundances produced in the simulation of a type II x-ray-burst (settings are taken from [Sch98]). The black curve shows the abundances calculated with the mass values of AME 2003. The red curve shows the abundances for the extrapolated masses obtained in this work [XRB].

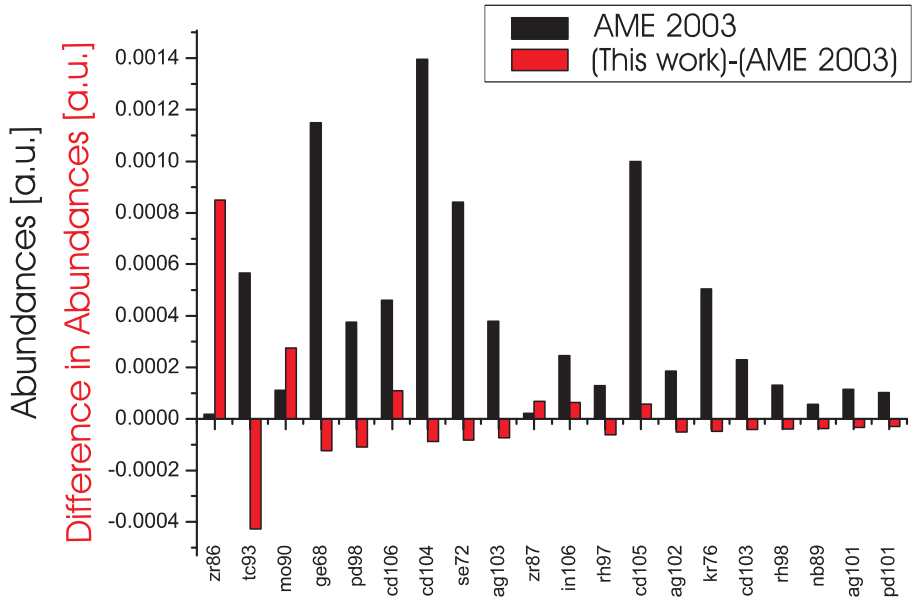

Figure 7.2: Illustration of the influence of the extrapolation on individual nuclides. The black bars show the final abundances for AME 2003 mass values. The red bars show the difference between the final abundances obtained using the AME 2003 and the newly extrapolated mass values [XRB].

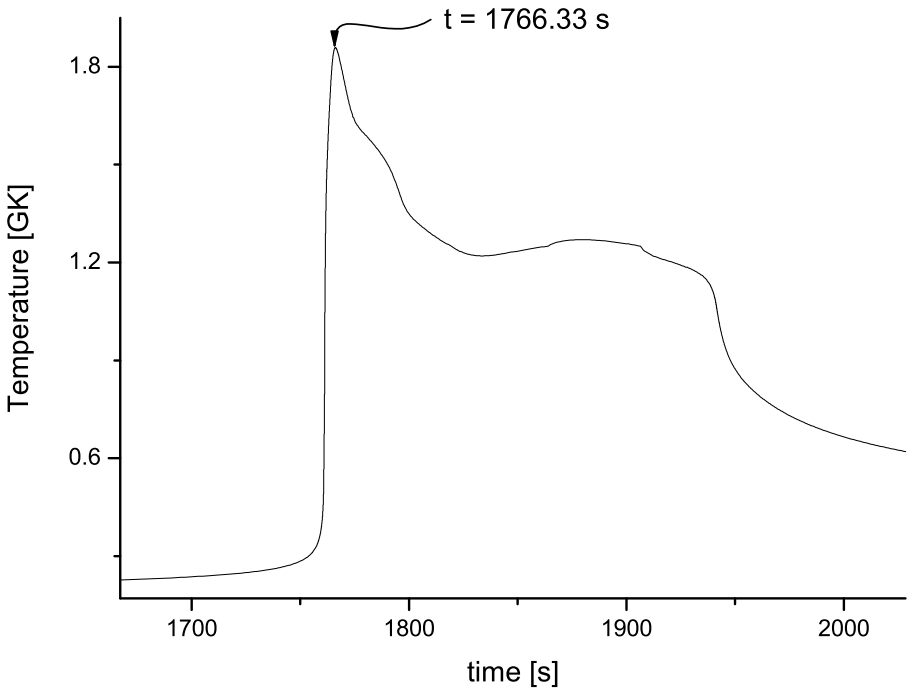

Figure 7.3: Time development of the temperature in the thermonuclear runaway in a type II x-ray burst [XRB].

keV). These nuclei are produced by β^+-decay only. This is reasonable because of the relatively long burst time of $\sim$ 200 s, in respect to the short lifetimes ($T_{1/2} \sim 5$ s). In figure 7.4, one observes the time development of the abundances during the x-ray burst for selected nuclides. The temperature determines the different stages in an x-ray burst (Explanation of x-ray bursts is given in section 3.3). The time development of the abundances mirrors the different stages in an x-ray burst (compare figure 7.3 with figure 7.4). The first abundance peak at $t \approx 1766$ s corresponds to the point at which the peak temperature ($T9 \approx 1.8$) is reached (figure 7.3). During the temperature peak, the creation of heavier elements is possible, however, due to the photodisintegration reactions these heavy elements are destroyed immediately after the temperature drops down. At $t \approx 1940$ s the temperature decreases from 900 MK to below 650 MK. Due to the decrease of photodisintegration reactions ((p,γ) and (n,γ)), heavier nuclei start to freeze out.

In the figure different circles outline important changes. Bubble 4 shows the decreased proton consumption for the calculations with the newly extrapolated masses. Additionally, one observes that the proton capture reactions start earlier for the AME 2003 case than in the new case (bubble 1). Bubble 3 marks the time development of the neutrons. Due to the low neutron density in the layer, the difference for both cases is quite small, too. Neutron capture reaction flows are several magnitudes smaller than proton capture flows. Bubble 2 points out the dramatic change for the ^{86}Zr abundance. The pink line, shows that the production of ^{86}Zr starts earlier (35 seconds) in the calculation with newly extrapolated masses. Additionally, one has to consider that ^{86}Zr is not produced by proton capture reactions in the *rp*-process, but via β^+-decay. The lifetimes of ^{86}Tc (55 ms), ^{86}Mo (19.6 s) and ^{86}Nb (88s) are still comparable to the typical burst time (200 s), however ^{86}Zr is the first nuclide in the A=86

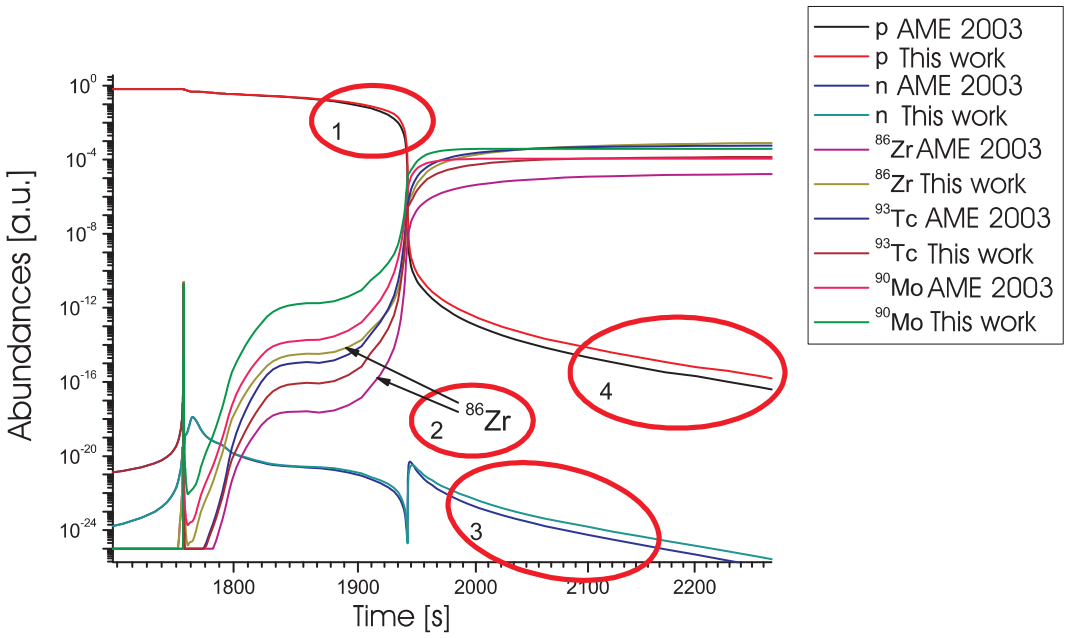

Figure 7.4: Time development of abundances of protons, neutrons and key nuclei for both mass sets (AME 2003 and this work). The numerated bubbles mark events, which are discussed in the text. Settings: [XRB].

chain with a much longer lifetime (16.5 h), therefore in the simulation the β-decay production channel stops at ^{86}Zr. Additionally, ^{86}Zr undergoes electron capture reactions only, which depend on the degree of ionization of the plasma. Therefore, one concludes that ^{86}Zr does not have to cause the modification of the production path, but other A=86 isobars, which are located directly in the production path.

Figure 7.5 shows the production path of the *rp*-process with AME 2003 masses and the newly extrapolated masses. There is a pronounced reduction of flow in the Sn-Sb-Te endcyle [Sch01] Additionally one observes stronger β^+-decay fluxes. The time development of the abundances and the production flow shows that with the new mass values the production of heavier nuclei in the mass region A=80 to 100 occurs faster than with the AME 2003 values. This is in good agreement with the systematic trend of the mass values and mass extrapolations (figure 5.10), which cause an increased proton-capture rate. However, the production of isotopes heavier than A=100 is slower because of the decreased proton-capture rate. Due to the limited burst time of about 200 seconds the decreased proton-capture rate causes a higher abundance of nuclei closer to stability with A=90 to 100.

Difference in the time development of the abundances of Ru, Tc and Mo isotopes for the different mass sets is presented in figure 7.6. One observes a clear enhancement of ^{86}Mo (c). The structure of the time evolution of ^{84}Mo is caused by a slight time shift in the burst process, however after all the final abundance is unaffected. ^{86}Tc shows the same behaviour, but to a much smaller extend. The graph in the middle (b) shows also the large underproduction of ^{87}Tc and ^{88}Tc. Interesting is the visible time shift of both peaks. The top graph shows the unaffected abundance of ^{87}Ru and the underproduction of ^{88}Ru and ^{89}Ru. One sees clearly that the abundance of ^{86}Mo is strongly increased for the new extrapolations (c). This is also the reason for the enhancement of the mass channel A=86, as described above. Having a closer look at the time developement of ^{86}Mo in figure 7.6, one notices that the destruction of

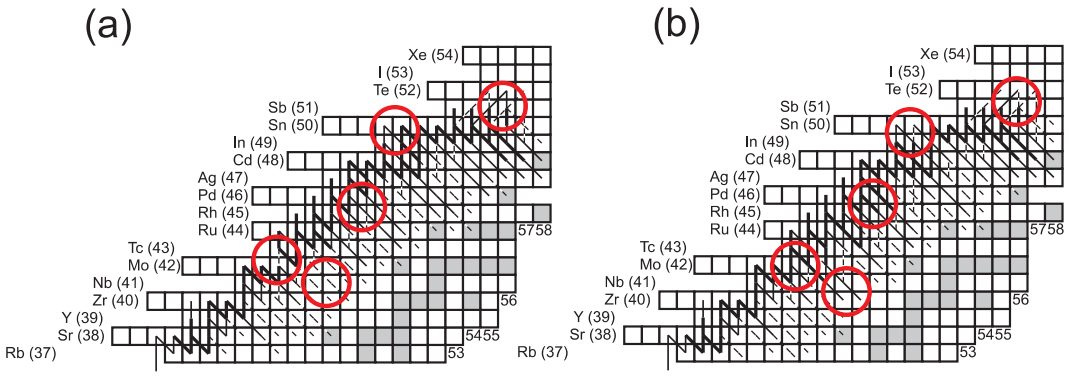

Figure 7.5: The production flow of the *rp*-process for different mass sets. (AME 2003 (a) and this work (b)). The red circles mark significant differences in both production flows. The flow is shown as black lines in logarithmic scale (dashed line: 10^{-3}; thin line: 10^{-2}; thick line: 10^{-1})The flux is normalized on the 3α-reaction. Diagonal lines represent β-decay reactions. Vertical lines represent p-capture and photodisintegration-reactions. Vertical lines close to the p-dripline often end up in a nucleus that does not undergo β-decay. These vertical lines present equilibrium states of (p,γ),(γ,p)-reactions [XRB].

its abundance can be approximated by an exponential decay with a half-life corresponding to the β^+-half-life of ^{86}Mo. Therefore, one concludes that nearly all ^{86}Mo ions undergo β^+-decay into ^{86}Nb.

In order to understand the changes in abundance, one should take into account the Q-value changes of nuclides in the vicinity of ^{86}Mo. This region of the chart of nuclides is shown in figure 7.7. One observes a global and a local effect of the mass extrapolations. The global effect is a systematic trend of the mass surface to higher mass excess values. In particular, accurate measurements have been performed for ^{85}Nb and ^{86}Nb with error bars of 28 and 6 keV. The measured values differ 700 keV from AME 2003. However, the extrapolation show that the systematic shift ends for nuclei with A=100. This causes an increased production of nuclides in the region A=82-105. The mass excess values of the nuclides ^{86}Mo and ^{87}Mo used in this simulation do not follow this global trend, because these nuclides have been measured before 2003 with a relatively large error (400 keV), but not since then, therefore they have not been included in the extrapolation. One observes that thus ^{86,87}Mo do not follow the linear trend in the two proton and neutron separation energies (figures 5.7 and 5.8). Therefore, the proton-separation energies around ^{86}Mo are changed strongly. This local divergence causes a dramatic overproduction of ^{86}Mo, ^{86}Nb and the quasi stable ^{86}Zr. In order to investigate this local effect in the mass surface, one has to remeasure this nuclides with smaller error bars.

7.2 The Impact of the New Mass Measurements and Extrapolations on the *νp*-process

The network calculations for the *νp*-process include proton- and neutron-capture and β-decay reactions. In order to observe the impact of the new extrapolations, one modifies the Q-values of the relevant reactions, therefore the equilibrium state of (p,γ)-(γ,p) and (n,γ)-(γ,n) are changed. Due to the systematic trend one can observe for the extrapolations, the Q-value do not change dramatically, however the mass region A=80 to 100 is systematically shifted, which is in good agreement with the mass measurements in this mass region. The final abundances (figure 7.8) show three increased peaks for A=100 to 102 for the calculations with the newly

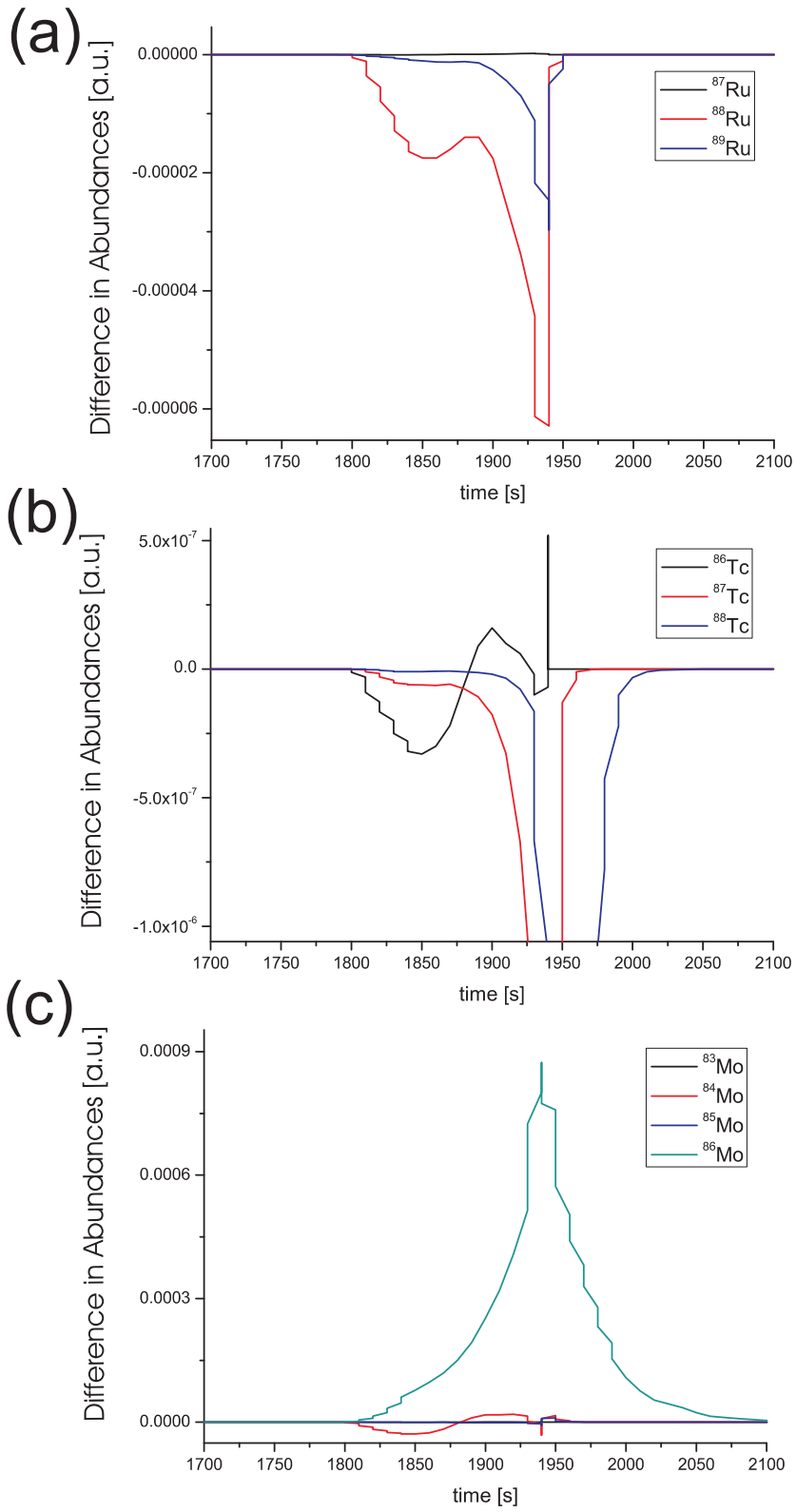

Figure 7.6: The figures show the time evolution for the isotopes of Mo, Tc and Ru. The color of each graph is explained in the legend box. The difference is given by $Y(t)_{thiswork} - Y(t)_{AME2003}$ [XRB].

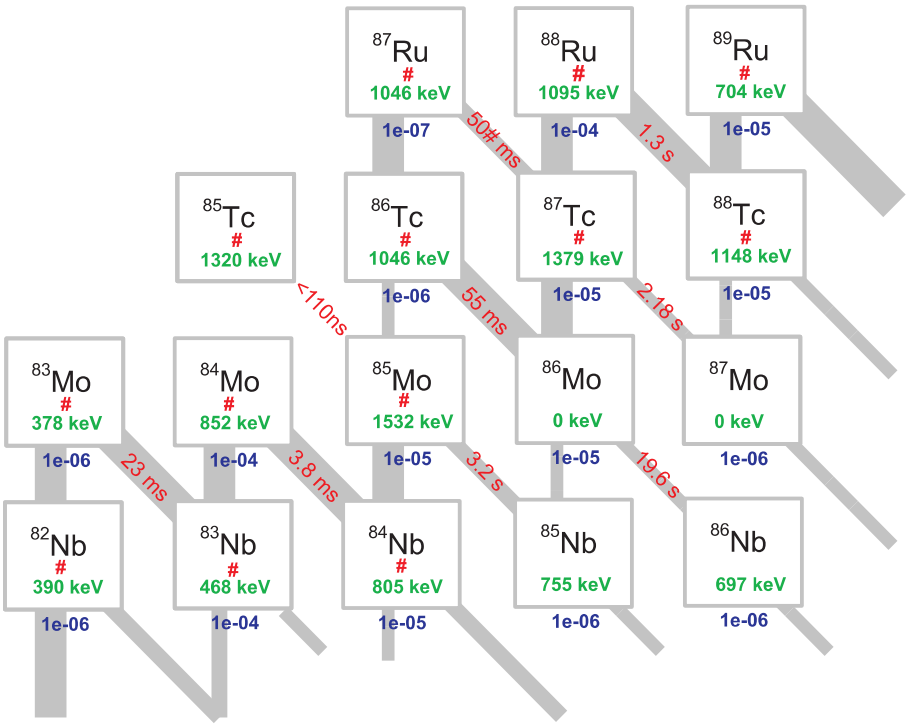

Figure 7.7: The figure shows the nuclides in the neighborhood of ^{86}Tc. The Q-value shift (this work-AME 2003) is shown in green. The maximum abundance of the nuclide is shown in blue.The red '#' marks extrapolated mass excess values.

extrapolated masses. The peaks at A=106 to 110 are slightly decreased in respect to the calculation with the AME 2003 masses.

In the direct comparison to the previous calculations in section 6.1 for the *rp*-process, one notices a similar behaviour in the final abundances, i.e. the overproduction of lighter nuclei A=86 to 95, and the underproduction of nuclei around A=100 and an underproduction of nuclei above A=100 (figure 7.8). However the changes in the A=86 to 95 region is negligible in respect to the changes in the region around A=100. Figure 7.9 shows the development for individual nuclides. In order to provide a better overview, figure 7.9 shows only nuclides with large differences in the final abundances.

One observes (figure 7.9) the impact of the newly measured and extrapolated masses on ^{100,102}Pd. Additionally, one notices a systematic decrease of the abundances for masses above A=106. However, the relative impact of the new extrapolations on the *νp*-process is rather small, compared to the impact of the masses on the *rp*-process. In the last figure 7.10, one observes the flow, for the different mass sets. On top, one sees the production flow for AME 2003 masses. The changes are marked by circles. In comparison to the new mass set, one notices the smaller flow for p-rich nuclei, which are close to the proton dripline above Z=47 to 50. Additionally, one notices the differences in the $\beta^+/(n,p)$- reaction channels.

Several publications have suggested the investigation of mass dependencies on the *νp*-process [Pru06, Fro06]. However, this work shows that masses have a smaller impact on the *νp*-process than expected. The maximum change in the production flow, due to the new extrapolations, amounts only to 5% in respect to the former flow value. In comparison, the flow deviations in the *rp*-process go up to 14%. The typical sensitivity of the final abundances

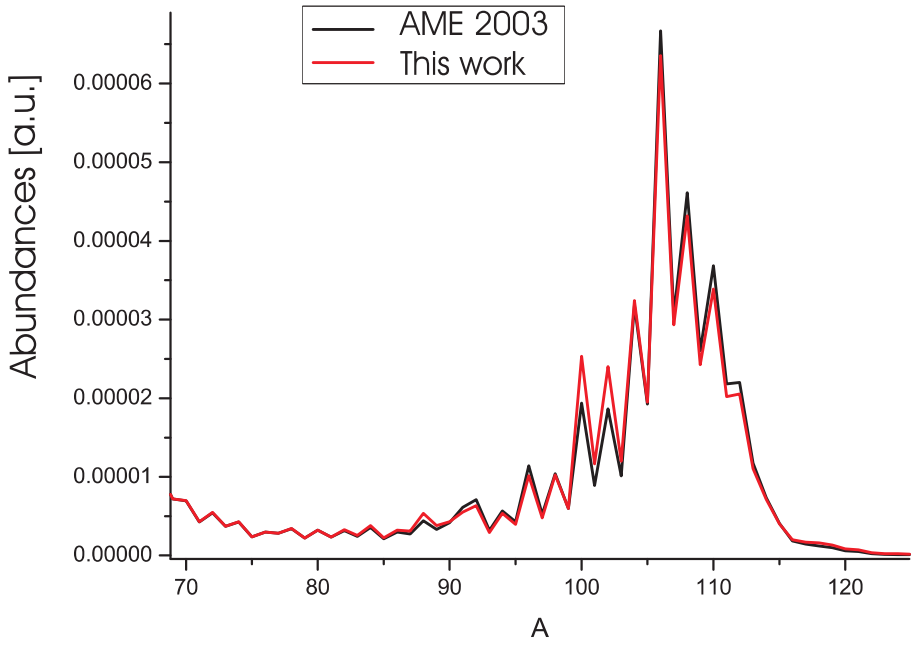

Figure 7.8: Comparison of the final abundances of the νp-process for two different mass excess value sets [NUP].

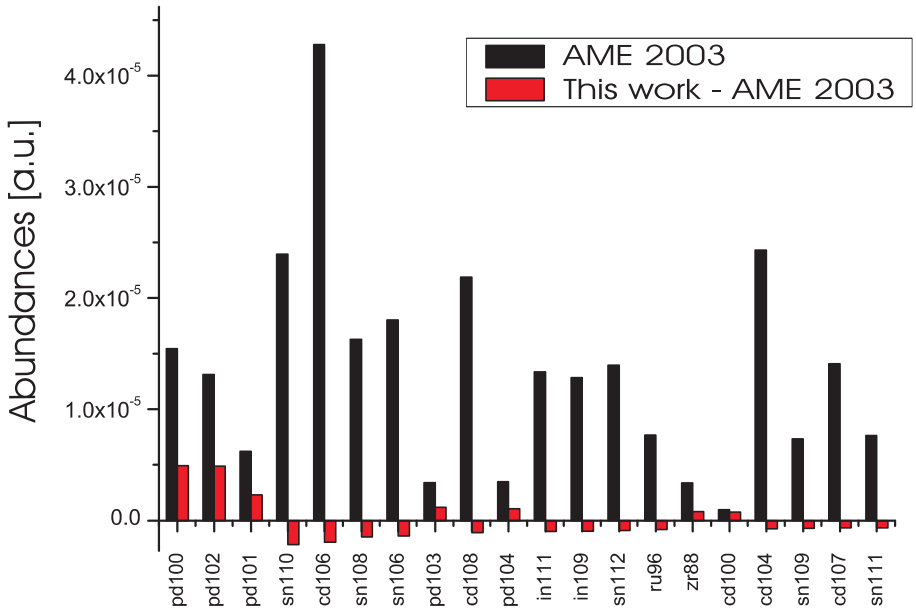

Figure 7.9: The final abundance with AME 2003 masses and the difference between the abundances with the newly extrapolated masses [NUP].

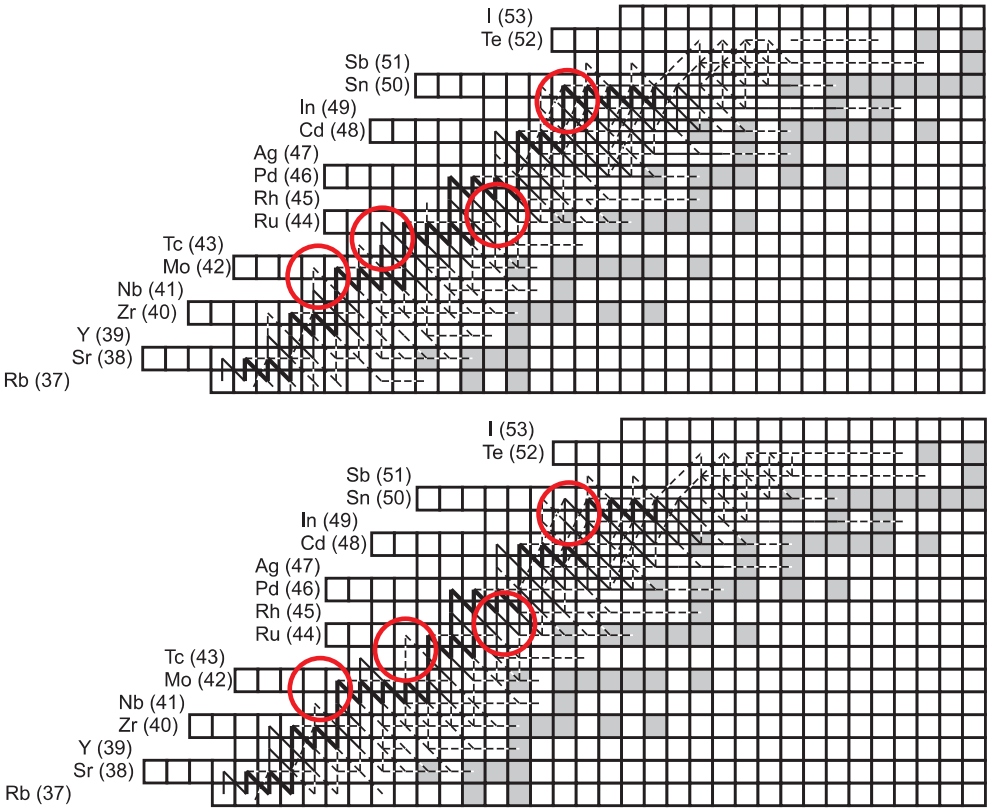

Figure 7.10: Illustration of the flow of the νp-process for AME 2003 and newly extrapolated masses [NUP].

in the νp-process on masses is about 15% to 20%, which is much smaller than in the rp-process. The reason for this that the νp-process proceeds in a less exotic region of the chart of the nuclides than the rp-process, where masses are known more accurately. In addition, the νp-process provides more reaction channels from one nuclide to the next than the rp-process (neutron-captures and (n,p)-reactions). Therefore, a blocked reaction channel can be bridged via other reactions. A detailed discussion of the weak dependence of this nucleosynthesis process on mass excess values and the enhancement of the heavier mass channels (A=100 to 110) is given in in chapter 6 (7.4.2 and 7.4.2)

7.3 Variation of Mass Excess Values: X-Ray Bursts

7.3.1 Overview

The rp-process consits mainly of α- and proton- capture reactions, photo disintegrations and β^+- decay. Schatz et al. have shown that this process cannot create nuclei with more than 52 protons, due to the Sn-Te-Sb-endcycle [Sch01].

In the course of this work, one varies the mass excess in the endpart of the rp-process (A=80-105) in respect to its error bars, in order to investigate the influence of the mass on the stellar production process. The reaction rates are calculated with AME 2003 values and varied by two standard deviations (σ) of the mass values given by AME 2003 both to more positive ($+2\sigma$) and more negative (-2σ) mass excess values. The changes in light-curve, the final abundance and the production flux are investigated. These quantities are defined in section 6.1 in equation (6.6), (6.7) and (6.9) First, one wants to prove the agreement of all observables considered, i.e. the determination of the most important nuclei has to be independent from the regarded observable, e.g. ^{94}Ag has the greatest impact on the emitted light-curve of the x-ray burst, it also has the biggest impact on the final abundance of the burst. The figure 7.11 shows the calculated relative change in light-curve, final abundances, production path and finally the average of all observables for different nuclides.

One observes that all graphs are in good agreement to the average function. For a deeper understanding of the results, one needs to connect the dependence of the physical observables and the production path. The total impact of the mass uncertainty of the nuclei in the endpart of rp-process is shown in figure 7.12. The absolute value of the total impact is color-coded. The production path is shown schematically by the black lines. Remarkably, only a few nuclei show a large influence on the nucleosynthesis model. The highest value in the total influence is obtained for ^{94}Ag,^{93}Pd and ^{91}Rh. These nuclei are in the main path of the stellar process. A detailed discussion is given in the following section.

7.3.2 Detailed Discussion of the ^{93}Pd (p,γ) ^{94}Ag Reaction

The ^{93}Pd(p,γ)^{94}Ag reaction has the greatest impact on the light-curve of the simulation of the x-ray burst. Because of varying the masses of ^{93}Pd and ^{94}Ag one observes a shift of the burntime and a shift in the burn temperature (see figure 7.13). According to AME 2003 [Aud03] the Q-value for proton-capture reaction is (-890 ± 640) keV. Having a closer look at the final abundances of the rp-process, one can easily observe the impact of the variation of the Q-value (figure 7.14).

The abundances obtained for both calculations are almost identical up to A=93. At A=93 the production flow stops, due to a modified waiting point. The typical burst-time in these

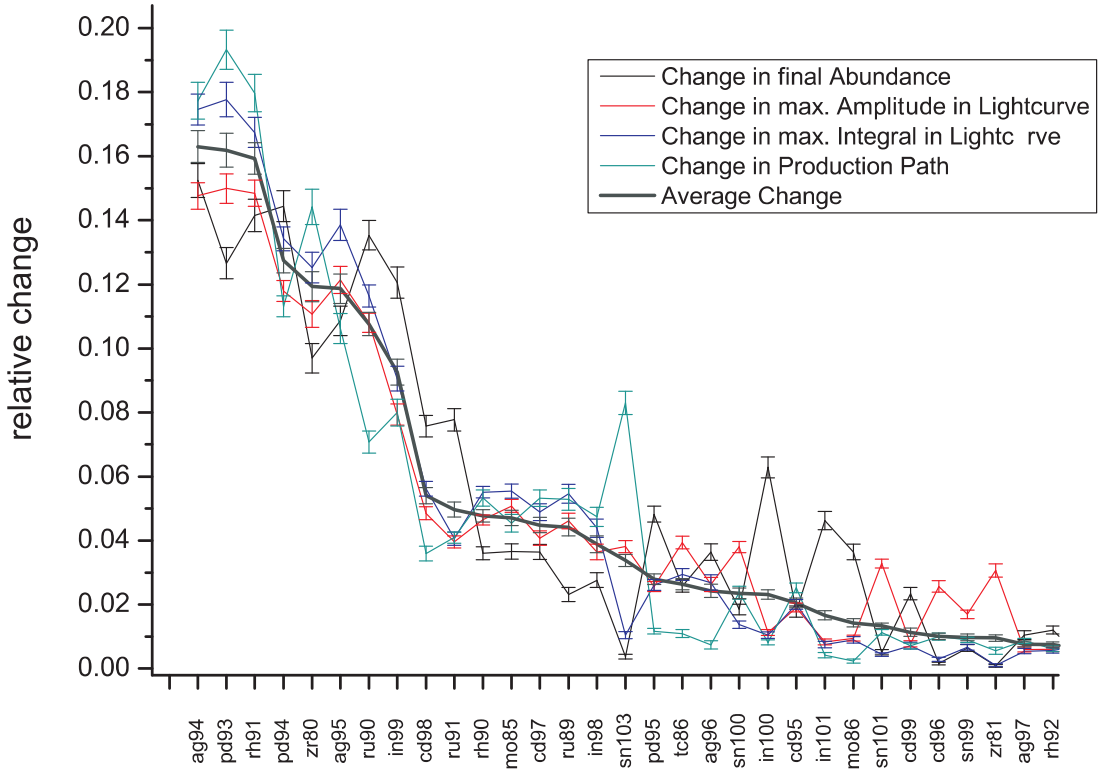

Figure 7.11: Overview on results of x-ray burst-simulations. This figure shows the different pseudo observables, which have been defined in chapter 5 in equation (6.6), (6.7), (6.8) and (6.9). The black line is the average of all curves. Settings: [XRB].

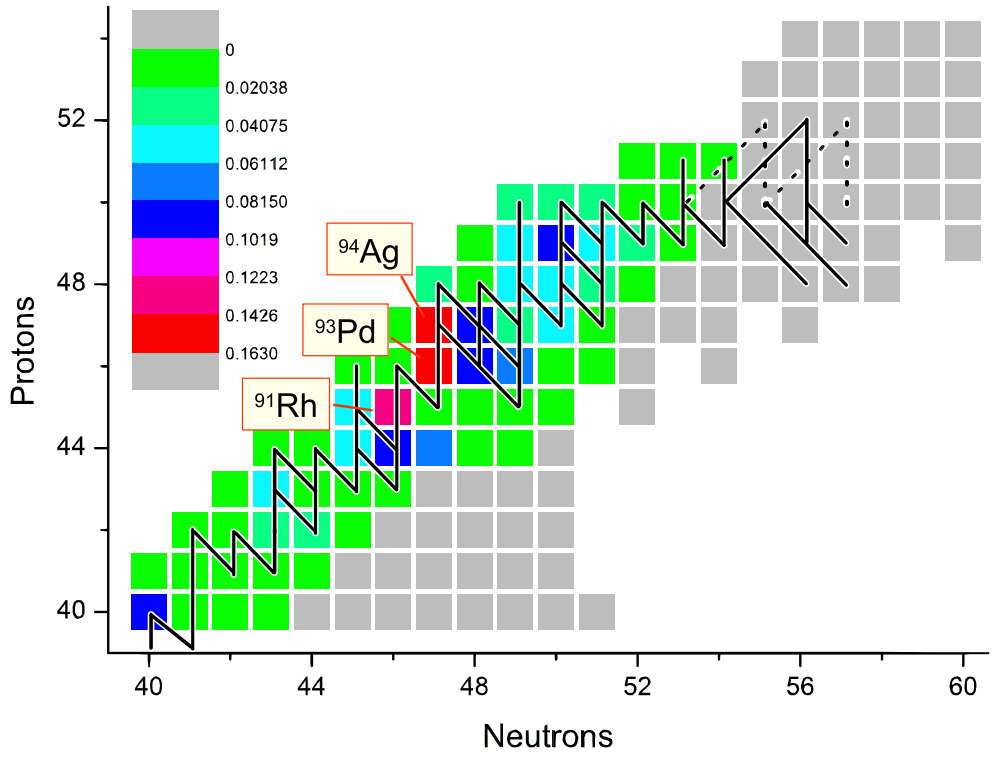

Figure 7.12: Overview on results of x-ray burst-simulations. Color-coded scale for the impact of mass variations on light-curve, final abundances (ashes) and path of the process. (Green means not important, Red stands for highest importance). The scale shows the relative impact, normalized to the mean value [XRB].

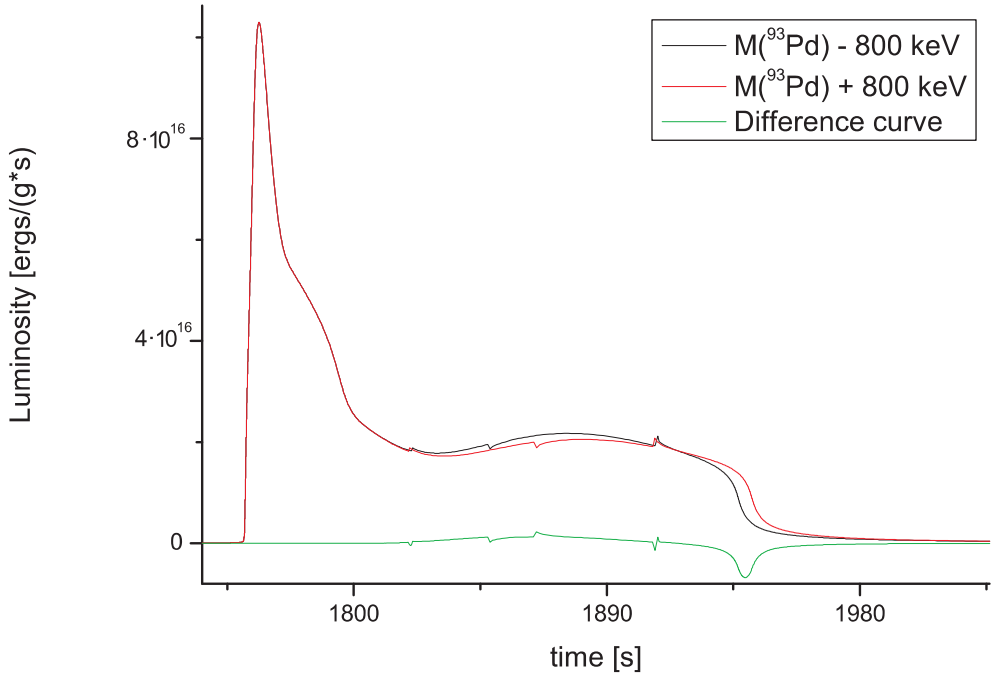

Figure 7.13: light-curve of Type II x-ray burst for two different mass excess values for ^{93}Pd. By reducing the Q-value of the ^{93}Pd(p,γ)^{94}Ag reaction, the beta decay branch is favoured, thus the burntime increases (red curve). The black curve is given by increasing the Q-value, which leads to a shorter, but more intensive burning. The green line is the difference of both curves [XRB].

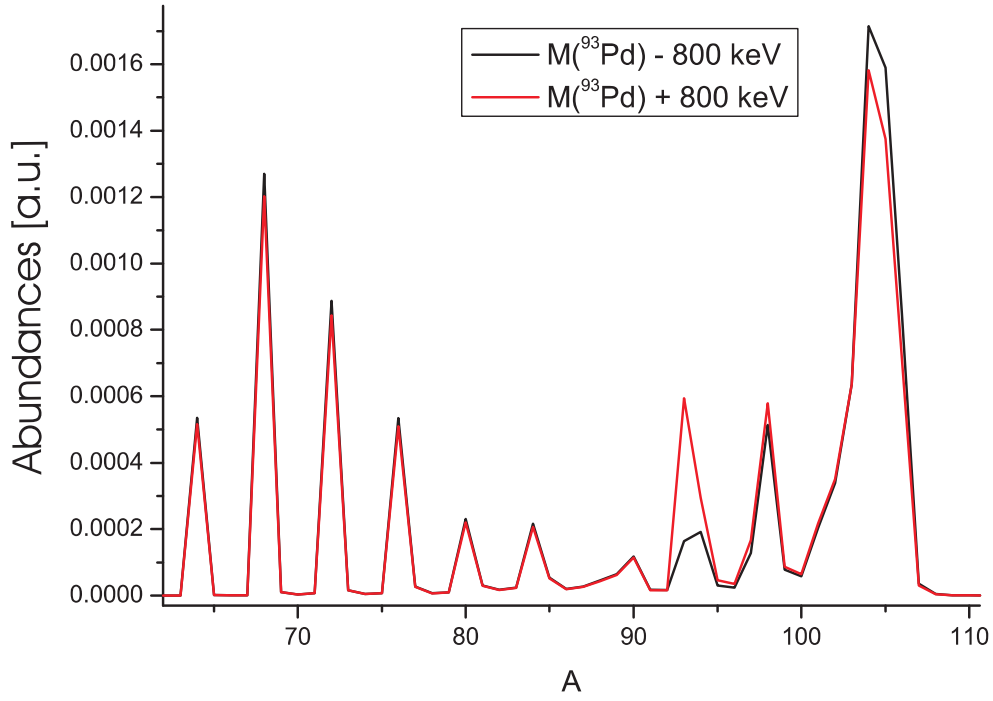

Figure 7.14: The final abundances for varied mass excess of ^{93}Pd. The black curve shows the abundance of the *rp*-process calculated with AME 2003 masses, but decreased ^{93}Pd mass by 800 keV. The red curve shows the abundances with increased mass excess of ^{93}Pd [XRB].

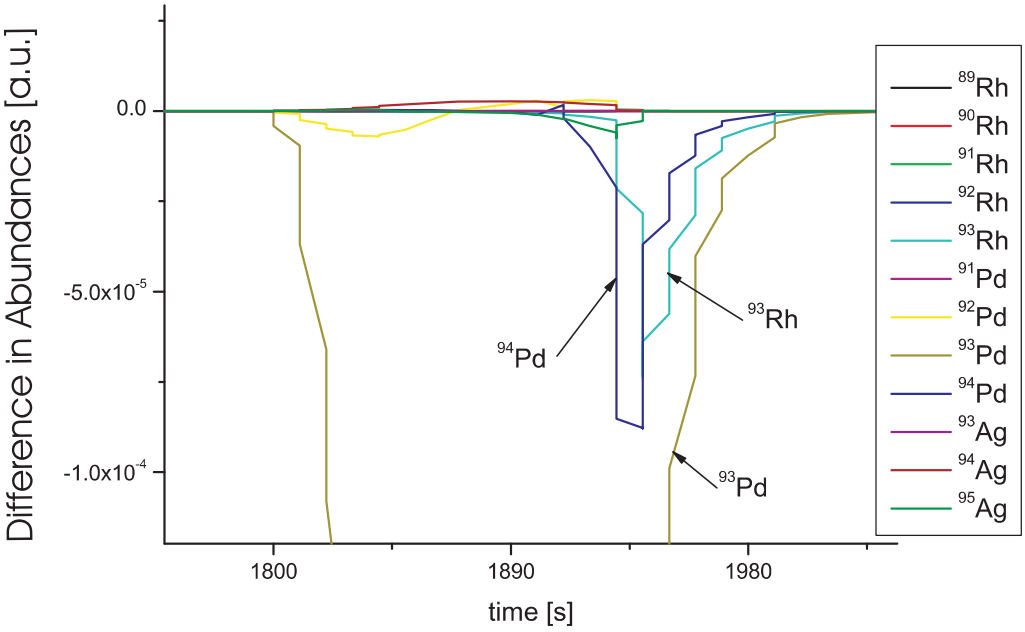

Figure 7.15: Time development of the abundances of nuclei in the vicinity of ^{93}Pd. The graph shows the differences between the abundances for artificially increased and decreased mass excess of ^{93}Pd by 800 keV [XRB].

simulations is about 200 seconds. The β-half-life of ^{93}Pd is 1 second. However, the half-life of ^{94}Ag is only 37 ms. If the Q-value is changed to a smaller value for proton-capture, the proton-capture reaction is favored, and at the same time the number of nuclei that have to wait for decaying into ^{93}Rh ($T_{1/2}$=13.9 s) are reduced. Thus some nuclei are able to skip this waiting point.

The time development of selected nuclei in the vicinity of ^{93}Pd is shown in figure 7.15. Only a few nuclei are affected by the mass variation of ^{93}Pd. The time development of ^{94}Pd is interesting for the understanding. The underproduction of ^{93}Pd should cause an observable overproduction of ^{94}Ag, due to the favouring of the proton-capture channel of ^{93}Pd. However, one observes a slight overproduction simultanously with the underproduction of ^{93}Pd. An overproduction of ^{94}Ag is not visible in figure 7.15, due to the short lifetime of ^{94}Ag (37ms). However, the short half-life causes the instant population of ^{94}Pd, therefore one would expect an overproduction of ^{94}Pd, as well. However, an underproduction is observed, which can be explained by the fact that the (p,γ)-reaction on ^{93}Rh, which also feeds 94Pd, is reduced even more strongly. One can compare the fluxes from ^{92}Rh into ^{93}Pd for different Q-values (figure 7.16). A change of $\pm 2\sigma$ of the mass excess of ^{93}Pd results in a flux-change of two orders of magnitude. In case of an increased Q-value, the almost the total flux goes from ^{93}Pd to ^{94}Ag. Thus, the beta-channel of ^{94}Ag is favored and nuclides with mass number 94 are produced. The large sensitivity of the flow-ratio between ^{93}Pd and ^{94}Ag indicates that the forward and backward flow are in the same order of magnitude. Thus this calculation shows ^{93}Pd as waiting point nuclide.

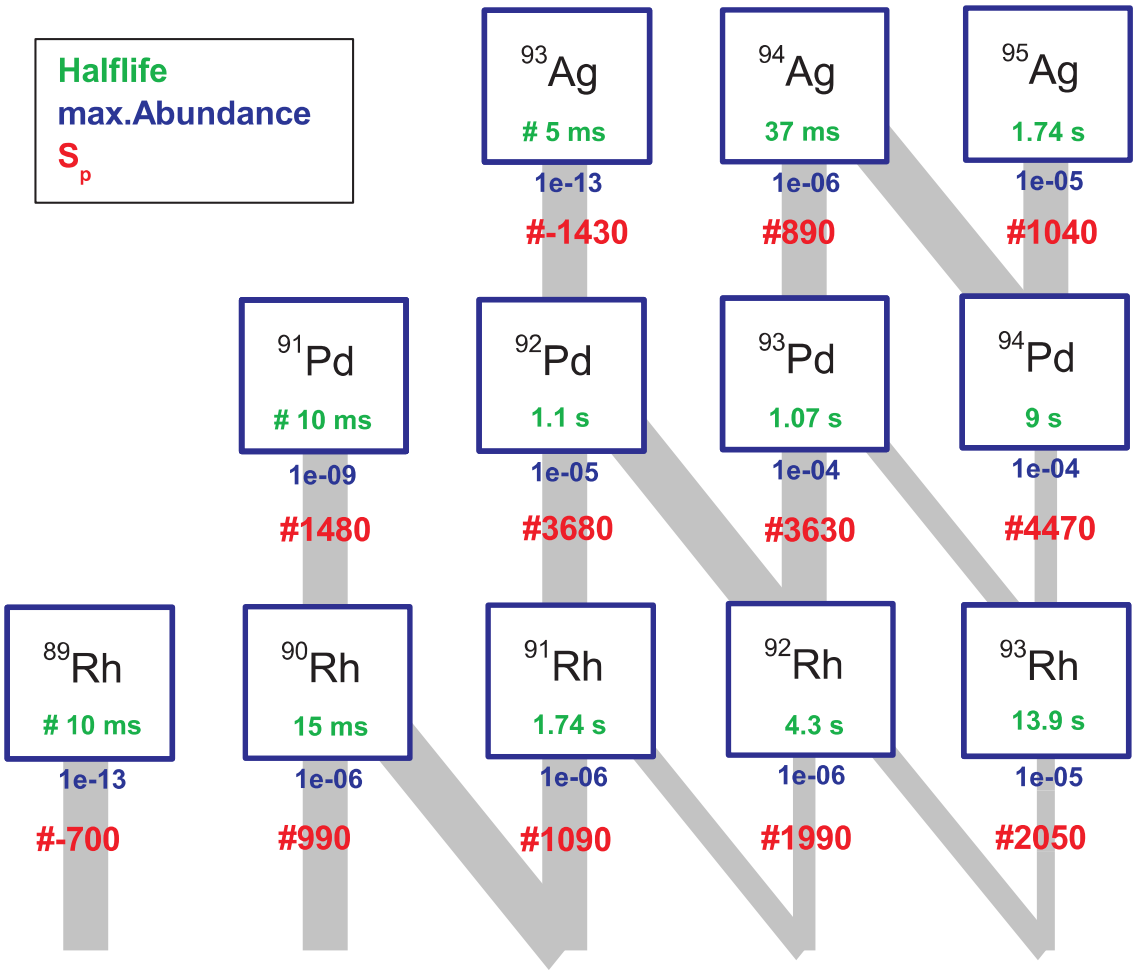

Figure 7.16: Illustration of proton separation energies (red values), halflives (green values) and the maximal abundance during the burst (blue values).

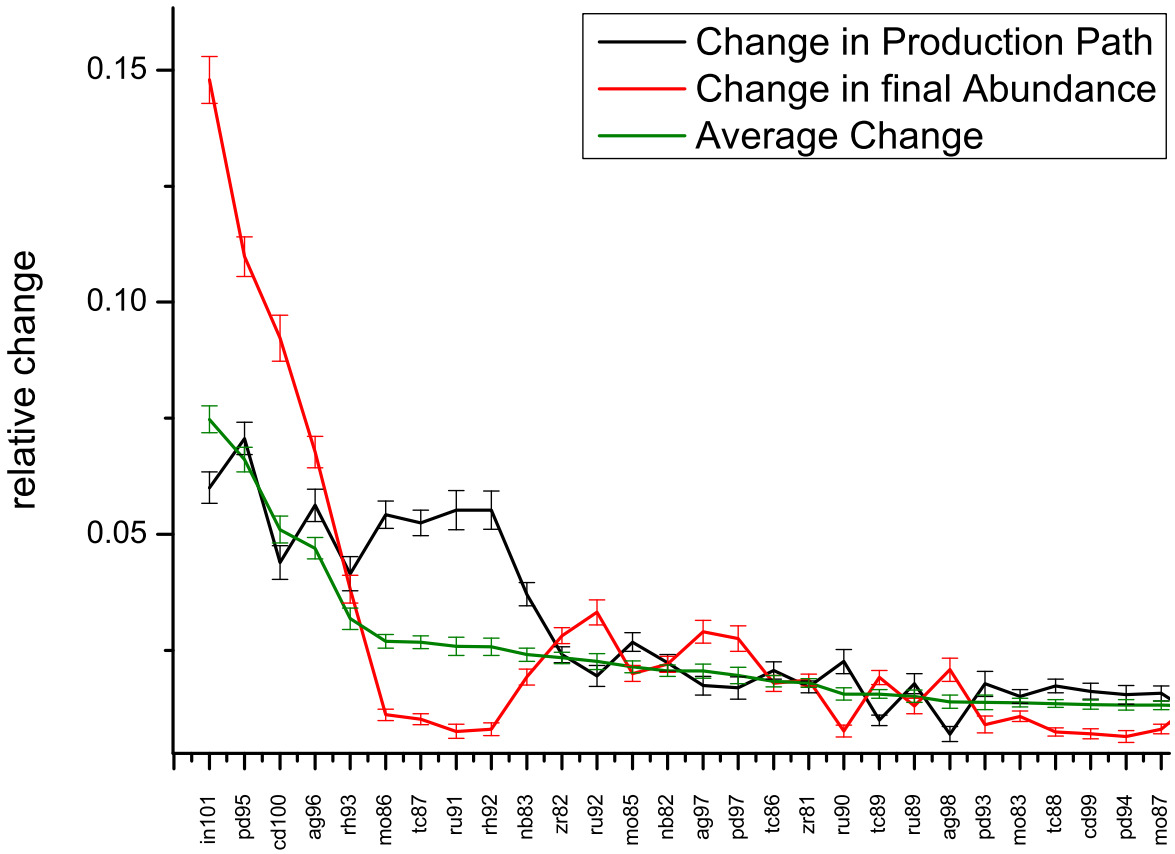

Figure 7.17: Overview on results of νp-simulations. This figure shows the different pseudo observables, which have been defined in 6.8 and 6.9. The green line is the average of all curves [NUP].

7.4 Variation of mass excess values: νp-Process

7.4.1 Overview on Results of νp-Process

The nucleosynthesis in neutrino-driven winds is more complicated than the rp-process, due to the additional reaction channels. Besides the proton reactions, one has to take neutron capture reaction in consideration as well. Especially the (n,p)-reaction, has the potential to modify the picture of classical waiting point nuclei. In this section, the mass variations are done, as explained in 7.3.1. The varied Q-values of the reactions in the network code result in recalculated backward reaction rates, which yield a shift in the equilibrium states (calculated with formula 3.21). Figure 7.17 presents the average impact of each isotope on the νp-process. The black function shows the impact of mass variation on the production path. The red line stands for the impact on the final abundances, calculated with equation (6.9), which represents the standard derivation of the average value of each nucleus. As in the discussion of the results of the rp-process, a color- coded overview is created on the total impact of the mass uncertainty on the νp-process (figure 7.18).

Only four nuclei show a larger importance for the model code, i.e. ^{100}Cd,^{101}In,^{95}Pd and ^{96}Ag. A discussion is given in the next subsection.

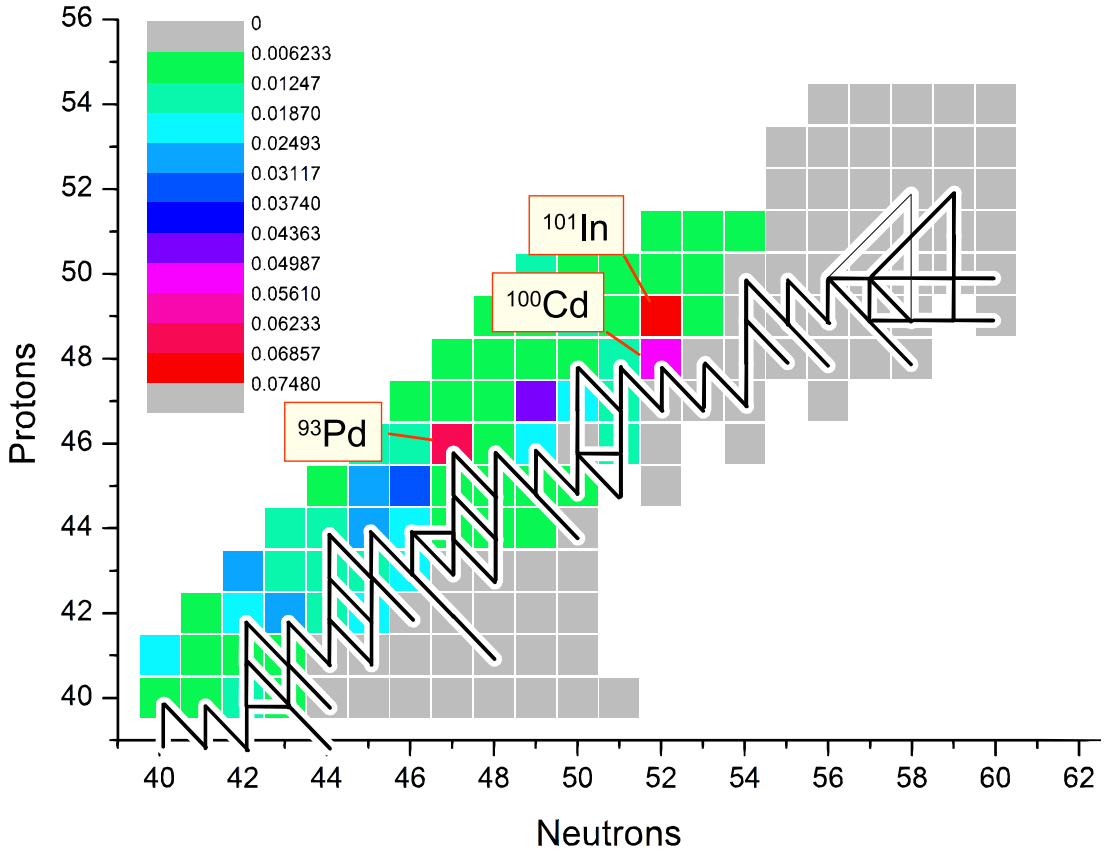

Figure 7.18: Color coded results of νp-process calculations. Color shows simulated relative impact on final abundances and path (Red more important, Green less important.) The black lines illustrates the production path of the νp-process [NUP].

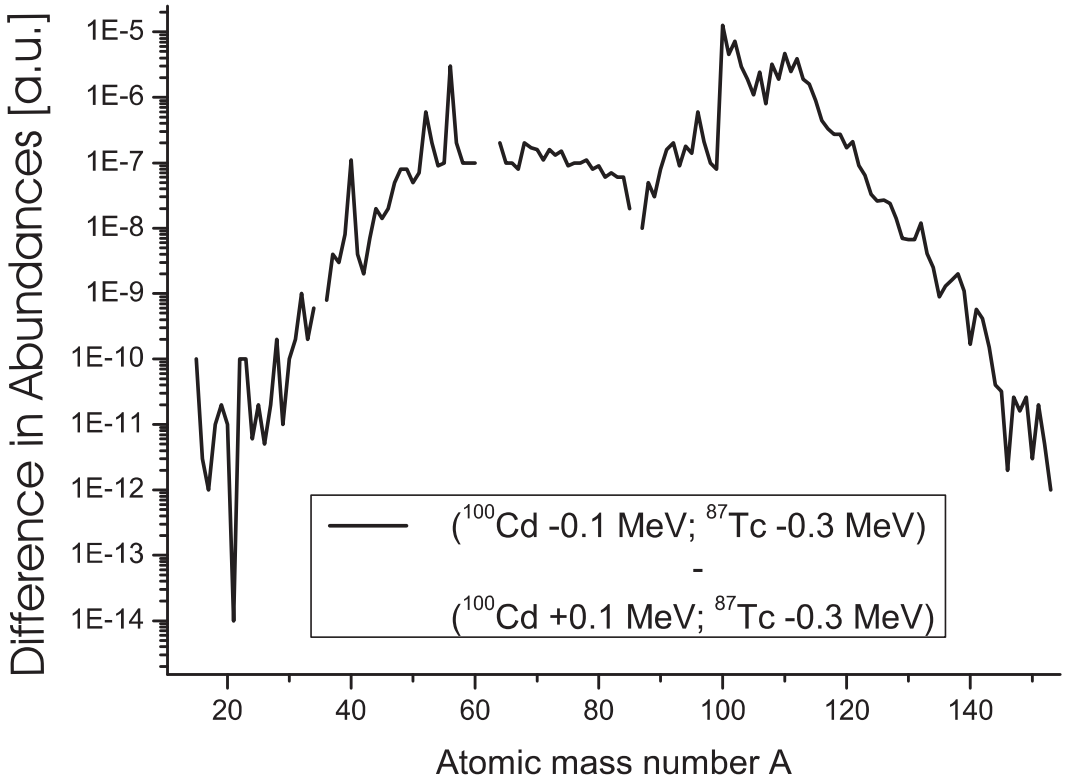

Figure 7.19: The variation of the final abundance for varied ^{100}Cd mass [NUP].

7.4.2 The Impact of the Mass Uncertainty of ^{100}Cd on νp-Process

Figure 7.18 shows the final impact of the mass excess of nuclides in the region on the νp-process. In order to understand these results, the impact of ^{100}Cd is discussed in detail. The importance of a single isotope on the stellar process depends on abundance of the seed nuclei, so the relative placement to the main production path of the νp-process is quite important. Secondly, the importance is derived from the instability of the nuclide's reaction-branching in relation to its error bar of the mass excess. In the scenario of the νp-process, one observes a branching between (p,γ),(n,γ),(n,p) and β-decay reactions, also between the various backward reactions. In this work the β-decay reactions are not affected by the Q-value variation, but the overall branching ratio shifts because of a stronger/weaker capture branch. First, one looks on the influence of the final abundance of all nuclei sorted by their mass numbers. The function in figure 7.19 shows the difference in the final abundances for two cases. The first abundance is calculated for an artificially decreased mass excess for ^{100}Cd, the second is the opposite, the mass excess is increased. The difference is shown in the figure. One can clearly see a peak at A=100. This peak reaches $2 \cdot 10^{-5}$, which should be compared to a typical final abundance of nuclei in its vicinity of about 10^{-4} to 10^{-6}. Therefore, this modification would be observable experimentally. An increased intensity in one mass channel means that the change of the mass excess reduces the branching into proton-capture reactions and favors β^+ and (n,p) reactions instead. The figure 7.20 shows the difference flux for two different values of the mass excess of ^{100}Cd. One observes a clear structure of larger and smaller fluxes in the region around ^{100}Cd. Due to the slightly varied simulation time, because

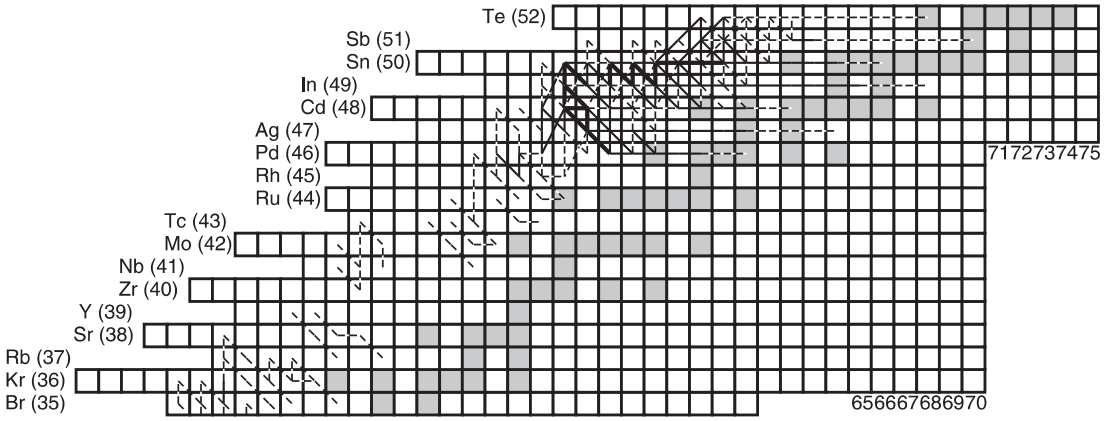

Figure 7.20: The difference flux for varied ^{100}Cd mass. The plot shows the difference of all reaction channels for the simulations with an increased and a decreased mass excess value of ^{100}Cd. The thick lines show a change in the production path of two orders of magnitude lower than the production flow of the triple α reaction. The thin line shows a production flow one order of magnitude lower than the thick lines. The dashed lines are one more magnitude lower than the thin lines [NUP].

Channel	$T_{1/2}$ of ^{100}Cd	Flow
$\beta^+ \rightarrow ^{100}$Ag	49.1s	$1.4{\cdot}10^{-4}$
$\beta^+ \rightarrow ^{100}$Ag	1.6 h	$1.4{\cdot}10^{-4}$

Table 2: β^+-flow observation for the measured and artificially increased half-life of ^{100}Cd.

of numerical artifacts. The simulation time is derived from the temperature development. If the temperature drops below 0.1 GK the network terminates. One notices small differences in β^+-decays of lighter nuclei. The next important step is the investigation of the β^+ / (n,p) reaction channel. In general, (n,p) reactions are much faster than β^+- reactions, however, the neutron capture reactions depend on the abundance of free neutrons in the proton-rich winds. The detailed discussion is given in the next subsection (7.4.2).

Variation of $T_{1/2}$ of ^{100}Cd

The availability of free neutrons in the νp-process, enables neutron-capture and (n,p)-reactions, which can compete with the β^+-decay. The dominant reaction cannot be determined from the output of the simulation program used in this work, because it delivers the integrated fluxes along the production path only. In order to identify the dominating reaction for the decay of heavy nuclei (A 80) in the νp-process and ^{100}Cd in particular, one can change the lifetimes and reaction rates and compare the resulting time-development of the abundances.

The β^+ lifetime of ^{100}Cd (49.1 s) has been increased to more than one hour. Since the total duration of the supernova explosion is 10 - 20 s, one can assume that during this time ^{100}Cd does not undergo any β^+-decay. One observes that, the production of ^{100}Ag is absolute the same for both lifetimes (see table 2). Hence, β^+-decay does not play an important role in the decay of ^{100}Cd.

Secondly, one disables the reaction $^{100}Cd(n,p)^{100}Ag$, but restores the half-life of ^{100}Cd used in this simulation to its literature value, in order to investigate the (n,p)-reaction. The flow is reduced by more than one order of magnitude (table 3), which means that this channel is governed by (n,p)-reactions. Thus, it is seen that the neutron-density is high enough to

Channel	Flow
$(n,p) - reaction \rightarrow {}^{100}\mathrm{Ag}$	$1.4{\cdot}10^{-5}$

Table 3: (n,p)-flow observation for an artificially increased (n,p)- reaction rate for ^{100}Cd.

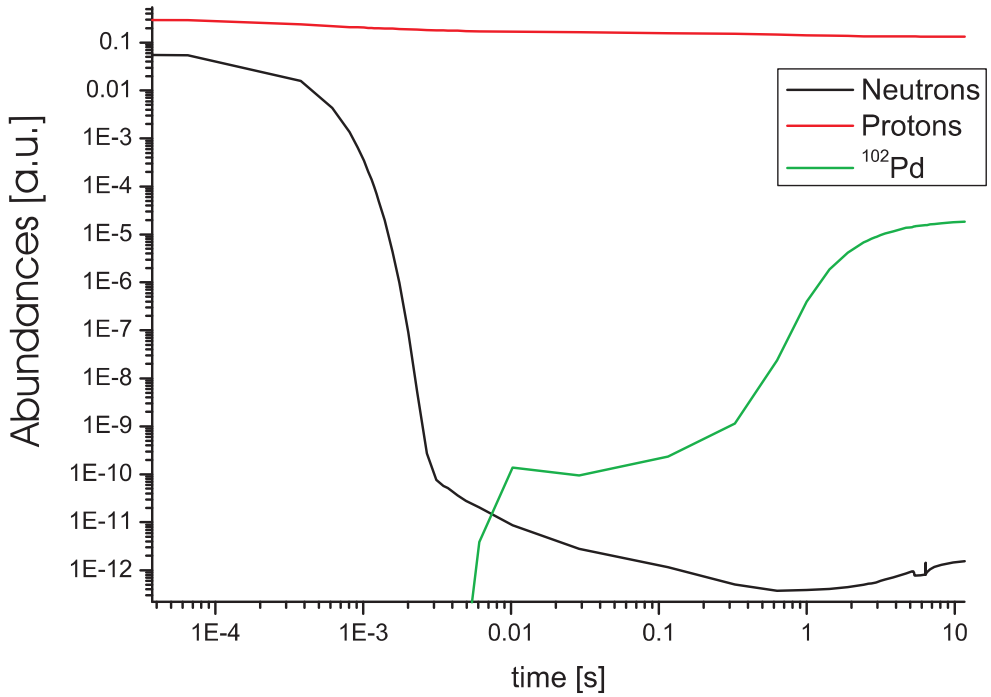

Figure 7.21: Typical abundance vs. time development in the νp-process. The red line shows the abundance of the free protons, the black line presents the abundance of the free neutrons in the νp-process. The green function shows the production of the stable isotope ^{102}Pd [NUP].

bridge classical waiting points with faster (n,p)-reactions.

For further investigations, one looks for the abundance vs. time development of ^{102}Pd. This nucleus is stable, but feels the strongest impact of a modified branching ratio in ^{100}Cd (This information comes from comparison of all readyint-files, which only reveals the integrated flow into each nucleus). In figure 7.21, the typical abundance vs time is shown for neutrons, protons and ^{102}Pd. The red line shows the proton-abundance, which is directly proportional to the electron-fraction Y_e. One observes a small consumption of hydrogen, which fits to the small change in Y_e. Typically, Y_e starts at 0.62 and decreases to 0.54. The black line indicates the extremely fast consumption of neutrons. The neutron abundance drops below $1 \cdot 10^{-10}$ after 2ms. The typical time, when heavier nuclei are produced, is in the range of seconds, thus only a small abundance of neutrons are available, but on the other side, the reaction flow in the A=90 mass region is dominated by (n,γ)- and (n,p)- reactions. Thus, one can conclude that after a neutron is produced by $p + \hat{\nu}_e - > n + e^+$, it is directly destroyed by a neutron capture reaction. The last curve shows the abundance of the stable nuclei ^{102}Pd. One sees that the abundance rises up to $1 \cdot 10^{-10}$ after 10 ms, afterwards the abundance increases up to $2 \cdot 10^{-5}$. The kink in the time development of ^{102}Pd could be caused by two different production mechanisms for the creation of ^{102}Pd. Because of the long β half-life of ^{102}Ag (12.9 min), one can exclude this reaction path, thus additional neutrons are needed for the production of this stable isotope. The first mechanism is the direct neutron

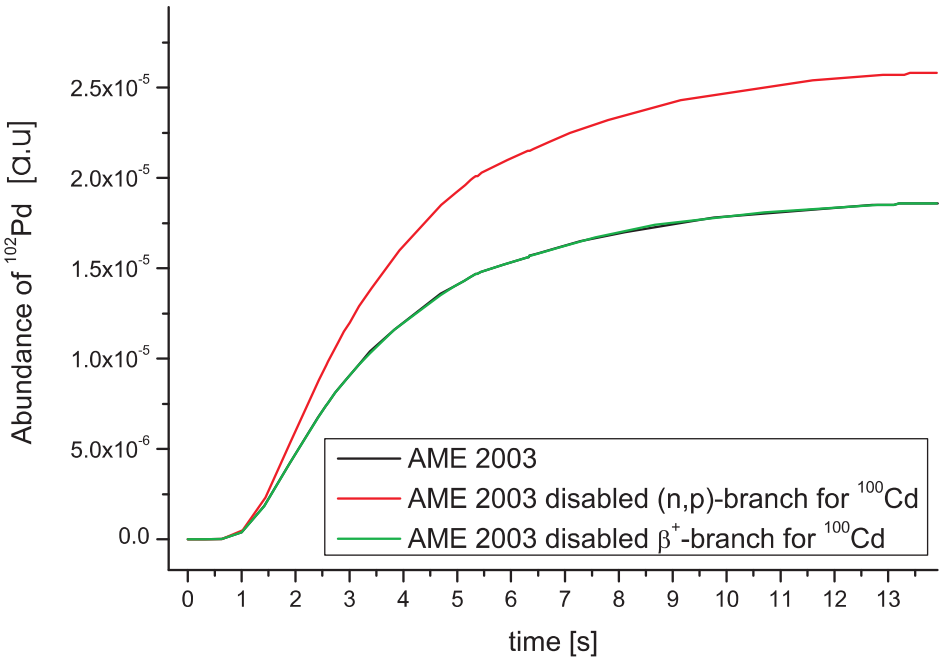

Figure 7.22: The abundance development of ^{102}Pd for three different cases, which are discussed in the text [NUP].

capture on ^{101}Pd. This is a rare reaction, because of the low proton binding energy in the neutron deficient mass region. The (n,p) reaction is more common, because of a much bigger Q-value difference, which stands for a larger gain in nuclear stability. The first increase of the abundance of ^{102}Pd is caused by the direct neutron capture reaction, because this reaction is able to produce ^{102}Pd in a shorter time. The (n,p) reaction of ^{102}Ag happens later, because ^{102}Ag has to be produced before.

In the beginning of this section, the influence of β^+- and (n,p) has been investigated. Figure 7.23 shows the differences in the production of ^{102}Pd for three cases. The first case (black line) is the original setting of the νp-process, without any altered reaction rates. The blue line, the second case, covers the first case in nearly every point, thus it offers no big changes to the original νp-process scenario. However, the red line, the last case, differs completely from the previous ones. One concludes that the β^+-reactions for ^{100}Cd are negligible, in regard to (n,p)- reactions. Therefore, the classical waiting point nuclei have to be identified, by investigating the branching ratios of p-capture, n-capture and (n,p)- reactions.

Investigation of the capture reactions branchings for ^{100}Cd

In the figures 7.23 and 7.24 one observes the time development of the differences in the abundances for two different cases. The first case is calculated with an increased ^{100}Cd mass, the second with a decreased mass. The mass variation of ^{100}Cd causes a decreased abundance of ^{100}Cd, due to the raised Q-value of the ^{100}Cd$(p,\gamma)^{101}$In- reaction. Therefore, the ^{101}In nuclei

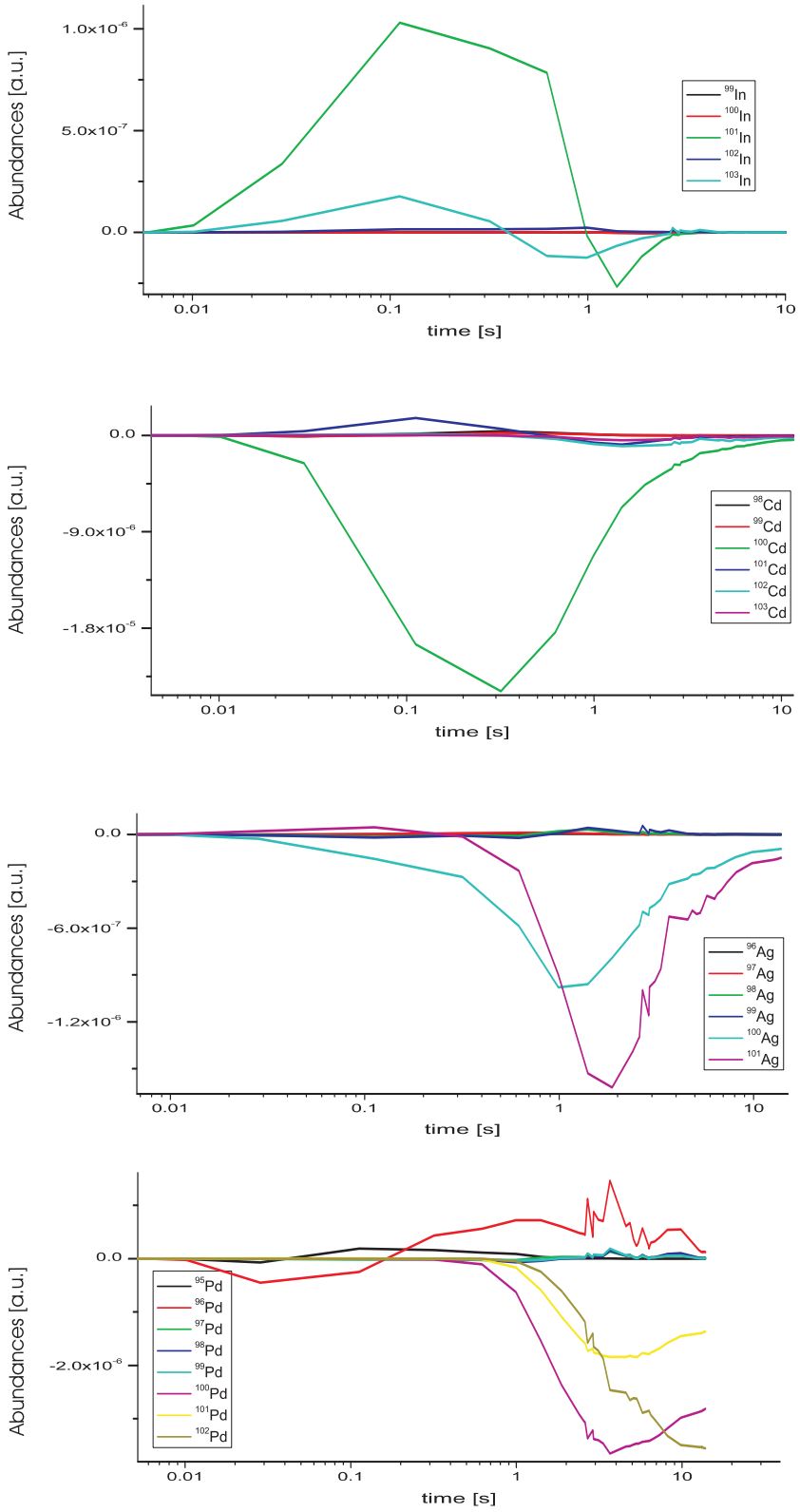

Figure 7.23: The abundance evolution in time of nuclei in the vicinity of ^{100}Cd. Every plot shows the difference in abundances for the different isotopes of an element. The difference is calculated with $Y_{M(^{100}Cd+200keV)}(t) - Y_{M(^{100}Cd-200keV)}(t)$ [NUP].

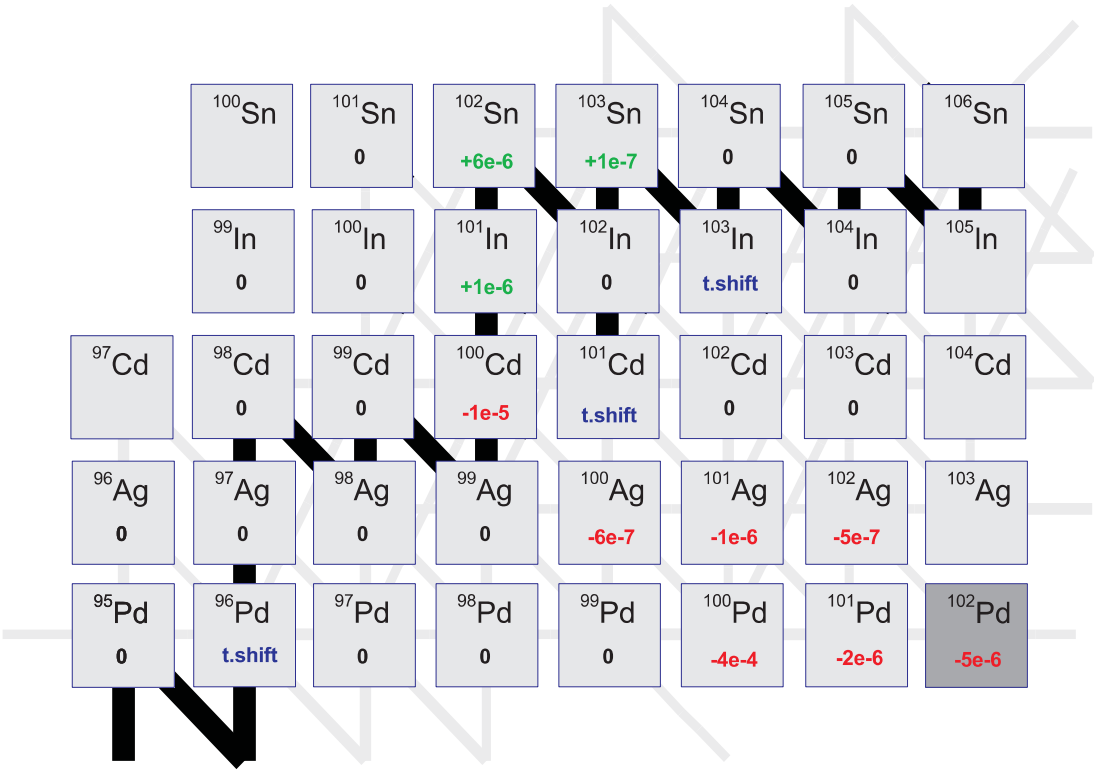

Figure 7.24: The schematic overview of the changes in abundance in the region around ^{100}Cd. The green/red numbers are calculated with $Y_{M(^{100}Cd+200keV)}(t) - Y_{M(^{100}Cd-200keV)}(t)$. 't.shift' stands for time shift in the $Y(t)$-function, which does not yield a change in the final abundances. The black and grey lines in the background shows the production flow, the grey flow through the grey lines is one order of magnitude smaller than through the black lines. ^{102}Pd is marked as stable isotope.

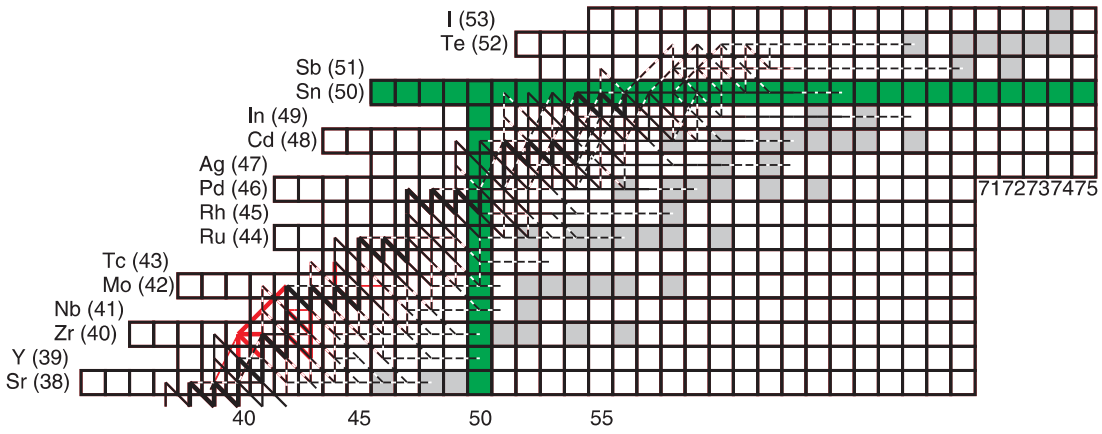

Figure 7.25: Impact of variation of ^{80}Zr on the production flow. The black flow is calculated with an increased mass excess for ^{80}Zr by 3 MeV. The red flow results from a decreased mass excess by 3 MeV. (The black flow covers the red flow. The only difference is shown in red. The red flow reaches as high as the black one.) The green squares mark the magic numbers in this region [NUP].

are more stongly populated. Additionally ^{102}Sn and ^{103}Sn. Due to the decreased population of ^{100}Cd, the nuclides in the (n,p)- reaction channel, ^{100}Ag and ^{100}Pd are underproduced. The underproduction of ^{101}Ag, ^{102}Ag, ^{101}Pd and ^{102}Pd are caused by the reduced number of seed nuclei for the (n,γ)- reactions on ^{100}Ag and ^{100}Pd. This can be observed in figure 7.20. The time shift of the abundance of ^{101}Cd gives a hint that the (n,p)- reactions of ^{101}In is faster than, the population of ^{101}Cd via $^{100}\mathrm{Cd}(n,p)^{100}\mathrm{Ag}(p,\gamma)^{101}\mathrm{Cd}$.

7.4.3 The Impact of the Mass Uncertainty of ^{80}Zr

By varying the mass excess value of ^{80}Zr by 2σ, one observes a huge impact on the production flow of the νp- process compared to other nuclei of higher importance of the νp-process. A mass variation of ^{80}Zr by 3 MeV is unphysical, but is a result of the systematic variation technique used in this work. But, to figure out the importance of ^{80}Zr for nuclear astrophysics, you have to consider also the size of the error. In our case the size of this error bar is gigantic (1480 keV). which is not extrapolated, but measured. Having a look at the Q-value for the proton capture for ^{80}Zr:

$$Q(Proton - capture) = (711 \pm 2100)keV$$

The huge impact on the production path (figure 7.25) is significant in the vicinity of ^{80}Zr. The proton- and neutron-capture rate are strongly influenced, even so the alpha-capture rate, therefore a new cycle is established.

7.5 The νp-process for different stellar conditions

The figure 7.26 in this section is a color coded overview on the impact on νp-process, but the stellar scenario is different from the one in chapter 6.1. One notices the different production path to figure 7.18. The parameter of this stellar scene is taken from numerical simulations of a supernovae explosions. The temperature, entropy and density development of the calculated supernova explosion is taken as input data for the nucleosynthesis network[Wind]. This shows

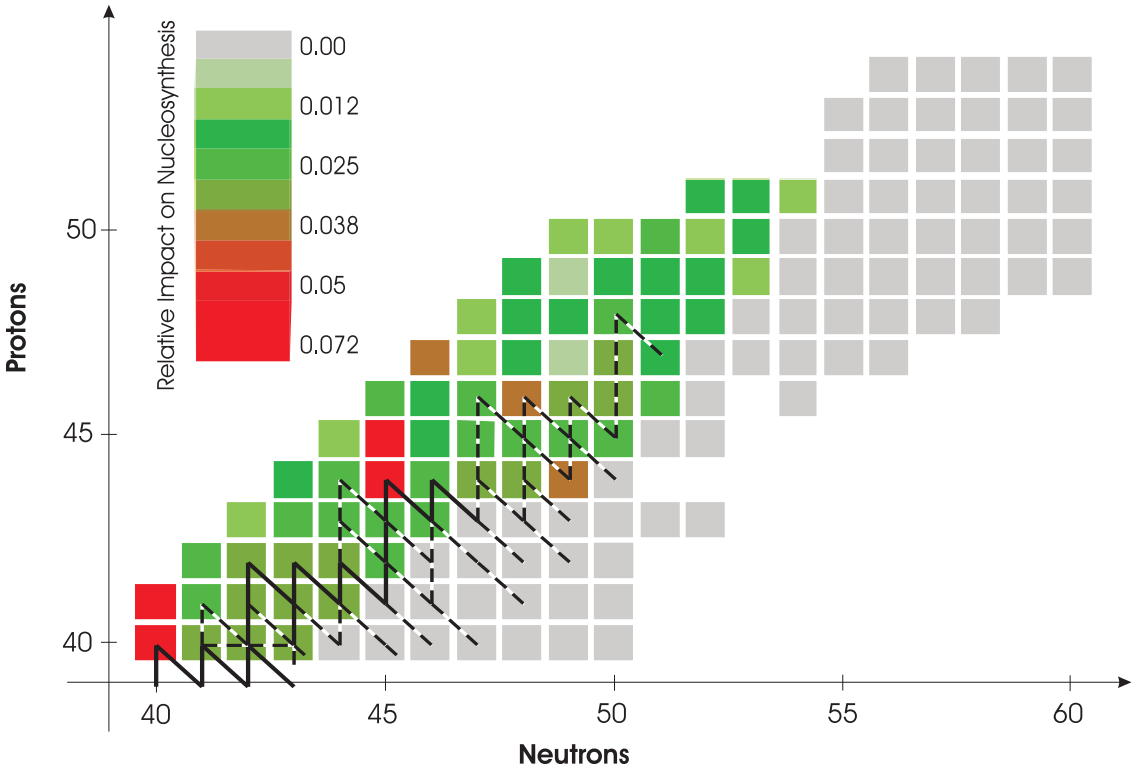

Figure 7.26: Color-coded results of νp-process calculations. Bottom color shows simulated impact on final abundances and path (Red more important, Green less important.). Top color shows measurement facility(Red stands for extrapolation. Black is a stable isotope) [Wind].

the dynamic of the νp-process. The explosion and synthesis time is nearly the same as in the former settings for the νp-process. The most important isotopes in this stellar scenario are ^{80}Zr,^{81}Nb,^{89}Ru and ^{90}Rh.

Chapter 8

Conclusions and Outlook

In this work, we have investigated the impact of mass uncertainties on the *rp*- and νp-process models. We have performed variations of the mass values in network codes. In general, we have found out that only a few nuclei have severe influence on the abundances, light-curves and production flow in the *rp*- and νp-process.

In the *rp*-process, we have shown the importance of the ^{93}Pd, ^{94}Ag, ^{91}Rh and ^{94}Pd nuclides. We have identified ^{93}Pd as waiting point nuclide. Due to the big differences in lifetimes the production flow strongly depends on the ratio of (p,γ)-(γ,p)- reactions.

We have discussed the production mechanism of the νp-process. This path covers less exotic nuclei than in the *rp*- process, because of the implementation of neutron- capture reactions. Moreover, we have shown the importance of ^{100}Cd, ^{101}In and ^{93}Pd for the abundances and production path. We have presented a new description of waiting point nuclei in the νp-process, which are governed by the branching ratio between (p,γ)- and (n,p)- reactions. Additionally, we have investigated the impact of the mass uncertainty of ^{80}Zr on the νp-process. We have shown clearly that the present error bar of 1.5 MeV is too large to determine the physical importance of this nuclide on this nucleosynthesis process.

Nuclides, which are close to the N=50 shell closure are characterized by small production cross sections and therefore difficult to access in present experiments. Therefore, reaction network codes have to rely on theoretical mass predictions and mass extrapolations. We have included new mass measurements since 2003 and have presented the systematic trend for the newly measured masses to higher mass excess values. This systematic trend, which differs from the AME 2003 predictions, points out the importance of accurately measured mass measurements. Furthermore, we have presented new local linear extrapolations in the A=80-105 mass region. By extrapolating newly measured masses with AME 2003 masses we have tested our extrapolation method. The network calculations with the newly measured and extrapolated masses underline the strong dependence of the *rp*-process on masses, especially of the exact position of the proton dripline and the proton separation energies of exotic nuclei. Moreover, we have observed that the νp-process is much less dependent on the accuracy of nuclear masses far-off stability than the *rp*- process.

In future, we want to improve the implementation of new mass values into the network code. Therefore, we want to include the calculation of the forward reaction rate with statistical model calculations (NON-SMOKER), additionally, we want to include stellar resonant capture rates. New accurate mass measurements of *rp* nuclides are planned with SHIPTRAP and FRS-ESR facilities at GSI using projectile fragmentation and fusion reactions.

Bibliography

[Ame93] Audi et al.; *'The 1993 Atomic Mass Evaluation'*; **http://amdc.in2p3.fr/masstables/Ame1993/ame93.pdf**; [1996]

[Amt06] Amthor et al.; *'Sensitivity of Type I X-Ray Bursts to rp-Process Reaction Rates'*; **arXiv:astro-ph/0608451 v1**; [2006]

[Arc07] Arcones et al.; *'Nucleosynthesis-relevant conditions in neutrino-driven dupernova outflows'*; **Astronomy & Astrophysics manuscript 6983**; [2007]

[Ath07] http://athena-positrons.web.cern.ch/ATHENA-positrons/wwwathena/penning.html; [2005]

[Atk36] Atkinson; **Astro. J. 84, 73**; [1936]

[Aud95] Audi et al.; *'Selecting nuclides for mass measurements'*; **Physica Skripta T59, 411**; [1995]

[Aud00] Audi et al.; *'The Evaluation of Atomic Masses'*; **Hyperfine Interactions 0 1-10**; [2000]

[Aud03] Audi et al.; *'The 2003 Atomic Mass Evaluation'*; **Nucl. Phys. A 729**; [2003]

[Aug94] Auger et al.; *'A cyclotron as a high resolution mass spectrometer for fast secondary ions'*; **Nucl. Instrum. Methods A 350, 235-243**; [1994]

[Bal05] Balantekin et al.; *'Neutrino mixing and nucleosynthesis in core-collapse supernovae'*; **New Journal of Physics 7, 51**; [2005]

[Bah69] Bahcall et al.; *'The rate of the proton-proton reaction and some related reactions'*; **Astro. J. 155**; [1969]

[Ber94] Bernas et al.; *'Projectile fission at relativistic velocities...'*; **Phys. Let. B 331, 1924**; [1994]

[Bet38] Bethe, H.A.,Critchfield,C.L.; **Phys. Rev. 54, 248**; [1938]

[Bet39] Bethe, H. A.; **Phys. Rev. 55, 434)**; [1939]

[Blo05] Block et al.; *'The ion-trap facility SHIPTRAP - Status and perspectives'*; **Eur. Phys. J., A25, 49**; [2005]

[Bol92] Bollen et al.; *'Resolution of nuclear ground and isomeric states by a Penning trap mass spectrometer'*; **Phys. Rev. C46, R2140**; [1992]

[Bor93] Borcea et al.; *'New Methods for Extrapolating Masses Far from Stability'*; **Institure of Phy. conference series (132) 59**; [1993]

[Bia89] Bianchi et al.; *'SPEG: An Energy Loss Spectrometer for Ganil'*; **Nucl. Instrum. Methods A276, 509-520**; [1989]

[Bor92] Borcea et al.; *'New Methods for Extrapolating Masses Far from Stability'*; **CSNSM 92.38**; [1992]

[Bor95] Borcea et al.; *'Constrained Mass Extrapolations'*; **http://csnwww.in2p3.fr**; [1995]

[Bur57] Burbidge et al.; *'Synthesis of the Elements in Stars'*; **Rev. Mod. Phys. 29, 4**; [1957]

[Cum01] Cumming et al.; *'Carbon Flashes in the Heavy Element Ocean on accreting Neutron Stars'*; **Astro.J. 559 (2) L 127**; [2001]

[Cum06] Cumming et al.; *'Long Type I X-Ray Bursts and Neutron Star interior Physics'*; **Astro. J. 646 (1), 429**; [2006]

[Dic06] Dickel; *'Aufbau und Charakterisierung eines Multi-Reflektions-Flugzeit-Massenspektrometers zur Isobarentrennung'*; **Diploma thesis**; [2006]

[FGM87] Franske, Geissel, Muenzenberg; *'Experiment proposal for the SIS- FRS-ESR facilities'*; **unpublished**; [1987]

[FGM07] Franske, Geissel, Muenzenberg; *'Mass and Lifetime Measurements of Exotic Nuclei in Storage Rings'*; **unpublished**; [2007]

[Fis04] Fisker et al.; *'Extracting the rp-process from X-ray burst light curves'*; **arXiv:astro-ph/0407319 v1**; [2004]

[Fis04b] Fisker et al.; *'The reactions and ashes of thermonuclear explosions on neutron stars'*; **arXiv:astro-ph/0408088v2**; [2004]

[Fis07] Fisker et al.; *'Explosive hydrogen burning during type I X-ray bursts'*; **arXiv:astro-ph/0703311 v1**; [2007]

[Fra87] Franzke et al.; *'The Heavy Ion Storage And Cooler Ring Project ESR At GSI'*; **Nucl. Instrum. Methods B24/25 18-25**; [1987]

[Fre06] Frebel et al.; *'Chemical Abundance Analysis of the Extremely Metal-Poor Star HE 1300+0157'*; **arXiv:astro-ph/0612160**; [2006]

[Fro05] Fröhlich et al.; *'Nucleosynthesis in Neutrino-Driven Supernovae'*; **arXiv:astro-ph/0511584v1**; [2005]

[Fro06] Fröhlich et al.; *'Neutrino-Induced Nucleosynthesis of $A > 64$ Nuclei: The νp Process'*; **Phys.Rev.Let.96 (14)**; [2006]

[Gal03] Galloway et al.; *'Periodic thermonuclear x.ray bursts from GS 1826-24 and the fuel composition as a function of accretion rate'*; **Astro.J. 601 (1) 466**; [2003]

[Gei92] Geissel et al.; *'The GSI projectile fragment separator (FRS): a versatile magnetic system for relativistic heavy ions'*; **Nucl. Instr. and Meth. B70**; [1992]

[Gei95] Geissel et al.; *'Secondary Exotic Nuclear Beams'*; **Ann. Rev. Nucl. Part. Sci. 45, 163**; [1995]

[Gei01] Geissel et al.; *'Mass measurements of stored exotic nuclei'*; **NUCLEAR PHYSICS A 693 (1-2)**; [2001]

[Gor96] Goriely et al.; *'Waiting point approximation and canonical multi-event r-process revisited'*; **Astron.Astrophys. 312, 327**; [1996]

[GSI07] www.gsi.de

[Gue07] Guenaut et al.; *'High-precision mass measurements of nickel, copper, and gallium isotopes and the purported shell closure at N=40'*; **Phys. Rev. C 75, 044303**; [2007]

[Har56] *'Detection of the Free Neutrino: a Confirmation'***Science**; [1956]

[Hau88] *'An overview of the 1986-1987 Atomic Mass Predictions'*; **Atomic Data and Nucl Data Tables 39, 185**; [1988]

[Hax97] Haxton et al.; *'Neutrino-Induced Nucleosynthesis and the Site of the r Process'*; **Phys. Rev. Let 78, 14**; [1997]

[Her95] Herndl et al.; *'Proton capture reaction rates in the rp process'*; **Phys. Rev. C 52, 1078-1094**; [1995]

[Hix03] Hix et al.; *'Impact of nuclear reaction rate uncertainties on Nova models'*; **Nucl. Phys. A 718, 620**; [2003]

[Hof78] Hoffman et al.; **Nature 271, 630**; [1978]

[Hoy56] Hoyle et al.; *'Origin of the Elements in Stars'*; **Science, 124, 3223**; [1956]

[Ili07] Iliadis; *'Nuclear Physics of Stars'*; **Wiley-VCH**; [2007]

[Jae88] Jänecke et al.; *'Mass prediction from the garvey-kelson mass relations'*; **At Data Nucl Data Tables 39, 265-271**; [1988]

[Jan07] Janka et al.; *'Theory of core-collapse supernovae'*; **Phys. Reports Rev. Section of Phys. Let.. 442 (1-6) 38**; [2007]

[Jon05] Jones; *'End-point of the rp-process and periodic gravitational wave emission'*; **Phys. Rev. D 72 (8)**; [2005]

[Jor04] Jordan IV et al.; *'Nucleosynthesis in Fast Expansions of High-Entropy, Proton Rich Matter'*; **Astro.J. 617 (2) L131**; [2004]

[Kel02] Kellerbauer et al.; *'A study of the accuracy of the Penning trap mass spectrometer ISOLTRAP and Standard-Model tests with superallowed beta decays'*; **URL: http://www.ub.uni-heidelberg.de/archiv/2463/**; [2002]

[Kel03] Kellerbauer et al.; *'From direct to absolute mass measurements: A study of the accuracy of ISOLTRAP'*; **Eur.Phys.J.D 22, 53**;[2003]

[Kis07] Kishimoto et al.; *'Neutrino-Accelerated Hot Hydrogen Burning'*; **Astro.J.656 (2) 1104**; [2007]

[Lit07] Litvinov et al.; *'Direct mass measurements of neutron-deficient ^{152}Sm projectile fragments at the FRS-ESR facility'*; **DOI 10.1007/s10751-007-9542-3**; [2007]

[Lun01] Lunney et al.; *'Precision mass measurements of very short-lived, neutron-rich Na isotopes using a radio-frequency spectrometer'*; **Phys. Rev. C 64, 054311**; [2001]

[Lun03] Lunney et al.; *'Recent trends in the determination of nuclear masses'*; **Reviews of modern physics, 75**; [2003]

[Mad99] Madsen et al.; *'Efficient excitation of Ps by 50-100 fs laser pulses'*; **JOURNAL OF PHYSICS B-ATOMIC MOLECULAR AND OPTICAL PHYSICS 32 (15): L425-L431**; [1999]

[Mat07] Matos et al.; *'TOF-Brho Mass Measurements of Very Exotic Nuclides for Astrophysical Calculations at the NSCL'*; **arXiv:0707.0119**; [2007]

[Maz07] Mazzocchi et al.; *'α Decay of ^{109}I and Its Implications for the Proton Decay of ^{105}Sb and the Astrophysical Rapid Proton-Capture Process'*; **Phys. Rev. Let 98**; [2007]

[Mey02] Meyer; *'r-Process Nucleosynthesis without Excess Neutrons'*; **Phys. Rev. Let 89, 23**; [2002]

[Mon07] Montes; *private conversation*; [2007]

[Mue79] Muenzenberg et al.; *'The Velocity Filter SHIP, a Separator of Unslowed Heavy Ion Fusion Products'*; **Nucl. Inst. Meth. 161, 65-82**; [1979]

[Nas07] $http://www.nasa.gov/centers/goddard/images/content/96701main_BINARY_lg_web.jpg$

[Nas07b] $http://hubblesite.org/gallery/album/entire_collection/pr2005037a/$

[Nuc03] Audi et al.; *'Nucleus-win'*; **http://csnwww.in2p3.fr/AMDC/nucleus/nucWxp2.exe**; [2003]

[NUP] Illustration is calculated with 'νp-process in early protonrich ejecta'- network code provided by Martinez-Pinedo et al.. Initial values are set to: Y_e =0.62, $\rho_1 = 1E7\frac{g}{cm^3}$, $\tau = 1E-3$, $\rho_2 = 75E3\frac{g}{cm^3}$, $\delta = 1$, $s/k_B = 30$

[Obe98] Oberhummer et al.; *'Proceedings of Nuclei in the Cosmos'*, **Z. Physik A349, 241**, [1998]

[Obe99] Oberhummer et al.; *'The triple-alpha process and its antropic significance'*; **arXiv:nucl-th/9810057v2**; [1999]

[Pac83] Paczynski; **Astro. J. 267, 315**; [1983]

[Per06] Pereira et al.; *'R-process Experimental Campaign at the National Superconducting Cyclotron Laboratory'*; **arXiv.org/abs/astro-ph/0608582**; [2006]

[Pla07] Plass et al.; **ASMS Conference on Mass Spectrometry and Allied Topics**; [2007]

[Pin06] Martinez-Pinedo et al.; *'Nucleosynthesis in neutrino heated matter: The νp-process and the r-process'*; **arXiv:astro-ph/0608490 v1**; [2006]

[Pin07] Martinez-Pinedo; *'Private communications'*; [2007]

[Pru05] Pruet et al.; *'Nucleosynthesis in the Hot Convective Bubble in Core-Collapse Supernovae'*; **Astro. J. 623 (1) 325**; [2005]

[Pru06] Pruet et al.; *'Nucleosynthesis in Early Supernova Winds II: The Role of Neutrinos'*; **Astro. J. 644 (2) 1028**; [2006]

[Qia96] Qian et al.; *'Nucleosynthesis in Neutrino-Driven Winds: I.The Physical Conditions'*; **Astro. J. 471 (1) 331**; [1996]

[Rav94] Ravn et al.; *'Comparison of radioactive ion-beam intensities produced by means of thick targets bombarded with neutrons, protons and heavy ions'*; **Nucl. Instr. and Meth. B88, 441**; [1994]

[Rah07] Rahaman et al.; *'Precision mass measurements of radioactive nuclei at JYFLTRAP'*; **arXiv:nucl-ex/0703018 v1**; [2007]

[Rai97] raimann et al.; *'The rp-process and new measurements of β-delayed proton decay of light Ag and Cd isotopes'*; **Nucl. Phys. A 621 (1-2) L215**; [1997]

[Rap05] Rapp et al.; *'The Influence of Reaction Rates on the Final p-Abundances'*; **Nucl. Phys. A 758, 545C**; [2005]

[Rap06] Rapp et al.; *'Sensitivity of p process nucleosynthesis to nuclear reaction rates in a 25 solar mass supernova model'*; **Astro.J. 653 (1) 474**; [2006]

[Rau00] Rauscher et al.; *'Astrophysical reaction rates from statistical model calculations'*; **At Data Nucl Data Tables 75, 1-351**; [2000]

[Rau01] Rauscher et al.; *'Tables of nuclear cross sections and reaction rates: ...'*; **At Data Nucl Data Tables 79, 47-64**; [2001]

[Rau06] Rauth et al.; *'Direct mass measurements around A=146 at SHIPTRAP'*; **private communications**, [2006]

[Rem97] Rembges et al.; *'An approximation for the rp-Process'*; **Astro. J. 484:412-423**; [1997]

[Rin04] Ringle et al.; *'The LEBIT 9.4 T Penning trap system'*; **Eur. Phys. J. A 25, 59-60**; [2005]

[Rin06] Ringle et al.; *'Precision mass measurements with LEBIT at MSU'*; **International Journal of Mass Spectrometry 251, 300**; [2006]

[Roh94] Rohlf et al.; *'Physics from a to Z0'*; **Wiley**; [1994]

[Ryk95] Rykaczewski et al.; *'Identification of new nuclei at and beyond the proton drip line near the doubly magic nucleus* ^{100}Sn*'*; **Phys. Rev. C 52,5**; [1995]

[Sav79] Savonije et al.; *'Roche-lobe overflow and massive X-ray binary systems'*; **Astron. Astrophys. 71, 352-358**; [1978]

[Sch98a] Schatz; *'Wasserstoffbrennen unter extremen Temperatur- und Dichtebedingungen'*; **PhD-thesis, Forschungszentrum Karlsruhe**; [1998]

[Sch98] Schatz et al.; *'rp-process nucleosynthesis at extreme temperature and density conditions'*; **Physics Reports 294, 167-263**; [1998]

[Sch99] Schatz et al.; *'The Rapid Proton Process Ashes From Stable Nuclear Burning On An Accreting Neutron Star'*; **Astro. J., 524 : 1014-1029**; [1999]

[Sch99b] Schatz et al.; *'The rp-process ashes from stable nuclear burning on an accreting neutron star'*; **Astro.J. 524 (2) 1014**; [1999]

[Sch01] Schatz et al.; *'The endpoint of the rp-process on accreting neutron stars'*; **Nucl. Phys. A 688, 150c-153c**; [2001]

[Sch04] Schatz; *'Running an X-ray burst network calculation'*; **private communications**; [2004]

[Sch05] Schatz et al.; *'New* $^{32}Cl(p,\gamma)^{33}Ar$ *reaction rate for astrophysical rp-process calculations'*; **arXiv:nucl-ex/0511040 v1**; [2005]

[Sch06a] Schatz et al.; *'The importance of nuclear masses in the astrophysical rp-process'*; **Int. J. Mass. Spec. 251 (2-3) 293**; [2006]

[Sch06b] Schatz et al.; *'X-ray binaries'*; **arXiv:astro-ph/0607624 v2**; [2006]

[Sch06c] Schatz et al.; *'Quests in nuclear astrophysics'*; **priv.comm.**; [2006]

[Sch07] Schatz; **Private communications**; [2007]

[Str67] Strutinsky; *'Shell effects in nuclear masses and deformation energies'*; **Nucl. Phys. A95, 420**; [1967]

[Tri07] ; $http://www.titan.triumf.ca/equipment/penning_trap/index.shtml$;[2007]

[Van85] van der Meer et al.; *"*; **Rev. Mod. Phys. 57, 689 - 697**; [1985]

[Vor06] Vorobjev et al.; *'Mass measurements of radionuclides in the endpoint of the rp-process at SHIPTRAP'*; **Hyperfine Interactions 173, 133**; [2006]

[Wal81] Wallace et al.; *'Explosive Hydrogen Burning'*; **Astro. J. Supp 45,389**; [1981]

[Wan06] Wanajo et al.; *'The rp-Process in Neutrino-driven Winds'*; **Astro. J. 647 (2) 1323**; [2006]

[Wap58] Wapstra et al.; *'Atomic Masses of Nuclides'*; **Springer**; [1958]

[Wei38] von Weizscker, C.F.; **Phys. Z. 39, 633**; [1938]

[Wind] Illustration is calculated with 'νp-process in early protonrich ejecta'- network code provided by Martinez-Pinedo et al.. Settings and temperature evolution are provided by supernova simulation by Janka et al.

[Wol87] Wollnik et al.; **approved experiment proposal at FRS-ESR**; [1987]

[Wol03] Wollnik et al.; *'An energy-isochronous multi-pass time-of-flight mass spectrometer consisting of two coaxial electrostatical mirrors'***Int.J.Mass Spectr. 227, 217**; [2003]

[Woo02] Woosley et al.; *'The evolution and explosion of massive stars'*; **Rev. mod. phys. 74,1015**; [2002]

[Woo04] Woosley et al.; *'Models for type I x-ray bursts with improved nuclear physics'*; **Astro. J. Supp 151 (1) 75**; [2004]

[XRB] Illustration is calculated with the type II x-ray burst network code, provided by Schatz et al.. Settings are taken from [Sch98].

Danksagung

Ich möchte allen danken, die zum Gelingen dieser Arbeit beigetragen haben. Im besonderen danke ich Herrn Prof. Dr. Hans Geissel, Dr. Wolfgang Plass und Prof. Dr. Christoph Scheidenberger für die freundliche Aufnahme am II. Physikalischen Institut und für Ihre überaus engagierte, kompetente und unermüdliche Unterstützung.

Herrn Dr. Gabriel Martinez-Pinedo möchte ich für seine hochqualifizierte und freundliche Hilfe bei der Fertigstellung der Arbeit danken, ebenso für das Bereitstellen des Netzwerkcodes.

Mein Dank geht auch an zu Herrn Prof. Dr. Hendrik Schatz und der JINA- Arbeitsgruppe, unter anderen Karl Smith, Lindsay Hebeler, Richard Cyburt und Milan Matos für die Ermöglichung eines interessanten Aufenthalts in der Michigan State Universtiy und wertvollen Ratschlägen.

Bedanken möchte ich mich auch bei meinen geschätzten Arbeitskollegen der IONAS- Gruppe der Universität Giessen, im besonderen Emma Haettner, Natalia Kuzminchuk, Christa Momberger, Katrin Reinheimer, Lixin Chen, Timo Dickel, Benjamin Fabian, Christian Jesch, Martin Petrick und Björn Riese für inspirierende und motivierende Gespräche und Arbeitspausen zur rechten Zeit.

Für die technische Unterstützung danke ich herzlich der IT-Gruppen der GSI und MSU.

Ganz besonders danke ich meiner Freundin Daniela Burggraf und meiner Familie.

Versicherung

Ich versichere, die vorliegende Arbeit selbständig erstellt und nur die aufgeführten Hilfsmittel benutzt zu haben.

Giessen, 2007

Timo Fleckenstein

Appendix A

Tables

A.1 Extrapolated mass excess values

A	Z	N	Mass excess AME 2003	δM	Mass excess This work	δM	Diff
82	40	42	-64192	225	-63788.37	141.53	403.63
82	41	41	-52974	298	-52520.57	247.33	453.43
84	41	43	-61879	298	-61103.62	317.33	775.38
83	42	41	-47748	503	-47369.87	364.19	378.13
84	42	42	-55806	401	-54953.91	238.68	852.09
85	42	43	-59103	280	-57570.61	408.38	1532.39
85	43	42	-47665	401	-46344.35	428.46	1320.65
86	43	43	-53207	298	-52160.59	501.62	1046.41
87	43	44	-59122	298	-57742.5	107.91	1379.5
88	43	45	-62710	201	-61561.07	233.12	1148.93
87	44	43	-47339	596	-46292.59	261.62	1046.41
88	44	44	-55647	401	-54551.55	453.6	1095.45
89	44	45	-59513	503	-58808.62	345.99	704.38
89	45	44	-47658	448	-46562.55	169.13	1095.45
90	45	45	-53216	503	-52505.3	314.15	710.7
91	45	46	-59103	401	-58097.4	205.3	1005.6
91	46	45	-47403	566	-46692.3	286.68	710.7
92	46	46	-55498	503	-54238.56	225.92	1259.44
93	46	47	-59699	401	-58886.52	128.61	812.48
94	46	48	-66350	401	-66022.32	152.75	327.68
95	46	49	-70151	401	-70206.04	260.96	-55.04
93	47	46	-46780	596	-45958.63	230.63	821.37
94	47	47	-53300	503	-52360.31	286.51	939.69
95	47	48	-60100	401	-59513.6	193.86	586.4
96	47	49	-64571	401	-64839.92	554.42	-268.92
95	48	47	-46696	596	-46144.99	181.38	551.01
96	48	48	-56104	503	-55651.09	235.87	452.91
97	48	49	-60603	401	-60960.79	396.87	-357.79
99	48	51	-69853	205	-69957.64	119.99	-104.64
97	49	48	-47003	596	-46550.09	290.71	452.91
98	49	49	-53896	196	-54295.66	466.19	-399.66
99	49	50	-61274	401	-60912.17	401.53	361.83
101	49	52	-68614	298	-68438.57	148.63	175.43

A	Z	N	Mass excess AME 2003	δM	Mass excess This work	δM	Diff
99	50	49	-47199	596	-47598.66	205.12	-399.66
101	50	51	-59560	298	-59851.5	165.38	-291.5
103	50	53	-66974	298	-67049.19	126.97	-75.19
103	51	52	-56178	298	-56444.19	522.21	-266.19
104	51	53	-59176	362	-59322.35	430.75	-146.35
105	52	53	-52499	503	-52870.3	192.58	-371.3
107	52	55	-60541	298	-60843.6	192.8	-302.6
108	53	55	-52652	359	-52732.52	154.08	-80.52
110	53	57	-60321	309	-60304.35	116.16	16.65
114	53	61	-72796	298	-72663.35	67.34	132.65
111	54	57	-54397	302	-54694.68	73.73	-297.68
112	55	57	-46294	302	-46345.02	210.42	-51.02
114	55	59	-54500	300	-54727.07	212.43	-227.07
115	55	60	-59700	300	-59602.6	210.76	97.4
116	55	61	-62070	100	-62098.12	210.42	-28.12
116	56	60	-54600	400	-54660.85	189.83	-60.85
117	56	61	-57300	300	-57032.34	191.78	267.66
118	56	62	-62370	200	-62222.83	191.85	147.17
121	57	64	-62400	500	-62331.31	132.87	68.69
122	58	64	-57800	400	-58122.56	187.79	-322.56
123	58	65	-60200	300	-60634.01	103.32	-434.01
123	59	64	-50300	600	-50484.31	243.37	-184.31
124	59	65	-53100	600	-53695.11	141.78	-595.11
125	59	66	-57900	400	-58050.12	254.79	-150.12
126	59	67	-60260	200	-60256.88	147.88	3.12
124	60	64	-44500	600	-44913.31	301.94	-413.31
125	60	65	-47600	400	-48096.52	179.24	-496.52
126	60	66	-52900	400	-53569.28	316.49	-669.28
127	60	67	-55400	400	-55625.79	166.15	-225.79
128	60	68	-60180	200	-60401.64	434.93	-221.64
126	61	65	-39600	500	-39991.35	220.23	-391.35
127	61	66	-45100	600	-45405.64	376.14	-305.64
128	61	67	-48000	400	-48134.54	195.33	-134.54
129	61	68	-52900	400	-53046.46	558.66	-146.46
128	62	66	-39000	500	-39416.86	439.02	-416.86
129	62	67	-42300	500	-42213.37	227.64	86.63
130	62	68	-47600	400	-47819.09	682.2	-219.09
130	63	67	-33900	500	-33622.14	460.2	277.86
131	63	68	-39400	400	-39527.93	807.45	-127.93

Table 1: This table shows a comparison between the extrapolated mass excess values of AME 2003 and of this work [keV]. δM gives the error of the mass excess extrapolation in keV. The last column presents the difference of the mass excess values (M(This work) − M(AME 2003)[keV]. This table is illustrated in figure 5.10.)